Nonlinear optical endoscopy with micro-structured photonic crystal fibers

Alberto Lombardini

Aix Marseille Université
Institut Fresnel
École Doctorale 352: Physique et sciences de la matière

Endoscopie optique non-linéaire avec fibres microstructurées à cristaux photoniques

Thèse pour obtenir le grade universitaire de docteur
Discipline : Optique, photonique et traitement d'image
Présentée par:

Alberto LOMBARDINI

Soutenue le 13 Décembre 2016 devant le jury :

Frédéric LOURADOUR	Université de Limoges	Rapporteur
Andreas ZUMBUSCH	Universität Konstanz	Rapporteur
Alexandre KUDLINSKI	Université de Lille	Examinateur
Ingo RIMKE	APE GmbH, Berlin	Examinateur
Hervé RIGNEAULT	Institut Fresnel	Directeur de thèse

Aix Marseille University
Fresnel Institute
Doctoral school 352: Physics and science of matter

Nonlinear optical endoscopy with micro-structured photonic crystal fibers

A thesis submitted for the degree of Doctor of Philosophy
Specialty: Optics, photonics and image processing
Defended on the 13th of December 2016 by:

Alberto LOMBARDINI

Defense commitee:

Frédéric LOURADOUR	Université de Limoges	Reviewer
Andreas ZUMBUSCH	Universität Konstanz	Reviewer
Alexandre KUDLINSKI	Université de Lille	Examiner
Ingo RIMKE	APE GmbH, Berlin	Examiner
Hervé RIGNEAULT	Institut Fresnel	Supervisor

This work was supported by the European Commission, Research Executive Agency Marie Curie Actions 607842 FINON ITN-2013.

Contents

Introduction

Nonlinear optical microscopy (NLOM) represents today a very powerful tool for the study of biological tissues. NLOM became a truly active field by the 1990s, when the availability of stable laser sources, delivering ultra-short pulses (on the order of $10^{-12} - 10^{-13}$ s duration), allowed the application in microscopy of different nonlinear contrast mechanisms. In fact, the use of pulsed lasers is necessary, in order to reach high field intensities with relatively low average powers, avoiding photo-damage of biological tissues.

Today, nonlinear microscopes can incorporate several imaging techniques on the same setup. For instance, two-photon excited fluorescence (TPEF) and second harmonic generation (SHG) can be simultaneously excited with a single-wavelength pulsed laser. Coherent Raman scattering techniques, such as coherent anti-Stokes Raman scattering (CARS) and stimulated Raman scattering (SRS), employ two synchronized laser pulse trains at different wavelengths, in order to stimulate the transitions between different vibrational levels of a molecule. These techniques are said to be chemically specific, because they can probe the molecular content of a sample, by driving chemical bonds into coherent oscillations.

The success of NLOM is also due to its intrinsic optical sectioning capability, which has pushed the penetration depth inside biological tissues, reaching locations previously inaccessible to linear microscopy. Moreover, in live tissues many cellular and extracellular components are intrinsic nonlinear markers. Collagen type I, the most abundant component of the connective tissue, is a strong emitter of SHG radiation. Different molecules, such as the NAD(H) and flavine proteins, can be imaged by TPEF. CARS and SRS have been widely used to visualize lipid droplets and cells, thanks to the strong Raman response of the CH_2 antisymmetric stretch vibration. Recently, different Raman lines have been recently used to differentiate DNA from cellular proteins and lipids in SRS images of live cells.

This is very promising, in sight of the application of NLOM as a label-free histology method for tissue inspection and diagnosis. In fact, the proliferation of cells, characterized by a very high density of nuclei, is one of the criteria employed by histopathologists to differentiate a malignant tissue from a normal one. Collagen degradation and disordering is also linked to many pathologies, and comparisons of NLOM images with conventionally stained histology slides have shown a very high degree of correlation between the two techniques. Many research groups are

currently working on the combination of nonlinear imaging techniques for fast and label-free inspection of tissues. The capability of performing in-vivo, label-free optical biopsy could have a large impact in many clinical situations, especially during surgeries, where tumor margins are not always identifiable by white light imaging, and their fast and precise identification is necessary.

The development of portable, miniature endoscope probes, capable of performing in-vivo nonlinear imaging of biological tissues, is a necessary condition for the translation of NLOM into clinical routine. One of the main challenges is related to the transmission of the ultra-short pulses with optical fibers. In classical single mode fibers, the pulses are affected by dispersive and nonlinear effects, which are difficult to control and alter the temporal profile of the pulses, generally reducing the efficiency in nonlinear signal excitation. Pre-compensation of these effects is possible, but it is generally effective in a narrow wavelength range, limiting the spectral tunability of the probes. Moreover, a very strong four wave mixing (FWM) background is generated in silica fibers. This has been so far the main obstacle to the development of CARS miniature and portable probes. Hence, the incorporation of multiple modalities in the same probe, which is very important for nonlinear imaging, is not a trivial step.

The invention of photonic crystal fibers (PCFs) has brought to a revolution in the field of ultra-short pulse transmission. These fibers are made of a micro-structured air-silica clad, surrounding either a solid core or a hollow core (HC). The delivery of ultra-short pulses through a HC reduces, by three orders of magnitude, the nonlinear effects experienced by the pulses, which makes them very promising for nonlinear endoscopy. New HC fiber designs, such as the Kagomé fiber, have greatly enhanced the width of the fiber transmission window. Moreover, the temporal broadening of the pulses is negligible in Kagomé fibers, thanks to the low, negative values of the group velocity dispersion. The pulses are delivered with no distortions and a negligible CARS signal is generated in such a fiber.

In this thesis, we used a Kagomé fiber designed for nonlinear endoscopy, for the development of a miniature (4 mm diameter, 72 mm rigid length) and portable probe. The system is based on a piezo-electric tube scanner and an achromatic miniature lens assembly, to perform imaging at the distal end of the Kagomé fiber. This has allowed us, for the first time to our best knowledge, to combine femtosecond TPEF, SHG and CARS imaging in such a compact endoscopic system.

This manuscript is organized as follows:

- **Chapter 1**: In this chapter we introduce NLOM and review the state-of-art in nonlinear endoscopy. We present different nonlinear contrast mechanisms and compare the optical properties of linear microscopy with those of NLOM. Then we discuss the practical aspects for the implementation of a NLOM setup. We review some of the applications of NLOM to bio-imaging, with a focus on multiphoton histopathology. The last part is a review of the recent literature concerning the development of nonlinear miniature probes, with a separate focus on TPEF/SHG and CARS endoscopes.

- **Chapter 2**: We present here the theory of pulse propagation in optical fibers. We discuss the effects of group velocity dispersion (GVD), self-phase modulation (SPM) and cross-phase modulation (XPM) on short pulses. We introduce the Nonlinear Schrödinger Equation (NLSE), which defines the evolution of the electric field in optical fibers, and the split-step Fourier method, which is used to obtain numerical solutions of the NLSE.

- **Chapter 3**: We first review the different optical fibers existing today, and their application to short pulse delivery in nonlinear endoscopy. We highlight the problems related to the temporal and spectral broadening, and the FWM background generated in silica fibers. The chapter is then dedicated to the characterization of a Kagomé fiber for short pulse delivery. We show that spectral and temporal effects, after propagation in 1 m of Kagomé fiber, are negligible even for pulses of 100 fs duration. This largely simplifies the implementation of multimodal nonlinear endoscopes.

- **Chapter 4**: We discuss here the different components of the fiber-scan device developed for nonlinear imaging. We study the mechanical aspects related to the resonant scan of the optical fiber. We present the algorithm developed to control the scan, acquire the signal and reconstruct the images. Then we introduce the Kagomé double clad (DC) fiber, specifically designed for nonlinear endoscopy. Finally we introduce the custom designed miniature lens system, based on four achromatic doublets, for efficient beam focusing on the sample.

- **Chapter 5**: We show here the imaging results obtained with the Kagomé DC scanner, whose development was described in Ch. 4. We characterize the system in terms of field-of-view (FOV) and point spread function (PSF). We perform nonlinear imaging, activating TPEF, SHG and CARS contrasts, both on test samples and unlabeled biological tissues ex-vivo.

- **Chapter 6**: We report here the integration of the miniature imaging system in a portable probe. We describe the procedure followed to seal the bead on the fiber core and present the mechanical aspects of the integration. Then we characterize the probe imaging performances and finally discuss the perspectives for future improvements in the probe.

- **Chapter 7**: In perspective of the implementation of SRS imaging in the endoscope probe, we study here the effects related to the delivery of picosecond pulses through a Kagomé fiber. We show that a wavelength dependent background is generated in the fiber, because of a coupling between nonlinear effects and fiber losses. We carry out numerical simulations to estimate the order of magnitudes of such a background. We then perform experiments to measure the effective background generated in the Kagomé fiber.

Chapter 1

Nonlinear imaging: from microscopy to endoscopy

This chapter is an introduction to nonlinear optical microscopy (NLOM) and endoscopy techniques. We first introduce the different contrast mechanisms and discuss the benefits of NLOM over linear microscopy. Then, we review the key technical aspects of nonlinear microscopes and the applications of NLOM to biological tissue imaging. In the second part of the chapter we present the current state of the art in the development of miniature probes for nonlinear endoscopic imaging.

1.1 Nonlinear microscopy

Optical imaging techniques are based on the interaction between a light source and the sample. While linear microscopy is based on phenomena such as linear absorption, scattering or index-dependent phase differences, NLOM measures the nonlinear response of a sample to an intense optical field $\vec{E}$. A general description of nonlinear optical interactions can be done in terms of the nonlinear polarization (dipole moment per unit volume), which is related to the nonlinear susceptibility of the material. The material polarization $\tilde{P}(t)$ can be expanded as a Taylor series of the electric field $\tilde{E}(t)$ [95]:

$$\tilde{P}(t) = \epsilon_0 \left[\chi^{(1)} \tilde{E}(t) + \chi^{(2)} \tilde{E}^2(t) + \chi^{(3)} \tilde{E}^3(t) + \cdots \right] \equiv \tilde{P}^{(1)}(t) + \tilde{P}^{(2)}(t) + \tilde{P}^{(3)}(t) + \cdots \quad (1.1)$$

Where $\chi^{(1)}$ is the linear susceptibility, $\chi^{(2)}$ is the second-order susceptibility and so on; $P^{(1)}$ the linear polarization, $P^{(2)}$ the second-order polarization and so on. For the sake of simplicity, $\tilde{E}$ and $\tilde{P}$ are taken as scalar quantities, but a vectorial description is possible for a deeper analysis [11]. Nonlinear optical interactions all occur because of the nonlinear polarization terms, as we will see in the next sections.

The first observation of nonlinear optical phenomena was done in the decade when the laser was invented. In just a few years, experimental evidence of two-photon excited fluorescence (TPEF [68]), second harmonic generation (SHG [42]), stimulated Raman scattering (SRS [34]), coherent anti-stokes Raman scattering (CARS [94]) was reported. However, the birth of modern NLOM[1] came with the combination of two-photon absorption and beam scanning techniques in 1990 [27]. That was the moment when advances in laser technology had made femtosecond lasers commercially available on a large scale, prompting the diffusion of NLO microscopes. We will now describe different nonlinear optical processes and their application in microscopy.

1.1.1 TPEF and SHG

TPE and SHG are both due to the simultaneous[2] interaction of two photons with a molecule, and can be both excited with a single laser source. However the nature of the processes is very different: SHG is a parametric[3], instantaneous process mediated by virtual states only; its radiation is highly directional and coherent. In TPEF a part of the photon energy is lost to the sample (through vibrational relaxations) and the molecule is excited to an energy eigenstate, which leads to the emission lifetimes on the order of nanoseconds (10^{-9} s). The emitted fluorescence light is incoherent, since it holds no phase relation with the exciting field. Moreover, while SHG radiation is highly directional, fluorescence emitted from a homogeneous solution is isotropic.

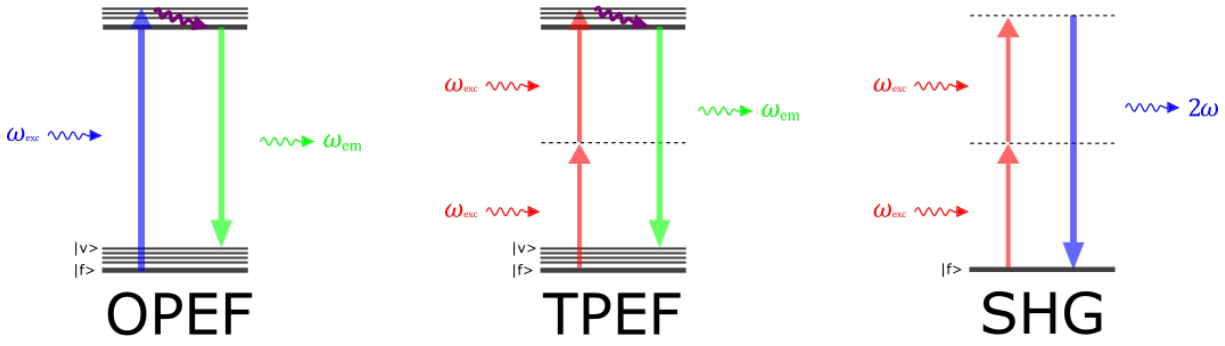

Figure 1.1: Molecular energy diagrams for the processes of one and two-photon excited fluorescence and second harmonic generation.

[1] A CARS microscope was developed in 1982 by Duncan et al. [33], in a non-collinear geometry to achieve phase matching. However this system lacked optical sectioning, a very important feature for NLOM.

[2] In the quantum world this means fractions of a femtosecond ($< 10^{-15}$ s), because of Heisenberg uncertainty relation between time and energy, that allows molecules to be in a *virtual state* (not an eigenstate of the molecule) for such a time window.

[3] It means that the initial and final quantum states are the same: this imposes photon energy and momentum conservation on the process, meaning that no energy is transferred to the material.

Two-photon excitation Two-photon absorption (TPA) occurs when an atom or a molecule is excited by the *simultaneous* absorption of two photons, whose combined energy matches the energy gap between the ground state and the excited electronic state (Fig. 1.1). In the classical description, TPEF is related to the imaginary part of the third-order susceptibility $Im\left\{\chi^{(3)}\right\}$. The theoretical description of TPE from a quantum point of view was first done by Maria Goeppert-Mayer, in her PhD thesis dissertation (1931) [54].

A molecule's *jump* to an excited electronic state is mediated by a virtual state, where the molecule stays for about 10^{-16} s. After excitation, the molecule relaxes to the vibrational ground state (after approximately 10^{-12} s) and subsequently decay to the electronic ground state with emission of a photon (10^{-9} s after excitation) [95]. The probability for a molecule to follow this pathway after absorption is defined as the *quantum yield*.

The condition on the photon wavelengths for TPEF can be expressed as:

$$\lambda_{\mathrm{OPE}} \approx \left(\frac{1}{\lambda_{\mathrm{A}}} + \frac{1}{\lambda_{\mathrm{B}}}\right)^{-1} \tag{1.2}$$

Where λ_{OPE} is the peak in the one-photon excitation (OPE) spectrum, λ_{A} and λ_{B} the excitation photons wavelengths. When TPEF is performed with a single wavelength, this condition becomes:

$$\lambda_{\mathrm{A}} = \lambda_{\mathrm{B}} \approx 2\lambda_{\mathrm{OPE}} \tag{1.3}$$

This provides a useful rule of thumb for two-photon excitation: a molecule with an OPE peak at wavelength $\tilde{\lambda}$ will be efficiently excited by photons having wavelength $2\tilde{\lambda}$. In OPE fluorescence, the emitted photon has a lower energy than the incident photon ($\lambda_{\mathrm{em}} > \lambda_{\mathrm{exc}}$), because some of the energy is dissipated through vibrational relaxations (fig. 1.1).
It can be shown that the excitation probability, and therefore the TPEF intensity is proportional to the square of the excitation light intensity I_{exc}:

$$I_{\mathrm{TPEF}} \propto {I_{\mathrm{exc}}}^2 \tag{1.4}$$

which has fundamental implications for the optical properties TPEF microscopy (discussed in section 1.1.3).

The transition probability for two-photon excitation is very low at ambient light conditions. Hence, a very high photon flux is required for efficient excitation, which can be reached with pulsed femtosecond lasers that are tightly focused using high NA objectives. A pulsed laser enhances the TPE process by a factor $1/(\tau f_{\mathrm{R}})$ as compared to a CW laser with the same average power. For a pulse duration $\tau = 100$ fs and a repetition rate $f_{\mathrm{R}} = 100$ MHz, the TPEF efficiency is increased by a factor 10^5 [58].

TPEF microscopy has become very popular since its first demonstration [27], thanks to its optical properties (see Sec. 1.1.3) and the widespread diffusion of Ti:Sa lasers. Moreover, one

big advantage of TPEF relies in the possibility to exploit the same fluorophores used in confocal fluorescence microscopy. A wide variety of exogenous probes exist today: organic probes, genetically expressed probes, quantum dots. Moreover, there exist many endogenous fluorophores for TPEF (elastin, keratine, flavoproteines, NADH and NAD(P)H, neurotransmitters...), that are naturally present in cells and tissues. Thanks to these molecules, it is possible to image live cells without labeling them with exogenous probe that perturb the cell's physiology.

Second harmonic generation The generation of a new field, at twice the frequency of the incident field, is due to the nonlinear polarization term originating from the second order nonlinear susceptibility $\chi^{(2)}$ [11]. Let us consider an electric field oscillating at frequency ω, that can be written as:

$$\tilde{E}(t) = E \cdot e^{-i\omega t} + c.c. \tag{1.5}$$

When the field is incident on a material with $\chi^{(2)} \neq 0$, a second order nonlinear polarization term (Eq. (1.1)) is generated:

$$\tilde{P}^{(2)}(t) = 2\epsilon_0 \chi^{(2)} E E^* + \left(\epsilon_0 \chi^{(2)} E^2 e^{-i2\omega t} + c.c.\right) \tag{1.6}$$

The first term is stationary and is responsible for optical rectification (a constant field is created in the material). The second term contains an oscillation at frequency 2ω and is responsible for SHG.

In the quantum picture, SHG happens when two photons of the same energy ω are annihilated to generate a photon with energy 2ω, as illustrated in Fig. 1.1. The process is mediated by a virtual state and must not violate energy and momentum conservation, which imposes two conditions on the characteristics of the generated photon. Energy conservation implies that $\omega_{\mathrm{s}} = 2\omega_{\mathrm{i}}$, while from momentum conservation comes the *phase matching* condition:

$$\vec{k}_{\mathrm{s}} = 2\vec{k}_{\mathrm{i}} \tag{1.7}$$

Here ω_{i} and ω_{s} are the frequencies of the incident and scattered photons, respectively, while $\vec{k}_{\mathrm{i}}$ and $\vec{k}_{\mathrm{s}}$ are their wavevectors. In SHG microscopy this condition is usually relaxed, because tight focusing of the excitation beam generates a wide distribution of $\vec{k}$ vectors in the field.
From Eq. (1.6) it appears that the SHG signal is proportional to the square of the excitation power:

$$I_{SHG} \propto \left|\tilde{P}^{(2)}(2\omega)\right|^2 \propto I_{exc}^2 \tag{1.8}$$

For symmetry reasons $\chi^{(2)}$ can be nonzero only in media that do not possess inversion symmetry [11]. For instance, no SHG radiation is generated in isotropic media, because of their centrosymmetric molecular structure. In random media, such as liquid solvents or amorphous solids, there is no SHG radiation because the net contribution from the molecules is averaged to

zero [95].

SHG microscopy is particularly interesting for live cells and tissues imaging [153]. Certain biological structures are strong SHG scatterers, such as type I collagen, which is an essential component of the connective tissue [152]. SHG has been also used to image myosin heads in muscle [113] and microtubules [30]. The reader can find a review of the application of SHG to tissue imaging and disease diagnosis in [15].

1.1.2 Vibrational Imaging

The recent development of Coherent Raman imaging techniques has enabled video-rate in-vivo vibrational imaging of tissues. We speak of molecular vibrations when the atoms, held together by molecular bonds, oscillate in a synchronized and periodic fashion. A vibrational mode can be described as a simple one-dimensional harmonic oscillator, after an appropriate coordinate transformation. Each chemical bond has characteristic resonant frequencies, that depend on which atoms participate in the bond and on the environmental conditions. This provides a distinctive signature for molecular bonds, that can be used to investigate the chemical content of a sample. The vibrational spectrum of a sample can be probed by IR absorption or Raman scattering.

Spontaneous Raman and IR absorption spectroscopy

IR absorption spectroscopy is based on the direct absorption of infrared light (in the wavelength range 3-30 $\mu\mathrm{m}$) that excite molecular vibrations. Fourier transform IR microscopy has been used for chemical imaging of histological slices (see [37]). However this technique holds two major drawbacks: low spatial resolution, due to the long excitation wavelength, and strong absorption of light by water, that limits live-cell imaging and penetration in tissues.

Raman spectroscopy typically uses shorter-wavelength visible light for excitation, which is beneficial for cells and tissue analysis (as reviewed in [102]). Spontaneous Raman scattering is a form of inelastic light scattering, that involves an energy exchange between a photon and a molecule, mediated by a molecular vibrational states. If we consider a molecular vibration, whose resonant frequency is Ω_{R}, and an incident photon of frequency ω, a Raman scattered photon can have a frequency $\omega - \Omega_{\mathrm{R}}$ (Stokes photon) or $\omega + \Omega_{\mathrm{R}}$ (anti-Stokes photon). The situation is described in Fig. 1.2. The anti-Stokes radiation is typically much smaller than the Stokes one, since at room temperature most of the molecules are in the vibrational ground state. In fact, both the Stokes and anti-Stokes radiations are very small, with only one out of 10^5 photons being Raman scattered.

While Raman microscopes exist since the 1970s, their speed is limited to few milliseconds per pixel because of the extremely small Raman cross sections (10^{-14} smaller than fluorescence cross sections). The frame rate of such microscope is on the order of tens of minutes per image

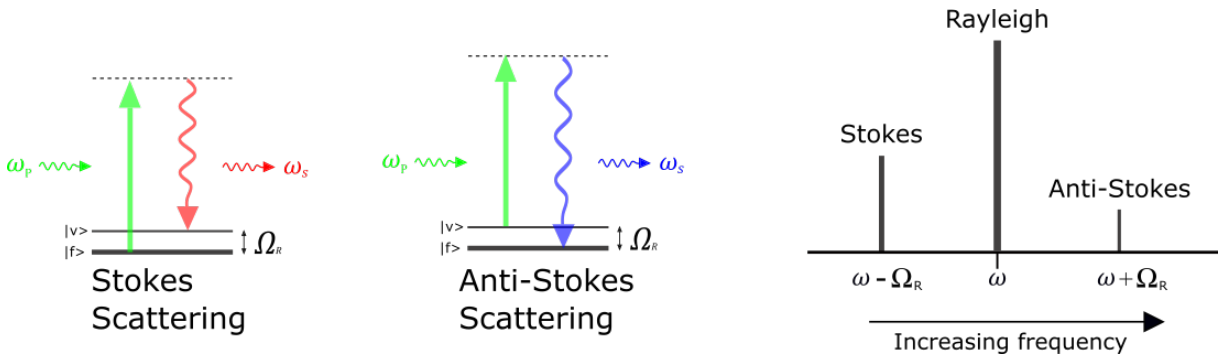

Figure 1.2: Energy diagrams describing spontaneous Raman scattering processes and comparison between the energy of Raman and Rayleigh scattered photons.

[108], which makes them too slow for live cell dynamics or surgery guidance applications.

Coherent Raman scattering (CRS) methods, such as CARS and SRS, overcome the frame rate limitations of spontaneous Raman scattering by boosting the weak Raman signal.

Coherent Raman Scattering

The first implementation of modern CARS microscopy dates back to the end of the 1990s, when Zumbusch et al. performed fs-CARS imaging in a collinear geometry using a high NA objective to focus on the sample [154], which relaxed the phase matching condition and significantly improved the axial resolution (as compared to existing CARS microscopes).

In CARS and SRS microscopy two excitation fields are typically used to generate a coherent Raman signal. A laser beam, called pump (ω_P), is synchronized and overlapped with a lower-frequency beam, called Stokes (ω_S). When the frequency difference between pump and Stokes matches the energy of a vibrational mode Ω_R, four major CRS processes take place, generating fields at frequencies:

$$\omega_\mathrm{P} + \Omega_\mathrm{R} = 2\omega_\mathrm{P} - \omega_\mathrm{S} = \omega_\mathrm{AS} \qquad \text{(CARS)} \tag{1.9}$$

$$\omega_\mathrm{P} - \Omega_\mathrm{R} = \omega_\mathrm{S} \qquad \text{(Stimulated Raman Loss, SRL)} \tag{1.10}$$

$$\omega_\mathrm{S} + \Omega_\mathrm{R} = \omega_\mathrm{P} \qquad \text{(Stimulated Raman Gain, SRG)} \tag{1.11}$$

$$\omega_\mathrm{S} - \Omega_\mathrm{R} = 2\omega_\mathrm{S} - \omega_\mathrm{P} = \omega_\mathrm{CS} \qquad \text{(Coherent Stokes Raman Scattering, CSRS)} \tag{1.12}$$

The origin of these new fields lies in the nonlinear polarization induced by interaction of the pump and Stokes field with the material's nonlinear susceptibility $\chi^{(3)}$ [20]. The first and the last one are parametric processes (the energy of the molecule does not change after interaction), that generate new frequency components. SRG and SRL belong to the process of SRS, where the newly generated fields interfere with the incident fields, leading to a depletion in the pump beam (SRL) and a gain in the Stokes beam (SRG) [20].

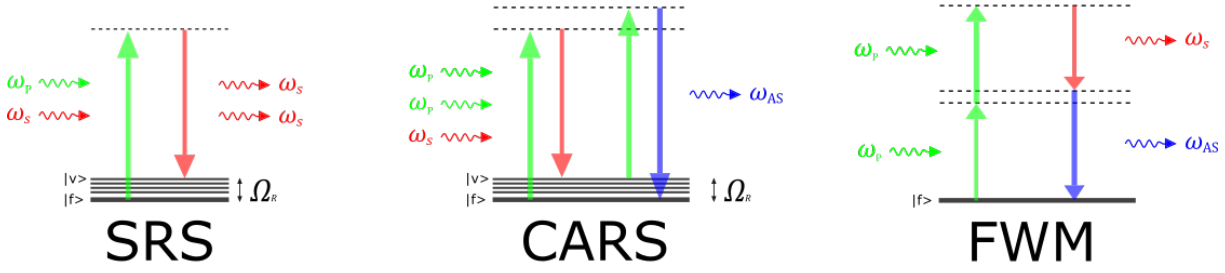

Figure 1.3: Energy diagrams describing Stimulated Raman Scattering, Coherent anti-Stokes Raman Scattering and Four Wave Mixing.

CRS imaging is generally done with femtosecond or picosecond pulses, that ensure high peak powers for efficient activation of the processes. However, while fs-CARS gives higher signal levels, the spectral resolution is limited by the broad spectrum of the pulses. The use of pulses with a duration of few picoseconds only can ensure a vibrational resolution better than 10 cm^{-1}. A strategy to gain spectral resolution with broadband fs pulses is the so-called spectral focusing [57].

CARS microscopy CARS microscopy exploits the radiation due to the nonlinear polarization term at the anti-Stokes frequency $\omega_{\mathrm{AS}} = 2\omega_{\mathrm{P}} - \omega_{\mathrm{S}}$ [9]:

$$\tilde{P}^{(3)}_{\mathrm{AS}}(\omega_{\mathrm{AS}}) = 3\epsilon_0 \chi^{(3)}_{\mathrm{AS}}(\omega_{\mathrm{AS}}) {E_{\mathrm{P}}}^2 {E_{\mathrm{S}}}^* e^{-ik_{\mathrm{AS}}z} \tag{1.13}$$

where E_{P} and E_{S} are the pump and Stokes fields amplitudes, and k_{AS} is the anti-Stokes field wavevector. The intensity of the anti-Stokes field, after a propagation distance L, is [9]:

$$I_{\mathrm{AS}}(L) \propto \left|\chi^{(3)}(\omega_{\mathrm{AS}})\right|^2 {I_{\mathrm{P}}}^2 I_{\mathrm{S}} sinc^2\left(\frac{\delta k L}{2}\right) \tag{1.14}$$

where $\delta\vec{k} = 2\vec{k_{\mathrm{P}}} - \vec{k_{\mathrm{S}}} - \vec{k_{\mathrm{AS}}}$. The CARS signal scales linearly with the Stokes beam power and quadratically with the pump beam power, and is maximum for $\delta\vec{k} = \vec{0}$, which is the phase matching condition. Like in SHG microscopy, this condition is relaxed by using high NA objectives [154]. The $\chi^{(3)}$ tensor in Eq. (1.14) consists of two parts, a resonant and a non-resonant one:

$$\chi^{(3)} = \chi^{(3)}_{\mathrm{R}} + \chi^{(3)}_{\mathrm{NR}} \tag{1.15}$$

Where the non-resonant term $\chi^{(3)}_{\mathrm{NR}}$ can be taken as a real and constant quantity [90, 88]. If we introduce $\chi^{(3)}$ into Eq. (1.14), we obtain:

$$I_{\mathrm{AS}} \propto |\chi^{(3)}_{\mathrm{R}} + \chi^{(3)}_{\mathrm{NR}}|^2 \tag{1.16}$$

$$\propto |\chi^{(3)}_{\mathrm{R}}|^2 + |\chi^{(3)}_{\mathrm{NR}}|^2 + 2 \cdot Re\left\{\chi^{(3)}_{\mathrm{R}} {\chi^{(3)}_{\mathrm{NR}}}^* \cdot\right\} \tag{1.17}$$

$$\propto |\chi^{(3)}_{\mathrm{R}}|^2 + |\chi^{(3)}_{\mathrm{NR}}|^2 + 2\chi^{(3)}_{\mathrm{NR}} \cdot Re\left\{\chi^{(3)}_{\mathrm{R}}\right\} \tag{1.18}$$

This means that the CARS signal comes from the sum of three different contributions of the nonlinear susceptibility:

- The resonant term, containing the spectral information on the vibrational mode of interest. It can be associated to the spontaneous Raman spectrum.
- The non-resonant term, which is frequency independent.
- The crossed term, proportional to the real part of $\chi^{(3)}_{\mathrm{R}}$.

The non-resonant term is at the origin of a spectrally flat Four Wave Mixing (FWM, Fig. 1.3) background, that limits the contrast in vibrational imaging. The last term is responsible for distortions of CARS spectra with respect to the spontaneous Raman ones, because of a spectral interference between the resonant and the cross-term. As a result the CARS peak is blue-shifted as compared to the spontaneous Raman one. Quantitative analysis of CARS images is also made more difficult by the quadratic dependence on the molecular concentration [20].

Different techniques for FWM background suppression have been demonstrated, based on polarization control [19], time-resolved CARS [138], heterodyne detection [114], frequency modulation [48]. SRS microscopy has emerged as a coherent Raman imaging technique free of the nonresonant background that affects CARS microscopy.

SRS microscopy SRS microscopy is based on the detection of the intensity change in the pump beam (SRL) or in the Stokes beam (SRG) after interaction with a sample. This energy change is due to the interference between the newly generated nonlinear fields, at frequencies ω_{P} and ω_{S}, and the exciting fields. The nonlinear polarization of the medium at ω_{P} and ω_{S} is [9]:

$$P(\omega_{\mathrm{P}}) = 6\epsilon_0 \chi^{(3)}_{\mathrm{R}}(\omega_{\mathrm{P}}) \left|E_{\mathrm{S}}\right|^2 E_{\mathrm{P}} e^{i(k_{\mathrm{P}} z)} \tag{1.19}$$

$$P(\omega_{\mathrm{S}}) = 6\epsilon_0 \chi^{(3)}_{\mathrm{R}}(\omega_{\mathrm{S}}) \left|E_{\mathrm{P}}\right|^2 E_{\mathrm{S}} e^{i(k_{\mathrm{S}} z)} \tag{1.20}$$

with $\chi^{(3)}_{\mathrm{R}}(\omega_{\mathrm{P}}) = \chi^{(3)}_{\mathrm{R}}(\omega_{\mathrm{S}})^*$. From these equations one can calculate the fields $\tilde{E}^{(3)}_{\mathrm{P}}$ and $\tilde{E}^{(3)}_{\mathrm{S}}$ that are generated and interfere with the exciting fields. The intensities at the frequencies of interest are then:

$$I_{\mathrm{P}} \propto |E_{\mathrm{P}}|^2 - 2\left|E_{\mathrm{P}} {E_{\mathrm{P}}}^{(3)}\right| \tag{1.21}$$

$$I_{\mathrm{S}} \propto |E_{\mathrm{S}}|^2 + 2\left|E_{\mathrm{S}} {E_{\mathrm{S}}}^{(3)}\right| \tag{1.22}$$

Where ${E_{\mathrm{P}}}^{(3)}$ and ${E_{\mathrm{S}}}^{(3)}$ are the amplitudes of the fields generated by the third-order polarization terms. From this equations one can see that the pump field experiences a depletion (SRL), while the Stokes field experiences a gain (SRG). It can be shown [11] that this intensity variations follow:

$$I_{\mathrm{SRL}} \propto I_{\mathrm{SRG}} \propto I_{\mathrm{P}} \cdot I_{\mathrm{S}} \tag{1.23}$$

In SRS microscopy, one typically detects intensity variations on the order of $\Delta I/I \approx 10^{-5} - 10^{-6}$. To do so, a high-frequency amplitude modulation scheme, with locked-in detection, has to be used [21].

The SRS signal is proportional to the imaginary part of the nonlinear susceptibility $Im\left\{\chi^{(3)}\right\}$, which implies that SRS is free of the nonresonant background that affects CARS imaging and provides spectral profiles nearly identical to spontaneous Raman spectra [20]. Moreover, the dependence on the molecular concentration is linear, which facilitates quantitative analysis of SRS images [21].

The first demonstration of SRS microscopy was reported by Ploetz et al. in 2007. Polymer beads were imaged with a broadband low repetition rate laser source and μJ pulse energies [112]. One year later, the implementation of an SRS microscope with MHz modulation of a picosecond pulse beam was reported by the Freudiger et al. [43]. Since then, SRS microscopy has been implemented by several groups in combination with other NLOM techniques.

1.1.3 A comparison between linear and nonlinear imaging

The optical properties of nonlinear imaging techniques have important consequences when it comes to biological tissue imaging, which make them preferable over linear techniques. To understand what are the implications of nonlinear excitation, let us consider the case of fluorescence microscopy. In one-photon excitation (OPE) fluorescence, there is a linear dependency between the emission and excitation intensities, whereas in TPEF the dependency is quadratic. This has a fundamental implication from an optical point of view. In fact, for OPE fluorescence, the total emitted intensity is constant on each plane perpendicular to the optical axis (Fig. 1.4). This limits the resolution and the contrast of the images, which lack optical sectioning in z. This is solved in confocal microscopy by means of a pinhole, placed before the detector, that rejects out-of-focus light. In nonlinear microscopy, as a consequence of the nonlinear signal dependence on the excitation power, the emitted intensity decreases as $1/z^2$ (for a ${I_{\mathrm{exc}}}^2$ dependence) as we move away from the focus (Fig. 1.4). Then the fluorescence emission is limited to a small region near the focus (with an extension of few micrometers in the axial direction). This is the reason why TPEF and all the other NLOM techniques are said to be intrinsically confocal.

The implications are quite important for imaging in scattering media. NLOM has allowed

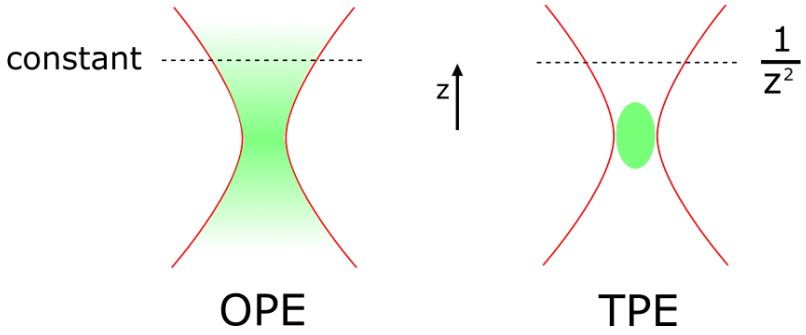

Figure 1.4: The fluorescence emission from an homogenous solution. In the case of one photon excitation, the integrated emission is constant on each plane perpendicular to the optical axis. For two photon excitation the fluorescence emission from out-of-focus planes decreases as $1/z^2$.

to reach penetration depths in biological tissues that were previously inaccessible to optical microscopy (several hundreds of micrometers deep) [58]. Confocal microscopy can overcome some of the effects of scattering, since the detector pinhole rejects fluorescence from off-focus locations. However, this includes the photons that are emitted at the focus, but scattered on their way out of the tissue. Since these photons do not reach the detector, confocal microscopy becomes unacceptably wasteful deep in tissues, which results in very limited penetration depths [28]. Moreover, scanning a single section excites the entire specimen, increasing the risk of photo-damage. The situation changes in TPEF, as illustrated in Fig. 1.5. The NIR excitation light is less sensitive to scattering than the visible light used for one photon fluorescence. When exciting through a scattering medium, the balistic photons that are deviated from their original trajectory do not generate signal, since the intensity is too weak. In the case of emission, scattering causes photons to appear as coming from a wider FOV but, as compared to the non-scattering case, a larger fraction will be in the angular acceptance cone of the objective. The fluorescence light that is generated and back-scattered by the tissue is not filtered by any pinhole and can be detected, provided that it lies in the FOV of the detector and in the angular acceptance cone of the objective. For these reasons, the photon losses are less important in TPEF, allowing deeper imaging in tissues.

Concerning CARS and SRS, we have discussed how they can increase the Raman signal by some orders of magnitude, enabling video-rate vibrational imaging of biological tissues.
A big advantage of nonlinear imaging techniques is that the different NLOM modalities can be implemented on the same microscope set-up, provided that the right laser source is used and a sufficient number of detectors is available. Performing multimodal imaging, with the different contrasts all accessed simultaneously, gives important and complementary informations on the different components of a tissue.

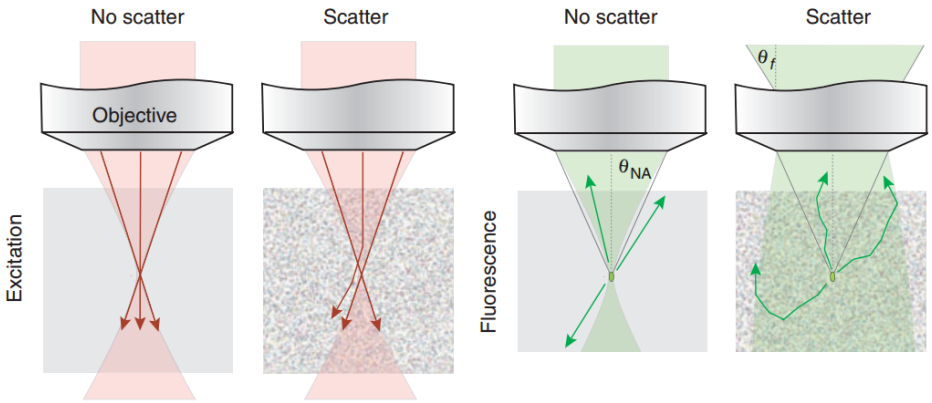

Figure 1.5: Two-photon fluorescence excitation and collection in the case of scattering and non-scattering medium. The NIR excitation light is not intense enough out of the focus to generate signal. The fluorescence light that is generated and back-scattered by the tissue is not filtered by any pinhole and can be detected, provided that it is in the field-of-view (FOV) of the detector and in the angular acceptance cone of the objective. Image taken from [58].

1.1.4 Practical implementation of NLOM

NLOM imaging is usually performed with one or more laser beams that are focused and scanned over the sample. A nonlinear microscope is composed of few fundamental units:

- A **laser source** delivering short pulses for the activation of the nonlinear contrasts.
- A **scanning unit** to move the excitation beams over the sample and perform imaging.
- Microscope objectives to **focus** the beams on the sample and collect the signal.
- Light **detectors** to measure the nonlinear signal generated at each point of the sample during the scan.

A multimodal microscope, incorporating TPEF, SHG, CARS and SRS modalities is shown in Fig. 1.6. One typical laser configuration is the following: a picosecond or femtosecond[4] pulsed laser with high repetition rate (≈ 100 MHz) is frequency doubled and used to pump an Optical Parametric Oscillator (OPO)[5]. The OPO is a tunable laser light source that uses a nonlinear crystal to convert an input photon to two lower-energy photons (called *signal* and *idler*), through the process of Optical Parametric Amplification (OPA). The output wavelength is tuned by acting on the crystal to change the phase matching condition, generally by mechanical or thermal adjustment. The beams generated by the OPO are temporally synchronized with the pump laser. They are then spatially combined using a dichroic mirror, which reflects wavelengths on one side of

[4]For CARS microscopy, ps pulses give better spectral resolution, but the higher peak power of fs pulses is beneficial for efficient signal activation of other nonlinear modalities.

[5]Other configurations exist: the OPO may be pumped by fiber lasers, and all-fiber laser systems have been used as well.

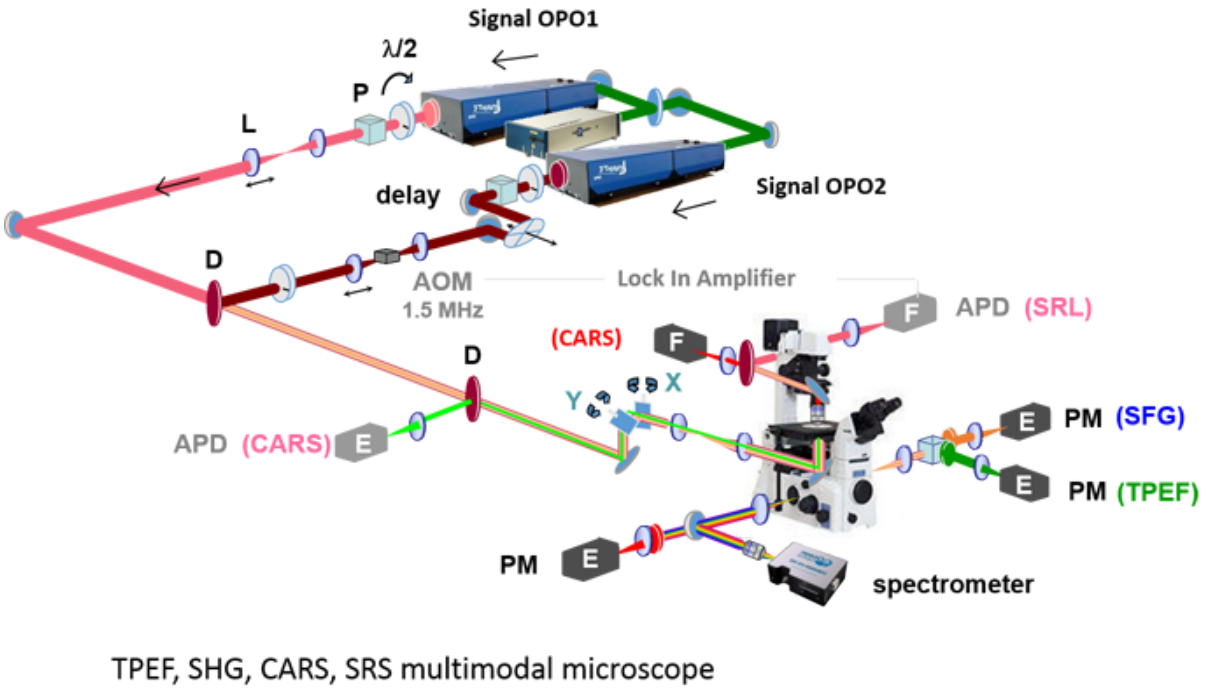

Figure 1.6: A nonlinear microscope, based on two OPOs for excitation. An acoustic-optic modulator (AOM) modulates the amplitude of one beam for SRS imaging. Several detectors are used to measure the different nonlinear interactions.

the cut-off frequency and transmits the other ones. Temporal overlap of the pulses is usually achieved with a mechanical delay line (moveable mirrors). The two beams are then sent to a pair of galvanometric mirrors, which deflects the beams in two lateral directions. The size of the beams is typically enlarged with a beam expander, in order to overfill the objective's back aperture, and exploit the whole NA of the focusing lens. The deflection of the beams from the scanning mirror results in a lateral translation of the focal spot on the sample plane. An image is obtained by measuring the instantaneous response of the sample to the excitation beams, that are focused and moved in a raster pattern. The pixel dwell time is typically on the order of few μs, which results in image acquisition times of tens to hundreds of milliseconds, depending on the image size. The signal generated is either back-collected by the focusing objective (epi-detection, necessary for thick tissues), or collected by another objective lens placed in the forward direction. Dichroic mirrors and optical filters are used to separate the signal of interest from the excitation light. Single point detectors, such as photomultiplier tubes (PMTs) or avalanche photodiodes (APDs), are typically used for photon detection. The signal acquired at each "pixel" is used to reconstruct the image via software.

Today, the majority of CARS microscopes are built in-house in research laboratories and imaging facilities. However some commercial systems for NLOM are now available: the first CARS microscopes were introduced on the market by Olympus (USA) in 2009 and Leica Microsystems (Germany) in 2010. APE GmbH (Berlin, Germany) developed the picoEmerald laser-OPO system for SRS and CARS microscopy, which can be easily integrated in any microscope setup.

1.1.5 Biomedical applications

Multiphoton microscopy is a powerful tool for the inspection of biological tissues, since it allows label-free imaging with sub-cellular resolution and molecular specificity. One promising field of application is that of cancer detection. The current protocol in clinics relies on the extraction of tissues via biopsy and the preparation in thin slices for histological examination. However, biopsies are not free of risk, especially when performed in neurological tissues, where they can cause damage. Moreover, the preparation of histology samples is a time demanding procedure. The conventional procedure, consisting of fixation and staining with hematoxylin & eosin (H&E), requires several hours before the extracted tissue can be examined by the pathologist. During surgery, tumor margins have to be detected as soon as possible, and a faster staining procedure can be followed, which takes approximately 30 minutes. In fact, tumors are not often detectable by white light examination, and failures in complete removal are one of the main causes of disease recurrence in patients.

NLOM techniques could potentially improve the protocol, offering a real-time, label-free diagnostic method. For this reason, several research works are carried out today in the direction of what is often called multiphoton histopathology. The goal is to prove NLOM capable of

retrieving the same degree of information on the morphology and the molecular composition of a tissue, as the one offered by conventional histology methods. In fact, histological diagnosis is generally based on the morphological observation of disease progression in a tissue. The disorganization of the connective tissue, together with an increased nuclear density due to the proliferation of cancer cells, are generally indicators of a diseased tissue. Performing label-free optical histology with NLOM would carry huge benefits, especially in those situations where a fast and precise identification of tumor margins is required. For the very same reason, the development of miniature and portable nonlinear endoscope probes is a crucial step for the future translation of NLOM in clinics. The rest of this section is dedicated to the application of multiphoton microscopy to tissue examination and inspection.

Multiphoton microscopy in tissues TPEF and SHG can rely on different endogenous sources of signal in biological tissues. Different components, both inside cells and in the extracellular matrix, can be imaged because of their nonlinear optical response. Inside cells, the main sources of fluorescence are NAD(P)H, flavins, retinol and tryptophan. In the extracellular matrix, elastin and collagen are responsible for TPEF and SHG emission [152]. Lipid imaging has been a primary focus for CARS and SRS microscopy, because of the strong Raman response given by the abundant $\mathrm{C}-\mathrm{H}$ bonds found in such structures [21]. For instance, lipids play an important role in atherosclerosis the most common cardiovascular disease, where the arterial walls are thickened by the accumulation of fatty deposits [81, 69, 96]. As we will see, recent works have highlighted the possibility to image DNA in live cells using SRS microscopy [91], which adds a very important information for histology. The interested reader can find more about the biological applications of CRS imaging in a recent review [14].

Disease diagnostics Many studies have highlighted the correlation between disease progression and a reduction in SHG signal, due to the lower collagen content and reduced ordering of the collagen structure [152, 49, 149]. Collagen reorganization at the tumor-stromal interface was used to detect cancer in mammary glands, using three-dimensional informations on the organization of the mammary stroma, which were not available in conventional histology [115]. The density reduction and disordering of collagen fibrils in breast, bone and skin cancers was also indicated as a potential diagnostic tool [60].

TPEF and SHG have been applied to the detection of ovarian cancer in fresh, unstained and unfixed human tissues, comparing it with conventional histology imaging. The results showed a high degree of correlation between the two techniques [146]. The spectroscopic analysis of endogeneous fluorescence excitation and emission has given promising results in real-time cancer detection in the gastrointestinal tract [56], in lungs [74] and colon [62].

Coherent Raman imaging has been applied in different studies, in combination with TPEF and SHG, to study the morphological features of diseased tissues. As an example, Freudiger et al.

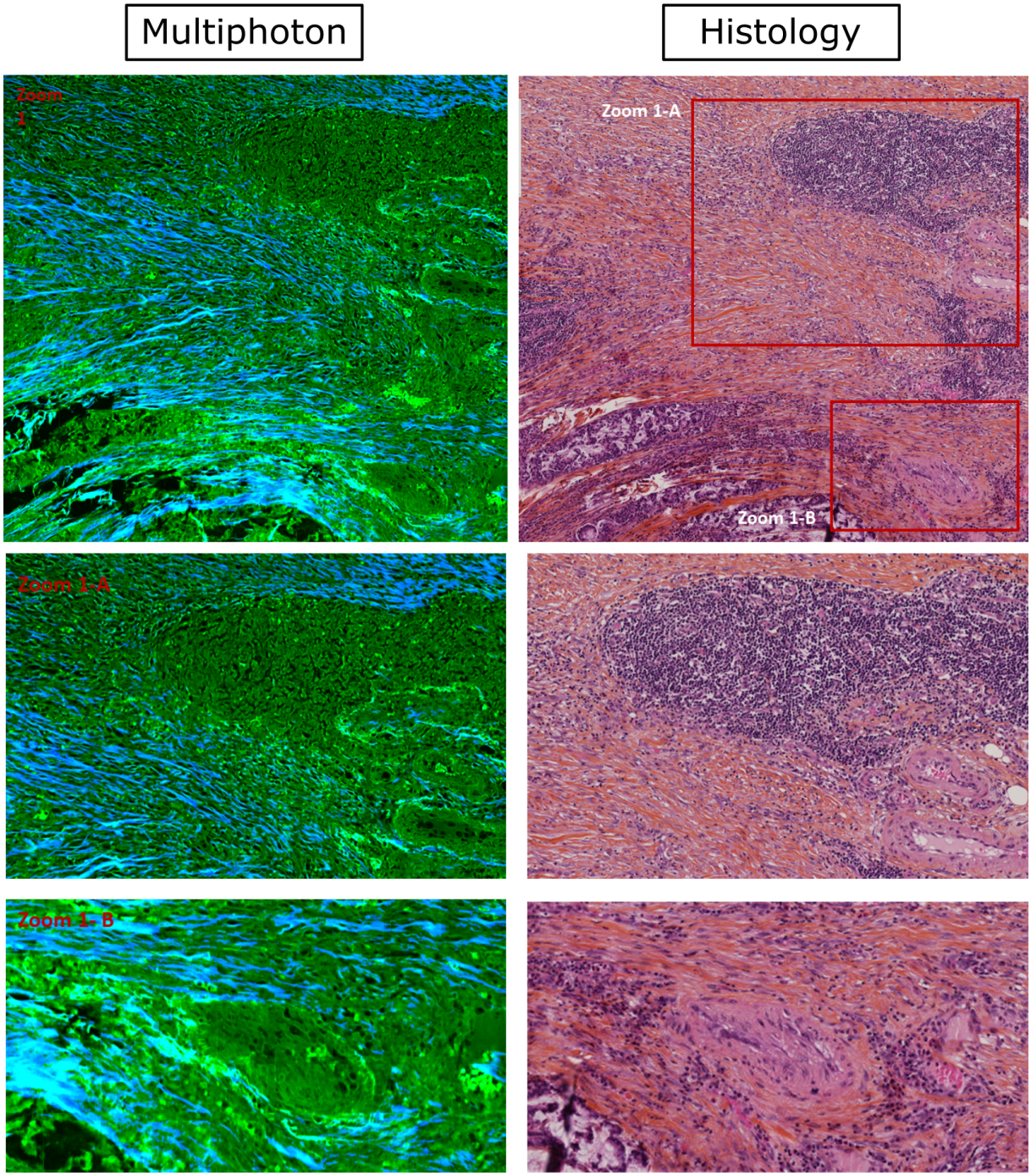

Figure 1.7: Comparison between TPEF/SHG imaging and histology visualization of a human colon tissue. SHG imaging highlights the collagen fibers in the extracellular matrix, while the TPEF response is given by proteins in the tissue. Image courtesy of Barbara Sarri and Rafael Canonge (Institut Fresnel).

exploited the CH_2 and CH_3 vibrations of lipids and proteins, as well as two-photon absorption of hemoglobin, to differentiate between normal and diseased tissue [44]. CARS imaging has revealed the mechanism behind the link in lipid accumulation and tumor progression, through the release of fatty acids that modify the physiology of tumor cells. Moreover, circulating tumor cells also show an excessive accumulation of lipid droplets, which could be exploited for detection of early-stage metastasis [80].

In TPEF/SHG images, certain important nuclear informations are missing, such as the nucleoli size and shape, chromatin condensation, and localization. In this sense, SRS microscopy could complement TPEF and SHG microscopy for histological analysis. A recent study has shown the capability of SRS microscopy to image the cells nuclei in live animals and fresh human tissues [91]. Three optimal Raman peaks were identified for cellular lipids (2854 cm^{-1}), proteins (2931 cm^{-1}) and DNA (2956 cm^{-1}). The SRS response of C-H bonds was used to retrieve the distribution of DNA in the tissue, retrieving it from the strong background of proteins and lipids by means of a linear decomposition method. This allowed authors to image chromosomes dynamics during cell division and present an optical histology method for human skin cancer diagnosis. SRS has been succesfully applied to image human and mouse brain tissues [65].

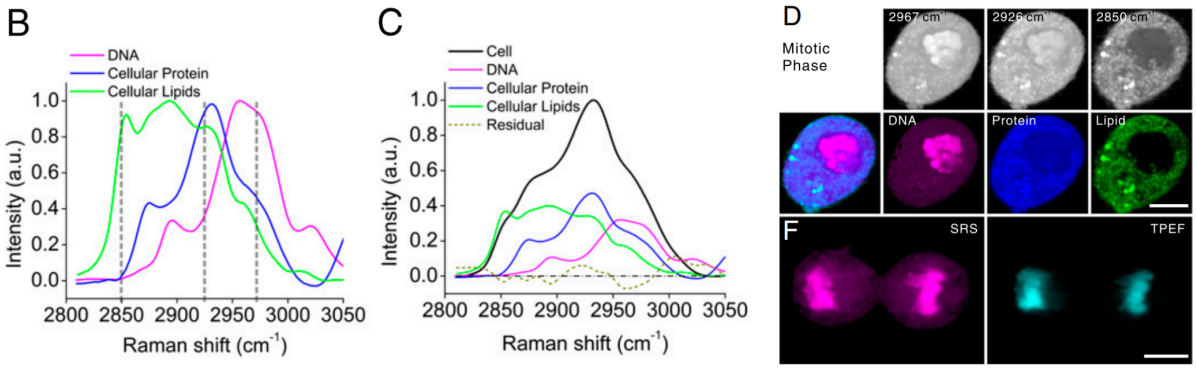

Figure 1.8: SRS microscopy allows the direct visualization of cells nuclei, a very important information for histological analysis. Taken from [91].

The authors of this work exploited the lipid and protein Raman resonances to discern between healthy and tumor-infiltrated tissues. The results were compared with histology H&E images and found a strong correlation for the detection of glioma infiltration. A combination of nonlinear microscopy, infrared, and Raman microspectroscopy was also used for brain tumor analysis [97].

Skin cancers have also been studied with multiphoton microscopy: König have used CARS in combination with TPEF and SHG to perform optical biopsy of human skin [75], while Mittal et al. applied SRS to identify squamous cell carcinoma in human skin [98].

Application of multiphoton microscopy is not limited to cancer detection, but has been used for different pathologies, such as different neurodegenerative diseases. Recent studies have been

carried out on the application of multiphoton imaging, including CARS, to image the progression of Alzheimer-related amyloid plaques [85, 70]. CARS microscopy is suitable to visualize myelin sheaths, dielectric materials that surround the axons of nerve cells and play a fundamental role for signal conduction. Myelin degradation plays an important role in neurodegenerative diseases, such as, such as Experimental Autoimmune Encephalomyelitis (EAE) and Multiple Sclerosis. Lipids contribute with 70 to 85% the dry mass of myelin sheaths. Axonal myelin was first imaged with CARS microscopy in live animals by Wang and coworkers [139]. Polarization-resolved CARS microscopy has been used, in combination with TPEF and SHG, to study the role and the morphological progression of demyelination and axon disorganization in such neurodegenerative pathologies [49].

1.2 Nonlinear endoscopy

The development of nonlinear endoscope probes is a crucial step for the translation of nonlinear imaging techniques into clinical routine. Several research groups have been working on the development of such probes in recent years, facing both mechanical and physical challenges. A nonlinear endoscope probe would ideally be a portable, light and miniaturized device, capable of reproducing, as close as possible, the performances of a nonlinear microscope. The design of nonlinear probes should ideally combine the following features:

- Small size, on the order of few millimeters in diameter.
- Flexibility and portability.
- Low electric voltage and current operation.
- Multimodality: simultaneous access to different contrast mechanisms (TPEF, SHG, CARS, SRS...).
- Large field of view (FOV).
- High spatial resolution.
- High frame rate (acquired images per second).

Such a probe would easily be integrated within current endoscopic technologies used in clinics. Forward viewing endoscopes are routinely employed for diagnostics (endoscopes) or guidance during surgery (laparoscopes). Colonscopes and gastroscopes are used for inspection of the gastrointestinal tract, while bronchoscopes are flexible endoscopes commonly used to inspect lungs. The working channels diameters in these endoscopes can be as large as $4.2\ \mathrm{mm}$ (colonscopes), $3.8\ \mathrm{mm}$ (gastroscopes) [137] or $3\ \mathrm{mm}$ (the BF-1T180 bronchoscope from Olympus).

An important issue in nonlinear endoscopy is represented by the delivery of ultra-short pulses. The theory of pulse propagation in optical fibers, and the implications for nonlinear endoscopes, will be treated in the next two chapters. However, we can here introduce the two most immediate issues. The first one is the temporal broadening of femtosecond pulses, due to group velocity dispersion (GVD) and self-phase modulation (SPM), which reduces the excitation efficiency and therefore the sensitivity of the probes. In order to reduce the risk of photodamage, efficient signal excitation has to be obtained with short pulse durations on the sample. Label-free TPEF and SHG in-vivo endoscopy has been recently demonstrated with miniature and portable probes [12, 32], thanks to the pre-compensation of propagation effects. The second problem concerns CARS endoscopy, because of a strong FWM background generated when the excitation beams propagate in solid core fibers [5]. This FWM background has hampered the development of miniature CARS probes so far.

Hereafter, we will discuss the different implementations of nonlinear micro-endoscopes, based on different beam scan techniques. Then we will review the advances and results of TPEF/SHG endoscopes in biological tissue imaging. The last part will discuss the efforts and state of the art in the development of miniaturized CARS endoscopes.

1.2.1 Remote imaging techniques

Different techniques can be employed to scan the excitation beams over a sample placed at the distal end[6] of an optical fiber. We can divide them in two classes: one relies on scanning elements placed at the distal end of a single-mode fiber, such as MEMS[7] mirrors or piezo-electric elements. In these systems the collection efficiency is usually enhanced by addition in the fiber of a double clad (DC) surrounding the delivery core. The other imaging approach is based on scanning elements (such as galvanometric mirrors) on the proximal end of a fiber bundle.

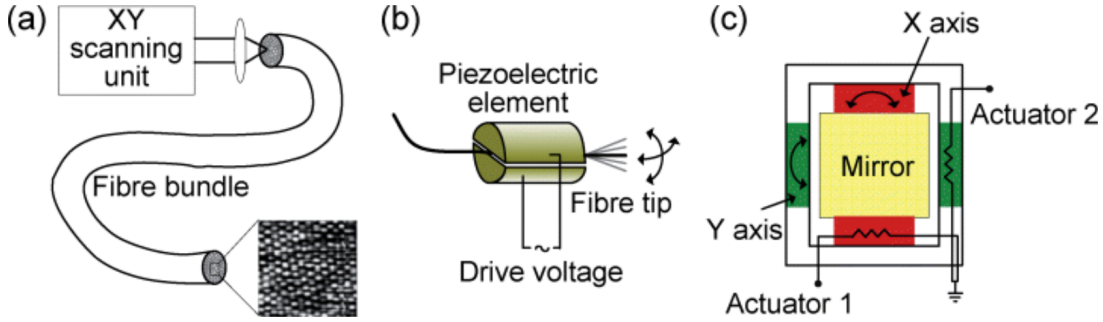

Figure 1.9: Different scanning mechanisms typically employed in NLO endoscopy. (a) Proximal scanning with a fiber bundle, (b) resonant scanning of the fiber tip and (c) beam scanning with a MEMS mirror [46].

[6] In endoscopy, the distal side of the fiber denotes the one close to the sample, where imaging is performed. The proximal side is where the fixed end of the fiber is, where light is injected and detectors are placed.

[7] Microelectromechanical systems.

Proximal scanning When using multicore fibers (also called fiber bundles), it is possible to preserve the information on the beam scan performed at the proximal end of the fiber. In fact, the beam can be coupled into individual cores, which act as point source of excitation light that is then focused onto the sample. Gobel et al. performed TPEF in-vivo endoscopy on labeled blood vessels with a fiber bundle coupled to a GRIN lens [52]. The lateral resolution is here limited by the interspacing distance between adjacent fibers. In order to increase the resolution, one must reduce the core-to-core distance, which increases the coupling between fibers and results in a degradation of imaging contrast. This coupling can be reduced using highly inhomogeneous fiber bundles.

Recent developments in the field have led to the development of lens-less ultra-thin rigid endoscopes, using proximal wavefront shaping. The control of the phase of the beam at the entrance of the optical fiber can produce a focused spot on the distal side, with no need for focusing optics. The position of the spot can be controlled as well. The size of the probe is limited by the fiber's dimension only, reaching diameters of less than 0.5 mm. Two types of fibers can be used for such endoscopes, multicore (see Andresen et al. [3], Conkey et al. [23]) and multimode fibers (see Papadopoulos et al. [109], Morales et al. [101], Sivankutty et al. [128]).

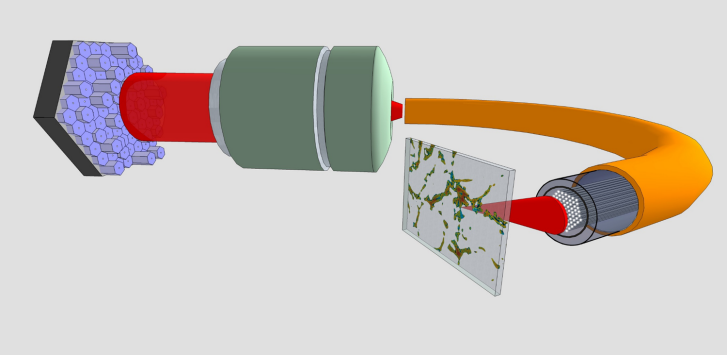

Figure 1.10: Wavefront shaping for lensless endoscopy through a multicore fiber. Image courtesy of Siddharth Syvankutty (Institut Fresnel).

MEMS based distal scanning One possibility to scan the beam at the distal end of a single delivery fiber is the use MEMS mirrors. These devices can have very small size (0.5 mm-2 mm) and achieve up to 30° rotation angles. MEMS mirrors are typically based on electrostatic or electro-thermal actuation and work with low drive voltages. They can be integrated in miniaturized probe, between the optical fiber and the focusing optics, to provide the beam scan. 2D scan is achieved with one single mirror, but it has to be coupled with another fixed mirror for frontal viewing, since it works at 45° (Fig. 1.11). Examples of nonlinear endoscope probes based on MEMS mirrors can be found in [47], [67] or [131].

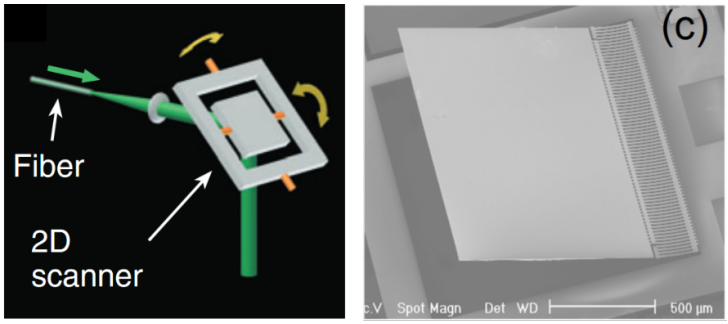

(a) (b)

Figure 1.11: (a) Beam scanning with a MEMS mirror [40] and (b) SEM micrograph of a MEMS mirror [47].

Piezo-electric based fiber-scanning One approach for beam scanning employs a piezo element to scan the fiber tip. The resonant scan of the fiber allows to obtain wide displacements using low driving voltages. Some miniature optical element is then used to refocus the beam onto the sample, where the scan pattern of the fiber is reproduced. Different types of piezo elements have been used, such as the piezo bending element in the miniaturized TPEF microscope developed by Helmchen et al. [59]. Four-quartered piezo-electric tubes offer a compact solution for 2D resonant scan. This is an easy-to-assemble solution which allows an important degree of miniaturization, and has been widely adopted for microendoscope probes [35, 105, 83, 32]. A precursor in this type of scan is the group of E.J. Seibel, from the University of Washington (see for example [124]). As we will see in Ch. 4, this is the solution we chose to adopt for the development of our nonlinear endoscope probe. The piezo-electric scan can be done in different configurations. One example is the resonant/non resonant system which uses two different piezo elements and generates a raster scan (the one used in microscopy). On this type of actuator is based the TPEF/SHG probe developed by Rivera and colleagues in Cornell University (USA) [116].

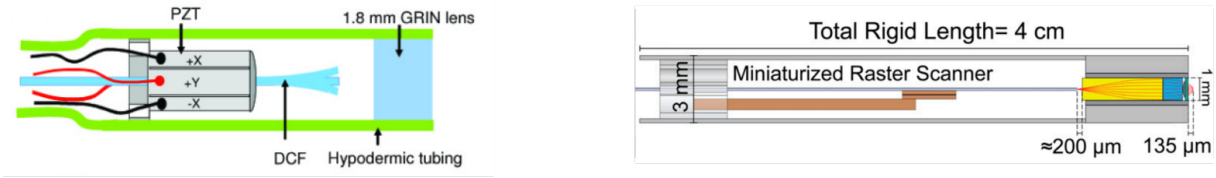

(a) (b)

Figure 1.12: Different types of piezo scanners. (a) Resonant scan based on a four-quartered piezoelectric tube [147]. (b) A resonant/non resonant scanner based on two different piezo-ceramic [116].

1.2.2 TPEF and SHG endoscopy

A variety of TPEF and SHG endoscope probes have been developed in the last decade. The pre-compensation of propagation effects for femtosecond pulses has allowed the development of endoscopes capable of accessing the two modalities with one single excitation wavelength. In-vivo nonlinear endoscopy has been first demonstrated in 2012 [12]. We will describe here the important results obtained with portable and miniature endoscopes on unstained tissues. We will not cover the results obtained on labeled tissues [6] or using GRIN lenses combined with multiphoton microscopes [89, 7] since these systems lack portability, although they have given interesting results in brain imaging in-vivo. The group of Xingde Li (Johns Hopkins University, Baltimore, USA) developed a piezo resonant scanning endoscope, using a customized DC fiber (Corning Inc.) and transmission gratings to compensate for the GVD introduced by the fiber [147]. The endoscope was used to monitor cervical remodeling during pregnancy in unstained ex-vivo murine and human cervical tissues (Fig. 1.13). The frame rate was 2.7 frames/second for a 110 µm diameter FOV, the images acquired with an incident power on the tissue sample of approximately 40 mW and 450 fs pulse duration [150]. The miniature, portable

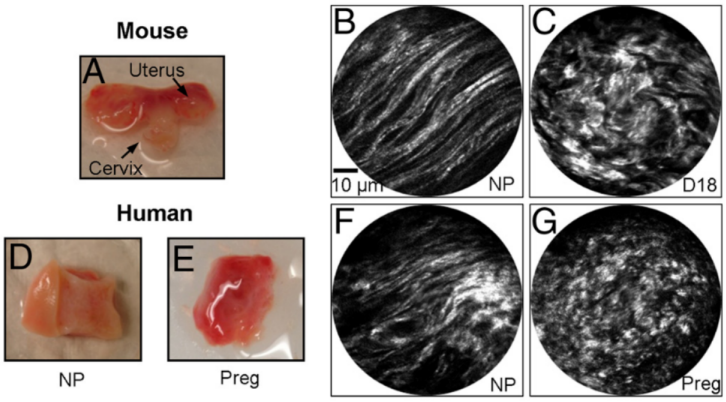

Figure 1.13: Observation of cervical remodeling in mouse (a) and human tissue (d)-(e) ex-vivo. SHG images show the morphological differences in the non-pregnant and pregnant (18 days mouse, 36 weeks human) tissues. Taken from [150].

endoscope developed by Rivera et al. [116] was the first to perform in-vivo nonlinear imaging of unstained kidney, liver and colon of an anesthetized rat [12]. The excitation pulses were delivered by a commercial DC optical fiber (DCF SM-9/105/125-20A, NuFern) with dispersion pre-compensation based on a prism pair. The pulse duration at the sample was measured to be 290 fs at 50 mW, with an initial duration of 100 fs. The FOV of the images measured 115µm x 115µm, imaged at 4.1 frames/s with 75 mW illumination power at the sample (Fig. 1.14).

The optimal pre-compensation of high-order dispersive and nonlinear effects, has allowed Ducourthial et al. to deliver sub-40 fs pulses onto the sample, after propagation in 5 m of a DC-PCF [32]. This has enabled the authors to perform in-vivo TPEF/SHG imaging of unlabeled

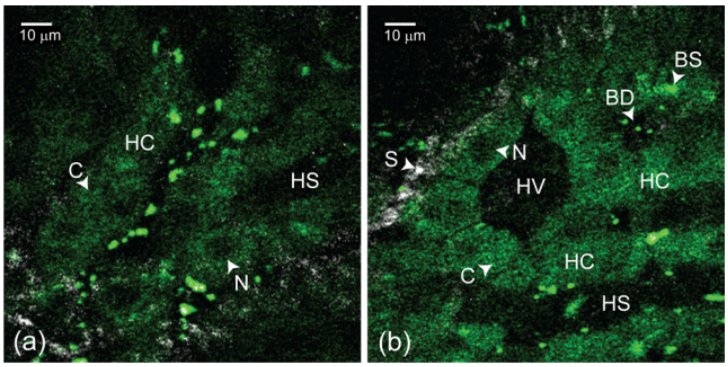

Figure 1.14: Unaveraged, unstained multiphoton endoscope images of rat liver located approximately 20 µm below the organ surface. The pseudo-color images show grey SHG signal (<405 nm) and green intrinsic fluorescent emission (420 to 690 nm). Taken from [12].

tissues, using a 2.2 mm diameter fiber scanning probe at 8 fps frame rate with 30 mW on the sample. These results are unmatched in present literature in terms of imaging speed and image contrast. Excitation at 810 nm highlights the collagen of the capsule (SHG) and the intracellular flavins of epithelial cells (TPEF) (Fig. 1.15), allowing in-vivo visualization of kidney fibrosis in the mouse.

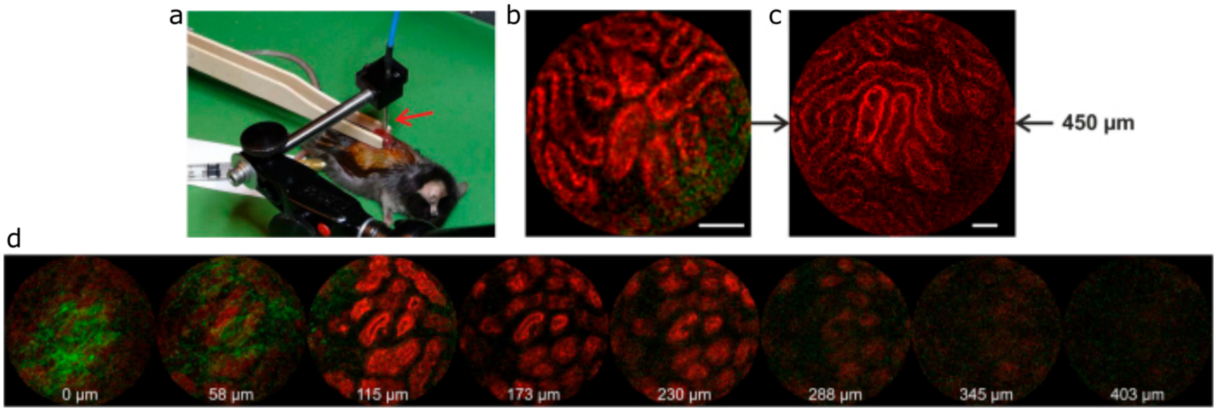

Figure 1.15: (a) In-vivo nonlinear imaging on an anesthetized mouse. Nonlinear excitation was obtained with a constant power of 30mW on the tissues. (b) and (c) SHG (in green) and TPEF (in red) raw image of respectively the collagen of the capsule and the intracellular flavins of epithelial cells of the kidney tubules. Scale bars 50 µm. (d) Successive optical sections of a fibrotic kidney. FOVs are 250 µm wide. Taken from [32].

1.2.3 CARS endoscopy

While TPEF/SHG endoscopes are already at a functional stage, CARS endoscopy is still facing technical challenges. In fact, while the picosecond pulses used for CARS imaging are less sensitive to dispersive and nonlinear broadening effects, meaning that pre-compensation schemes

are not necessary for few meters of fiber, a strong FWM background is generated in solid-core fibers [66] when delivering the excitation beams. This background largely overcomes the CARS signal collected from the sample, and strategies to suppress it have to be employed. This will be treated in detail in Sec. 3.2.2, but what matters here is that miniaturization of the probes is complicated by this background.

In 2011, Saar et al. [120] performed CRS imaging with a free-space system, based on a single mode fiber for pulse delivery, a piezo-tube for the scan, and a photodiode surrounding the focusing lens for SRS signal detection. In this work, CARS imaging was not performed in endoscope modality, but in forward detection. An issue with the $10\text{x}10\ \text{mm}^2$ photodiode for SRS, is that its size impairs medical applications. No mention of the background generated in the fiber was found in the paper. Although all the elements of the system were miniaturized, no portable version and further application has been reported by the authors since.

Balu et al. [5] developed a portable CARS probe, that incorporated a dichroic mirror to separate the FWM signal from the excitations beams delivered by the fiber. A separate fiber was used for signal collection and the probe, that incorporated galvanometric mirrors for beam scanning, had quite important dimensions (Fig. 1.16a, probe dimensions in cm). The portable microscope was used for CARS imaging of tissues (Fig. 1.16b to 1.16d).

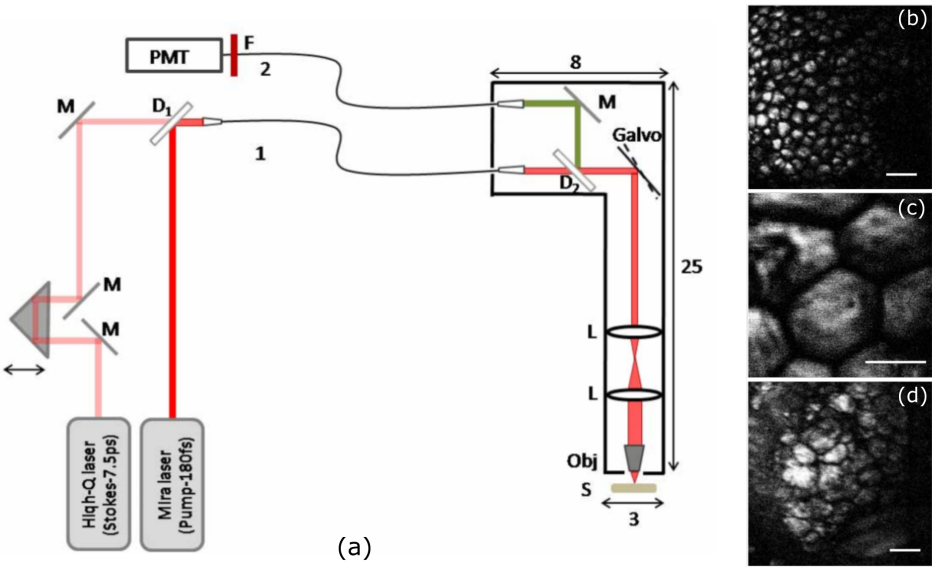

Figure 1.16: (a) The portable CARS probe developed by Balu et al. (the probe size is reported in centimeters). (b)-(d) CARS images of thick tissue samples ex-vivo at 2842 cm^{-1}. (b) Small adipocytes of mouse ear skin. (c) Adipocytes of subcutaneous layer of rabbit skin tissue. (d) Meibomian gland in mouse eyelid. Image acquisition time 2 s. Scale bar is 50 µm. Images taken from [5].

Smith et al. [129] reported in 2013 a CARS exoscope (too big to be an endoscope), using a MEMS scanner, separate fibers for beam delivery and signal collection and a dichroic mirror used to prevent the FWM from reaching the sample. With this system they were able to perform

CARS imaging of axons and fat cells, in the sciatic nerves of mouse tissues ex-vivo. An inter-

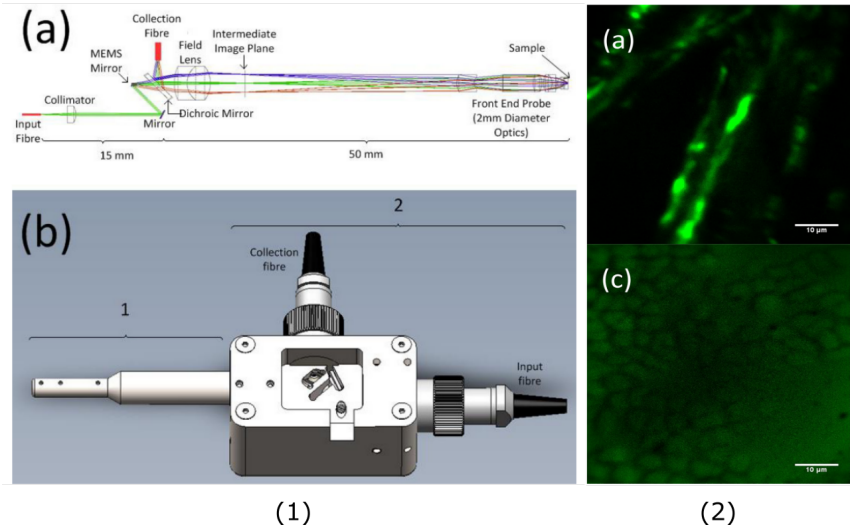

Figure 1.17: (1) Design of a CARS portable microscope, based on dichroic filtering of FWM background and separate delivery and collection channels. (2) Epi-CARS images obtained with the probe from a tissue ex-vivo: (a) Axons in the sciatic nerve of a mouse and (c) fat cells surrounding the sciatic nerve. Taken from [129].

esting approach was the one reported by Murugkar et al. [104], who developed a miniature CARS microscope based on a MEMS scanner, miniature optics and a single laser source. This solution provided a compact microscope capable of multimodal imaging of different tissues ex-vivo (in the forward direction). However, this system lacked the portability ideally required to an endoscope.

As we will see in Sec. 3.2.2, other strategies to suppress the FWM background have been recently proposed, that are compatible with a miniaturization of the probes to few millimeters in diameter [26, 18]. Deladurantaye et al. [26] performed endoscopic CARS imaging of polystyrene beads, with a fiber-scanning system. However, bulk optical elements (microscope objectives) were used to re-focus the beams from the fiber to the sample. Moreover, the images suffer from strong aberrations, especially when imaging on a relatively large FOV (Fig. 1.18c). Chen et al. [18] recently reported the development of a MEMS-based nonlinear probe, employing a polarization scheme for FWM background suppression. However, no nonlinear images were presented in the paper.

Fiber-optic Raman spectroscopy The development of efficient CARS and SRS probes, capable of combining vibrational imaging and spectroscopy, will profit from the knowledge and experience accumulated by spontaneous Raman spectroscopy clinical applications.
Raman spectroscopy for biomedical and clinical analysis is indeed a mature field, with Raman miniaturized fiber probes currently making their way into clinical applications. Raman based

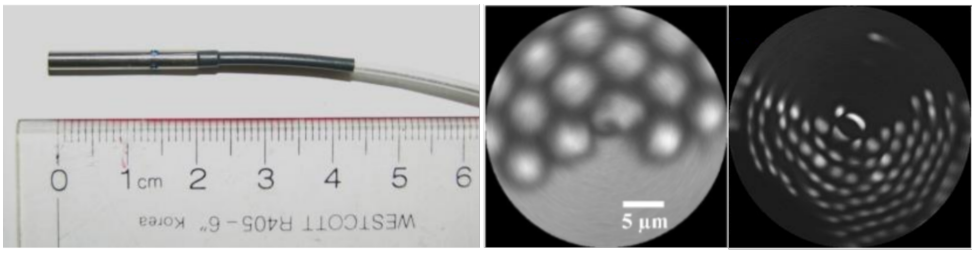

Figure 1.18: (a) Expected probe size of the miniature and portable CARS endoscope design from Deladurantaye et al. [26]. Epi-CARS images of (b) 5 µm and (c) 15 µm polystyrene beads, obtained using microscope objectives as focusing elements.

diagnosis of cancerous tissues has been reviewed by Krafft et al. [76], Chen et al. [17] and Tu et al. [135]. An interesting review of fiber probe Raman spectroscopy for real time optical biopsies of internal organs and tissues can be found in [141]. A more recent and up to date review of the current developments and applications of fiber-optic linear and nonlinear Raman techniques can be found in [79]. It is really worth citing a recent work, which reported the use of fiber optic Raman spectroscopy for intra-operative brain tumor detection, during surgery on a human patient [64].

1.3 Conclusions

In this chapter, we have introduced NLOM and its remarkable features for high-resolution, chemically-selective imaging of unlabeled biological tissues. The application of NLOM to biological tissues, shows what an impact these techniques could have as clinical diagnostic tools. However, translation of NLOM into clinics requires the development of miniaturized and portable probes, a road that is paved with a number of physical and technical issues. While TPEF and SHG probes are now at a developed stage, where in-vivo imaging can be performed with miniature (diameter ≈ 2 mm) and portable probes, CARS endoscopy has been limited so far by fiber delivery issues. Nevertheless, the development of miniaturized coherent Raman probes is of great interest, both to access the multimodality of NLOM and to combine in-vivo Raman spectroscopy with imaging.

Chapter 2

Pulse propagation in optical fibers

The fiber delivery of optical pulses emerged as a key issue in nonlinear endoscopy. In this chapter, we provide a theoretical introduction to some of the main effects occurring when ultrashort pulses propagate in optical fibers. We first discuss group velocity dispersion (GVD, Sec. 2.2) and self-phase modulation (SPM, Sec. 2.3), and the different outcomes of the interplay between these two phenomena (Sec. 2.4). Later on, we present cross-phase modulation (XPM, Sec. 2.5), an effect that occurs when two different pulses propagate in the same medium. To conclude, we introduce the split-step Fourier method, a popular approach for the numerical simulation of pulse propagation in optical fibers (Sec. 2.6).

2.1 Nonlinear pulse propagation

An optical pulse with central frequency ω_0 and spectral width $\delta\omega$ (where $\delta\omega << \omega_0$, a condition valid for pulses longer than 0.1 ps) can be treated in the so-called slowly varying envelope approximation [1]. This means that we can separate the pulse envelope from the fast oscillating part of the electric field (at frequency ω_0). The electric field can subsequently be expressed as:

$$E(\mathbf{r},t) = \frac{1}{2}\hat{x}[E_0(\mathbf{r},t)\exp(-i\omega_0 t) + c.c.] \tag{2.1}$$

Where $E_0(\mathbf{r},t)$ is the (slowly varying) amplitude envelope of the pulse. The electric field can be equivalently treated in the frequency domain, taking the Fourier transform of the time-dependent electric field:

$$\tilde{E}(\mathbf{r},\omega-\omega_0) = \int_{-\infty}^{\infty} E(\mathbf{r},t)\exp[i(\omega-\omega_0)t]dt \tag{2.2}$$

$\tilde{E}(\mathbf{r},\omega-\omega_0)$ has to satisfy the Helmotz equation:

$$\nabla\tilde{E}^2 + \epsilon(\omega)k_0^2\tilde{E} = 0 \tag{2.3}$$

where $k_0 = \omega/c$ and

$$\epsilon(\omega) = 1 + \tilde{\chi}_{xx}^{(1)} + \epsilon_{NL} \tag{2.4}$$

is the dielectric constant, that includes the nonlinear response term ϵ_{NL}, originating from the third order nonlinear susceptibility $\chi^{(3)}$.

The method of separation of variables can be used to solve the Helmholtz equation. It consists in assuming a solution of the form:

$$\tilde{E}(\mathbf{r}, \omega - \omega_0) = F(x, y)\tilde{A}(z, \omega - \omega_0)\exp(i\beta_0 z) \tag{2.5}$$

The electric field is here decomposed in different terms. The modal distribution function $F(x, y)$ represents the transverse profile of the electric field in the fiber and is constant in z, if we consider the case of a single propagation mode. The longitudinal term $\tilde{A}(z, \omega - \omega_0)$ is a slowly varying function of z and describes the pulse envelope in the frequency domain. This decomposition leads from the Helmholtz equation to two differential equations for the transverse and longitudinal components of the field. The pulse envelope $A(z, t)$ is the inverse Fourier transform of $\tilde{A}(z, \omega - \omega_0)$ and can be shown to follow the equation [1]

$$\frac{\partial A}{\partial z} + \beta_1 \frac{\partial A}{\partial t} + \frac{i\beta_2}{2}\frac{\partial^2 A}{\partial t^2} + \frac{\alpha}{2}A = i\gamma(\omega_0)\left|A\right|^2 A \tag{2.6}$$

Where $\beta_1 = \frac{\mathrm{d}\beta}{\mathrm{d}\omega}$. β_1 is the inverse of the group velocity ($v_{\mathrm{g}} = \beta_1^{-1}$), that represents the propagation speed of the center of the pulse. β is the propagation constant in the fiber and α defines the fiber losses. $\beta_2 = \frac{\mathrm{d}^2\beta}{\mathrm{d}\omega^2}$ is the GVD parameter. The nonlinear parameter γ is defined as:

$$\gamma(\omega_0) = \frac{n_2(\omega_0)\omega_0}{cA_{\mathrm{eff}}} \tag{2.7}$$

where the parameter A_{eff} is known as the effective mode area and can be exactly calculated if the modal distribution $F(x, y)$ is known, while n_2 is the nonlinear coefficient:

$$n_2 = \frac{3}{8n_0} Re\left\{\chi^{(3)}\right\} \tag{2.8}$$

Equation (2.6) can be written as

$$i\frac{\partial A}{\partial z} + \frac{i\alpha}{2}A - \frac{\beta_2}{2}\frac{\partial^2 A}{\partial T^2} + \gamma\left|A\right|^2 A = 0 \tag{2.9}$$

by using a frame of reference moving with the pulse at the group velocity $\mathrm{v_g}$, through the transformation

$$T = t - z/v_g \equiv t - \beta_1 z \tag{2.10}$$

Equation (2.9) is referred to as the Nonlinear Schrödinger Equation (NLSE). It describes the

propagation of optical pulses in fibers under the effect of GVD (β_2), SPM (γ) and fiber losses (α). This equation does not include higher order effects, such as SRS, self-steepening and higher order dispersion. Except for few specific cases, the NLSE doesn't lead to analytic solutions and a numerical approach has to be followed. One of the most used is the split-step Fourier method, which we will present in Sec. 2.6.

2.2 Group velocity dispersion

GVD is an effect originating from the wavelength dependency of the propagation constant β. Because of GVD, the different spectral components of a short pulse (which is not monochromatic) propagate with different velocities inside the fiber. Group velocity dispersion is described by the parameter:

$$\beta_2 = \frac{\partial^2 \beta}{\partial \omega^2}|_{\omega_0} = \frac{\partial}{\partial \omega}\frac{1}{v_g} = \frac{\partial \beta_1}{\partial \omega} \tag{2.11}$$

$\beta = \beta(\omega)$ is the frequency dependent propagation constant of the fiber. The GVD parameter β_2 is expressed in units of $[\mathrm{s}^2/\mathrm{m}]$. In the context of optical fibers, the GVD parameter is often expressed as a derivative with respect to wavelength. The dispersion parameter D_λ, generally given in units of $[\mathrm{ps}/(\mathrm{nm}\cdot\mathrm{km})]$ or equivalently $[\mathrm{fs}/(\mathrm{nm}\cdot\mathrm{m})]$, is defined as:

$$D_\lambda = -\frac{2\pi c}{\lambda^2}\cdot\beta_2 = -\frac{2\pi c}{\lambda^2}\cdot\frac{\partial^2 k}{\partial \omega^2} \tag{2.12}$$

β_2 and D_λ have opposite sign, since a longer wavelength corresponds to a smaller frequency.

The effect of GVD on a transform limited pulse[1] is to increase the pulse duration and introduce an instantaneous frequency variation (*chirp*). The duration $\tau(z)$ (defined as the FWHM of its temporal envelope) of an initially transform-limited Gaussian pulse after propagating over a distance z in a dispersive material is:

$$\tau(z) = \tau_0 \cdot [1 + (z/L_D)^2]^{1/2} \tag{2.13}$$

where τ_0 was the initial duration and the useful quantity

$$L_\mathrm{D} = \frac{\tau_0^2}{2.772\cdot|\beta_2|} \tag{2.14}$$

is called the **dispersion length**, which defines the propagation distance over which the pulse duration increases by a factor $\sqrt{2}$.
The factor 2.772 comes from the fact that L_D is usually defined in terms of the pulse half-width

[1] A pulse with the smallest time-bandwidth product. For a Gaussian pulse that is $\Delta t\cdot\Delta\nu \approx 0,44$, where Δt and $\Delta\nu$ are measured as the full-width at half maximum (FWHM).

at the 1/e-intensity point $\tau_{1/e}$[2]. Since the pulse duration is more often measured and expressed as the FWHM, our choice was to define the L_D accordingly. Equation (2.14) tells us that the temporal broadening of a pulse depends on its initial duration. For the same GVD parameter, the dispersion length is smaller for shorter pulses. From Eq. (2.13), it is clear that the broadening of a short pulse will be more pronounced, for the same propagation distance. This effect is due to the larger spectral width of shorter pulses.

The instantaneous frequency variation is proportional to the phase variation across the pulse [121]:

$$\delta\omega(z,T) = -\frac{\partial\phi}{\partial T} = \frac{2\beta_2 z}{\tau(z)^4 + \beta_2^2 z^2} T \tag{2.15}$$

The linear relation between time and frequency variation means that the GVD induces a linear chirp. It can be shown that the spectrum of a pulse is not affected by GVD (and even higher order dispersion) [121].

Two different situations exist: $\beta_2 > 0$ ($D_\lambda < 0$) is defined as the **normal dispersion** regime, where longer wavelengths travel faster than shorter ones ($\delta\omega < 0$ for $T < 0$, the leading edge of the pulse). When $\beta_2 < 0$ ($D_\lambda > 0$), blue components of the spectrum move at the leading edge of the pulse: this is called the **anomalous dispersion** regime. In a typical dispersion graph, a GVD parameter (either β_2 or D_λ) is expressed as a function of the wavelength (fig. 2.1).

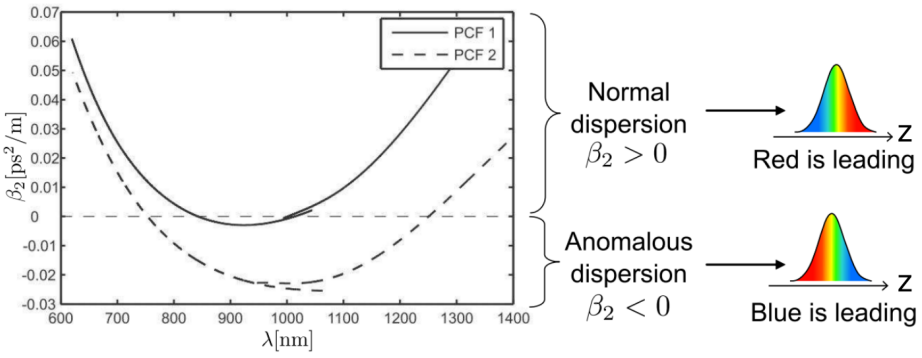

Figure 2.1: (a) The dispersion graph for two different PCFs, representing the GVD parameter β_2 as a function of the wavelength. (b) In the normal dispersion regime ($\beta_2 > 0$), red frequency components will lead in the pulse envelope, while in the anomalous dispersion regime ($\beta_2 > 0$) the blue components lead in the pulse. Taken from [121]. Graph: courtesy of Esben R. Andresen.

2.3 Self-phase modulation

SPM is an effect arising from the intensity dependence of the refractive index. It is responsible for spectral broadening of transform-limited pulses. From a physical point of view, SPM occurs

[2]For a Gaussian pulse: $\tau_{1/e} = \tau_{\mathrm{FWHM}}/2\sqrt{\ln(2)}$

when the pulse intensity is strong enough to modify the optical properties of the material it is propagating in. This causes an instantaneous, nonlinear variation of the phase across the pulse, which results in a modification of the pulse spectrum.

The intensity dependent refractive index can be expressed as [133]:

$$n(T) = n_0 + n_2 I(T) \tag{2.16}$$

where n_0 is the linear index, n_2 is the nonlinear coefficient (Eq. (2.8)) and $I(T)$ is the instantaneous intensity of the optical field. The magnitude of nonlinear effects is determined by the nonlinear parameter γ (Eq. (2.7)). For a typical single mode fiber, $\gamma \approx 20\ \mathrm{W^{-1}km^{-1}}$ ($n_2 \approx 2.6 \cdot 10^{-16}\ \mathrm{cm^2/W}$ in silica).
SPM induces a nonlinear phase shift ϕ_{NL} on the propagating pulse:

$$\phi_{\mathrm{NL}}(T) = n_2 I(T) \omega_0 L/c \tag{2.17}$$

The maximum phase shift occurs at the center of the pulse. After a propagation distance z, it is:

$$\phi_{\mathrm{NL,max}}(z) = \gamma P_0 z \tag{2.18}$$

where P_0 is the peak power of the pulse, which is related to the average power P_{avg}, the repetition rate f_R and the time duration τ of the laser:

$$P_0 = \frac{P_{\mathrm{avg}}}{f_{\mathrm{R}} \cdot \tau} \tag{2.19}$$

The nonlinear time-dependence of the phase $\phi_{\mathrm{NL}}(t)$ leads to a spectral modification of the pulse. This can be expressed as an instantaneous frequency variation across the pulse:

$$\delta\omega(z,t) = -\frac{\partial \phi_{\mathrm{NL}}(t)}{\partial t} = -n_2 \frac{dI(t)}{dt} \frac{2\pi}{\lambda} z \tag{2.20}$$

The frequency variation is inversely proportional to the gradient of the pulse intensity profile. The leading edge of the pulse (where $dI/dt > 0$) is red-shifted ($\delta\omega < 0$), while the trailing edge is blue-shifted (Fig. 2.2). The spectral broadening for an unchirped Gaussian pulse can be calculated, if we neglect dispersion ($\beta_2 \approx 0$), using [1]:

$$\delta\omega_{\mathrm{max}} = 0.86 \cdot \frac{\phi_{\mathrm{max}}}{T_0} \tag{2.21}$$

where T_0 was the initial pulse duration. For an unchirped Gaussian pulse T_0 is related to the initial spectral width of the pulse $\Delta\omega_0$, through: $T_0 = (\Delta\omega_0)^{-1}$.

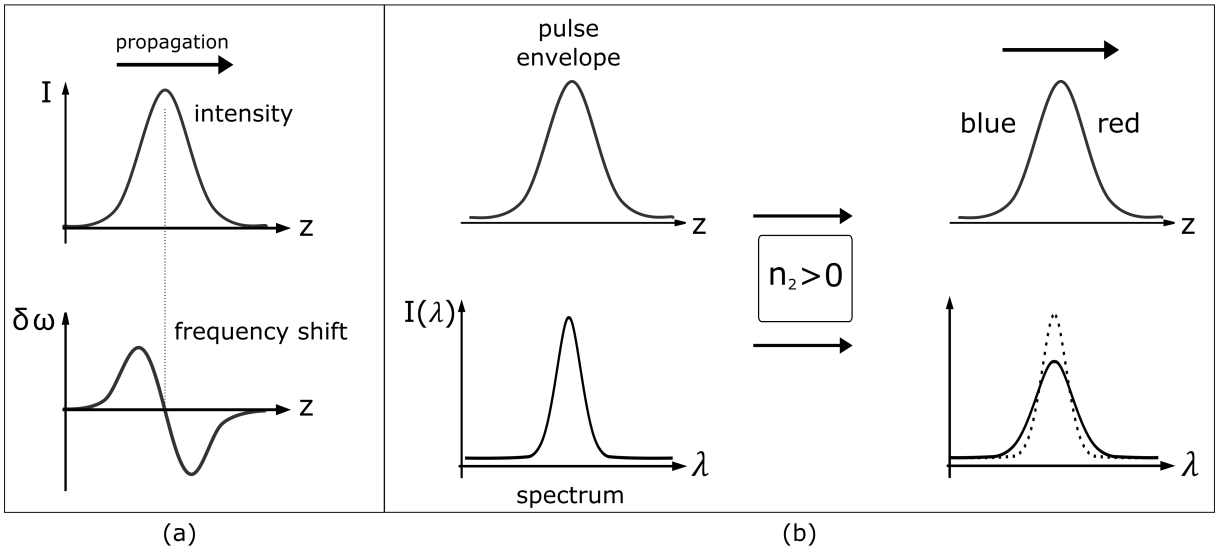

Figure 2.2: (a) SPM induced frequency shift for a gaussian pulse. (b) Spectral broadening, after propagation in a nonlinear medium, due to SPM.

Similarly to what done for GVD, it is useful to introduce a characteristic **nonlinear length**:

$$L_{\mathrm{NL}} \equiv (\gamma P_0)^{-1} \tag{2.22}$$

Then the maximum phase shift (defined in eq. (2.18)) can be written in terms of the nonlinear length $\phi_{\max} = z/L_{\mathrm{NL}}$. The nonlinear length defines the propagation distance ($z = L_{\mathrm{NL}}$) at which $\phi_{\max} = 1$.

2.4 Combined effects of GVD and SPM

We have seen that GVD and SPM can be responsible for the temporal and spectral broadening of transform limited pulses. The broadening occurs when they act together, in the normal dispersion regime ($\beta_2 > 0$), on transform-limited or positively chirped pulses. In this case, the temporal broadening is accelerated by the cooperation of the two effects. However, when a pulse propagate in the anomalous dispersion regime, the SPM-induced broadening can be compensated by GVD, leading to pulse compression. When the two effects cancel out each other ($L_{\mathrm{NL}} = L_{\mathrm{D}}$), the pulse remains transform limited as it propagates in the fiber and it is called an *optical soliton* (this effect can happen both in silica fibers [100, 122] and in hollow-core fibers [93]).

The net effect of GVD and SPM strongly depends on the initial pulse shape and chirp. For instance, the introduction of a negative chirp is often used to pre-compensate for the GVD induced by normal dispersion fibers. This is typically done with a pair of prisms or gratings, that

stretch the pulse in time with the higher frequencies at the leading edge. With a proper initial chirp the output from the fiber can be a transform-limited pulse. However when SPM acts on negatively chirped-pulses it leads to spectral compression: the higher frequency components at the leading edge of the pulse are red-shifted by SPM, while the lower frequency components at the trailing edge are being blue-shifted. For instance, the spectral compression of negatively chirped pulses, from 8.4 nm to 2.4 nm spectral width and a constant phase over the spectral and temporal profiles, was reported [145].

The reduction of the transform limited pulse duration is also possible (temporal compression). It can be done in two steps: first the pulse is spectrally broadened by SPM in a fiber in the normal dispersion regime. Then, the new frequency components are temporally compressed in a fiber with anomalous dispersion [132, 73].

2.5 Cross-phase modulation

Cross phase modulation (XPM) occurs when two optical fields propagate in the same medium. Similarly to SPM, the mechanism behind XPM is the intensity dependence of the refractive index. The physical picture is the following: a propagating pulse modifies the refractive index of a material, which is proportional to the instantaneous intensity of the pulse. This imposes on the other pulse an additional nonlinear phase shift, which is called XPM.

In other words, XPM occurs because the refractive index seen by one pulse depends on the intensity of the other one. XPM modifies the spectrum of the pulses, like SPM, but its effect changes with the relative delay between the pulses, as illustrated in Fig. 2.3.

Let us now call the two beams pump and Stokes, like for an SRS experiment. As the delay between the pulses changes, the pump beam might experience a positive (a) or negative (b) slope in the Stokes intensity profile. The sign of the slope will define the sign of the frequency variation. When the pump beam is leading (a), most of the pump pulse will experience a rising slope in the Stokes pulse, which is associated with a red-shift. Therefore, the XPM contribution to the nonlinear phase will cause the pump spectrum to shift to lower frequencies. When the pump beam is trailing (b), the negative intensity slope of the Stokes shifts the pump spectrum to higher frequencies.

Consider now the pump and Stokes fields, centered at frequencies ω_1 and ω_2 with intensities I_1 and I_2. The nonlinear phase acquired by the pulses as they propagate in the medium can be generally written as [1]

$$\phi_{\mathrm{j}}^{\mathrm{NL}}(z) = \gamma_j A_{\mathrm{eff}}(I_j + 2 \cdot I_{3-j})z \tag{2.23}$$

Where $j = 1$ or 2 and γ_j is defined as

$$\gamma_j = n_2\omega_j/(cA_{\mathrm{eff}}) \tag{2.24}$$

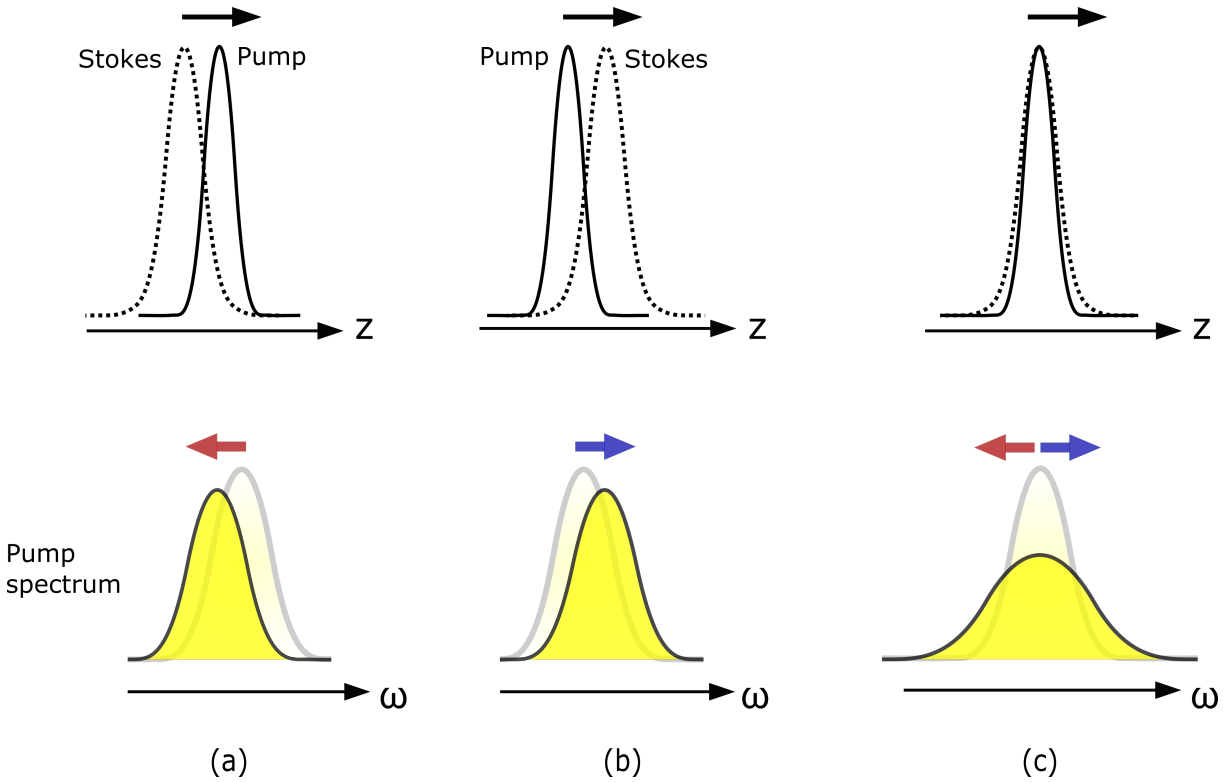

Figure 2.3: Spectral effects (bottom row) of XPM, as a function of the pulse delay (top row). Depending on the relative position between the Stokes (dotted line) and the pump beam, the spectrum can experience a red-shift (a), a blue-shift (b) or both ways (c).

The first term in Eq. (2.23) is responsible for SPM discussed in the previous section. The second term is responsible for XPM.

Similar to the single beam case, the NLSE describes the propagation of the pulse envelopes A_1 and A_2, under the effect of fiber losses, Kerr nonlinearity and GVD. Two coupled NLSE equations are written, taking into account the group velocity mismatch. If fiber losses are neglected, they take the form [1]:

$$\frac{\partial A_1}{\partial z} + \frac{i\beta_{21}}{2}\frac{\partial^2 A_1}{\partial T^2} = i\gamma_1\left(|A_1|^2 + 2\,|A_2|^2\right)A_1 \tag{2.25}$$

$$\frac{\partial A_2}{\partial z} + d\frac{\partial A_2}{\partial T} + \frac{i\beta_{22}}{2}\frac{\partial^2 A_2}{\partial T^2} = i\gamma_1\left(|A_2|^2 + 2\,|A_1|^2\right)A_2 \tag{2.26}$$

where time $\mathrm{T} = \mathrm{t} - \frac{\mathrm{z}}{\mathrm{v_{g1}}}$ is measured in a reference frame moving with the pulse traveling at speed $\mathrm{v_{g1}}$ and

$$d = \frac{v_{g1} - v_{g2}}{v_{g1}v_{g2}}$$

is a measure of group velocity mismatch between the two pulses.

In order to estimate the magnitude of the XPM-induced spectral broadening, one can at first neglect the GVD contribution to equations (2.25) and (2.26), and set $\beta_{21} = \beta_{22} = 0$. In such a case, the pulse shapes do not change and the equations can be solved analytically. The general solution, at z=L, is given by:

$$A_1(L,T) = A_1(0,T)e^{i\phi_1} \quad ; \quad A_2(L,T) = A_2(0,T-dL)e^{i\phi_2} \tag{2.27}$$

where the nonlinear phase shifts are

$$\phi_1(T) = \gamma_1\left(L\,|A_1(0,T)|^2 + 2\int_0^L |A_2(0,T-zd-T_{12})|^2\,dz\right) \tag{2.28}$$

$$\phi_2(T) = \gamma_2\left(L\,|A_2(0,T)|^2 + 2\int_0^L |A_1(0,T+zd-T_{12})|^2\,dz\right) \tag{2.29}$$

where $\mathrm{T_{12}}$ is the initial delay between the pulses and $\mathrm{z}\cdot\mathrm{d}$ is the time delay due to group velocity mismatch. The first contribution to the nonlinear phase is due to SPM, while the second one comes from XPM. The XPM contribution changes along propagation because of group velocity mismatch, then to obtain its total effect, it has to be integrated over the fiber length L. The dependence on the initial pulse delay of the XPM effects can be again understood in terms of Fig. 2.3.
This integration can be performed analytically for certain pulse shapes, such as that of unchirped Gaussian pulses. In that case, the maximum XPM-induced frequency chirp experienced by pulse

1 is [1]:

$$\Delta\,\omega_{\max}|_1 = \frac{2\gamma_1 P_2 L_W}{T_0} \tag{2.30}$$

where T_0 is the pulse duration (assumed equal for both pulses) and the walk-off length

$$L_W = T_0/\,|d| \tag{2.31}$$

defines the length over which the two pulses interact before being separated by GVD. The derivation of eq. (2.30) can be found in [1]. We will use this equation in Sec. 7.2 for an estimation of the frequency shift in a KagomÃľ fiber.

2.6 Simulation of nonlinear pulse propagation

In general, the NLSE does not lead to analytical solutions. Therefore, numerical methods have to be employed in order to simulate the propagation of short pulses under nonlinear and dispersive effects. The split-step Fourier method is one of the most used numerical tools for the purpose (see [63] and [127]). This method starts by rewriting the NLSE (Eq. (2.9)) as:

$$\frac{\partial A}{\partial z} = (\hat{D} + \hat{N})A \tag{2.32}$$

where we introduced the nonlinear operator $\hat{\mathrm{N}}$ and the dispersive operator $\hat{\mathrm{D}}$:

$$\hat{N} = i\gamma\,|A|^2 \quad ; \quad \hat{D} = -\frac{i\beta_2}{2}\frac{\partial^2}{\partial T^2} \tag{2.33}$$

Nonlinear effects and GVD act together on the pulse envelope $A(z,T)$ during propagation inside the fiber. If the fiber length L is divided in small steps h, the propagation from z to $z+h$ can be computed with:

$$A(z+h,T) \approx \exp(h\hat{D})\exp(h\hat{N})A(z,T) \tag{2.34}$$

The split-step Fourier method is based on the assumption that over the small length h, the two effects act independently. The dispersive step is more easily carried out in the Fourier domain, on the pulse envelope $\tilde{\mathrm{A}}(\mathrm{z},\omega)$. In the frequency space the dispersive operator can be evaluated by:

$$\exp(h\hat{D})B(z,T) = F_{\mathrm{T}}^{-1}\exp(h\hat{D}(-i\omega)F_{\mathrm{T}}B(z,T) \tag{2.35}$$

F_{T} is the Fourier transform which can be performed with the FFT algorithm, and F_{T}^{-1} is the inverse Fourier transform. The term $\exp(h\hat{D}(-i\omega))$ is a number, which can be easily computed by substituting the derivative $\frac{\partial}{\partial \mathrm{T}}$ by $-\mathrm{i}\omega$. Then the effect of dispersion over the length h is calculated as:

$$\tilde{A}(z+h,\omega) = \tilde{A}(z,\omega)\cdot\exp[h(-i/2\cdot\beta_2\omega^2)] \tag{2.36}$$

The field is then inversely transformed to the time domain, where the nonlinear effect is computed by including the nonlinear phase term on the field:

$$A(z+h,T) = A(z,T) \cdot \exp(h \cdot i\gamma |A|^2) \tag{2.37}$$

The repetition of these two steps over all the n steps (n=L/h), leads to the final field profile $A(L,t)$.

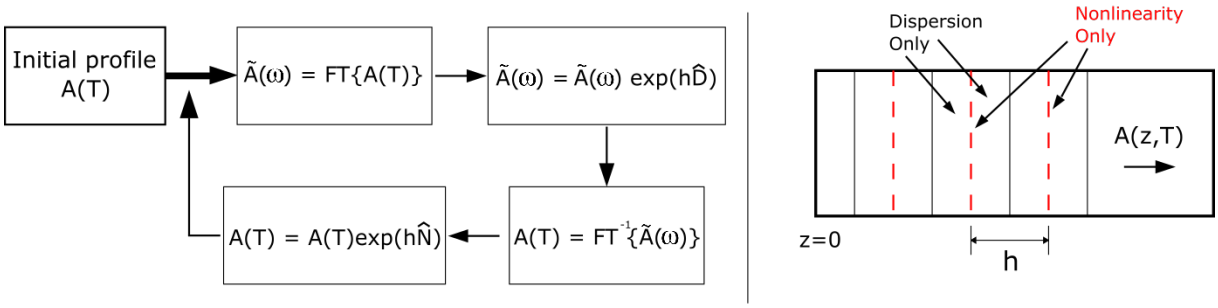

Figure 2.4: This figure illustrates the split-step Fourier method. On the left-hand side, the flow diagram of the algorithm. On the right-hand side, a graphical representation of the principle behind the method.

2.7 Conclusions

In this chapter we have laid the theoretical foundations of pulse propagation in optical fibers. We have first introduced the NLSE (Sec. 2.1), which governs pulse propagation under dispersive and nonlinear effects. We have then separately examined the effects of GVD (Sec. 2.2) and SPM (Sec. 2.3), introducing useful equations and parameters for the quantification of these effects. We have then analyzed the outcomes resulting from the interplay of dispersive and nonlinear effects, under different propagation conditions (Sec. 2.4). In Sec. 2.5, we introduced the effect of XPM, that occurs when two different fields propagate in the same medium. Finally we have presented the split-step Fourier method (Sec. 2.6), which is often used to simulate pulse propagation in optical fibers.

We will first use these concepts in Ch. 3, which is dedicated to the fiber delivery of femtosecond pulses for nonlinear endoscopy. They will be useful to examine the framework of the problem and the different strategies that have been employed for efficient nonlinear excitation at the distal end of optical fibers. They will also be applied in Ch. 7, where we will use Kagomé fibers to deliver picosecond pulses for SRS microscopy. We will see that XPM can play a role in the generation of a background signal in the Kagomé fiber. In the same chapter, we will adopt the split-step Fourier method to simulate pulse propagation and estimate the modulation transfer occurring in the fiber.

Chapter 3

Pulse delivery for nonlinear endoscopy

This chapter is dedicated to the problem of ultrashort pulse delivery in nonlinear endoscopy. We start with a review of the different types of optical fibers existing today (Sec. 3.1). The use of such fibers in nonlinear endoscopy is discussed in Sec. 3.2. We analyze here the the issues related to pulse delivery, such as the temporal broadening of the pulses and the CARS background generated in the fiber. In Sec. 3.3, we introduce a custom designed Kagomé-lattice hollow-core fiber for nonlinear endoscopy, describing its advantageous optical properties. In Sec. 3.4 we study the propagation effects on femtosecond pulses delivered by the Kagomé fiber. In the last section of the chapter (Sec. 3.5), we measure the FWM background generated in the fiber as a function of the delay between the pulses.

3.1 Optical fibers

An optical fiber is a cylindrical dielectric waveguide, that allows remote delivery of light by confining the optical field in a central region, which is called *core*. Guidance in classical optical fibers is based on total internal reflection (TIR), that is induced by a refractive index mismatch between the silica core and the region surrounding it, which is called *cladding*. Such fibers can be divided in two categories: *multimode* and *single mode* fibers. For our purpose we will restrict the description to the last ones.

3.1.1 Solid-core fibers

In classical optical fibers, a central core with refractive index n_1 is surrounded by a cladding of refractive index n_2, where n_1 is typically 1%-2% bigger than n_2 [41], which leads to a numerical aperture $\mathrm{NA} = (n_1^2 - n_2^2)^{1/2}$. Propagation in the fiber core is described by Maxwell's equations:

it is found that for a core radius a, a fiber will be single mode if the wavelength λ is such that the condition $V < 2.405$ is verified. The parameter V is defined as $V = (2\pi a\,\mathrm{NA})/\lambda$. If $V > 2.405$, the fiber supports multiple propagation modes and is called multimode.

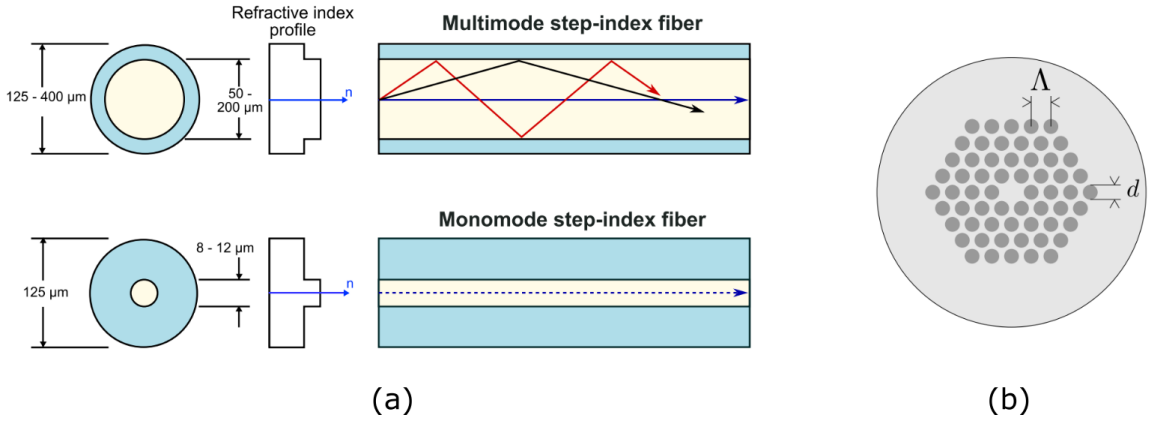

Figure 3.1: (a) Step-index fibers and (b) typical structure of solid core photonic crystal fiber. Adapted from [121], courtesy of Sarah Saint-Jalm.

Single mode fibers (SMF) These fibers are characterized by a small core size (few micrometers for visible light). Since only one propagation mode is supported, GVD is mainly due to the chromatic dispersion of the silica core. In silica, the GVD is +35 $\mathrm{fs}^2/\mathrm{mm}$ ($D_\lambda = -103\ \mathrm{ps}\cdot\mathrm{nm}^{-1}\cdot\mathrm{km}^{-1}$) at 800 nm and -26 $\mathrm{fs}^2/\mathrm{mm}$ ($D_\lambda = 21.8\ \mathrm{ps}\cdot\mathrm{nm}^{-1}\cdot\mathrm{km}^{-1}$) at 1.5 µm, with the zero-dispersion wavelength ($\beta_2 = 0$) located near 1.3 µm. Because of the small core size, nonlinear effects such as SPM can be quite important even at moderate power levels, because of the high electric field intensities, as we will see in Sec. 3.2.

Solid-core PCF A new class of fibers has been developed in the 1990s by the group of Philip St. J. Russell [117]: the Photonic Crystal Fibers (PCF). Such fibers are based on different confinement mechanisms than classical fibers, such as modified TIR or photonic bandgap (PBG) formation, and have opened many exciting perspectives for ultrashort pulse delivery. The first PCF consisted of a periodic array of air capillaries surrounding a central silica rod [71]. The guiding mechanism of this fiber is called modified total internal reflection (MTIR), since the effective refractive index of the photonic structure is lower than that of the core. Important parameters are the diameter of the capillaries d and the hole-to-hole distance (or pitch) Λ. For $d/\Lambda < 0.4$, a PCF exhibits an endlessly single mode behavior [118]. This is an advantage because the single mode condition depends only on the d/Λ ratio. Fibers with large core size can be produced by scaling the whole structure: they are called large mode area (LMA) fibers and typically have mode field diameter (MFD) larger than 10 μm. These fibers reduce the nonlinear

effects because of the larger core area Another advantage of PCFs is the possibility to tailor certain properties of the fiber, such as the dispersion, by changing d and/or Λ (this contribution is called the waveguide dispersion). In PCFs, the GVD can be positive or negative depending on the wavelength, and multiple zero-dispersion wavelengths (ZDW) are possible (Fig. 3.2b).

3.1.2 Hollow-core fibers

In a new type of fiber structure, the hollow-core (HC) PCFs, light is guided through an air-core, and the fraction of the field propagating in silica can be less than 1% [61]. As a consequence, the nonlinear coefficient n_2 in HC fibers can be 3 orders of magnitude smaller than in solid-core fibers [107]. The reduction of nonlinear effects is dramatic in this type of fibers. For this reason HC fibers are very attractive for high power laser delivery [125, 142]. Different type of HC fibers exist today, such as PBG fibers or Kagomé fibers.

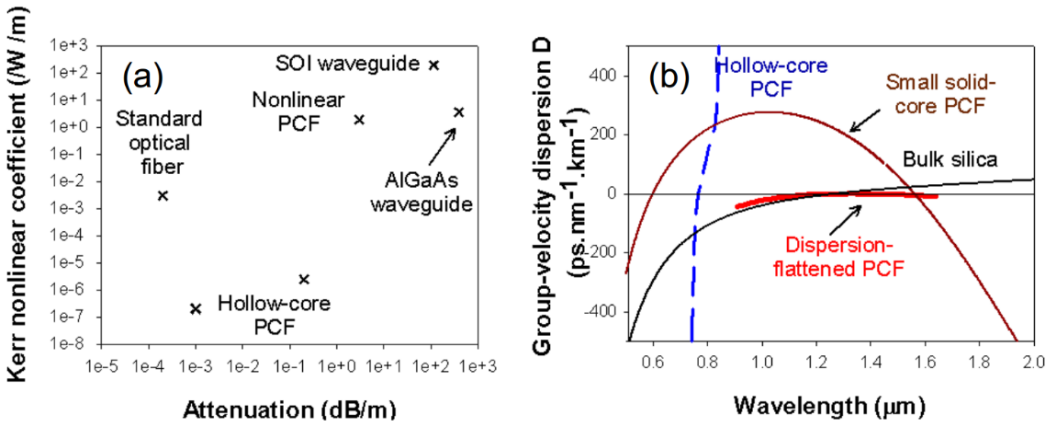

Figure 3.2: Nonlinear (a) and GVD (b) coefficients for different types of PCFs. Taken from [72].

Hollow-core PBG fibers When the silica core of a PCF is replaced by a hollow capillary with a different diameter than the ones in the photonic structures (usually bigger), light is guided because of the formation of photonic bandgaps[1] (PBG). The periodicity of the photonic structure inhibits propagation out of the core, for certain wavevectors k, which results in a low-loss confinement of light within a certain wavelength range. HC-PBG fibers (Fig. 3.3a) are characterized by a relatively narrow transmission window (typically < 100 nm). Within the transmission window, they take on both positive and negative GVD values, and the zero-dispersion wavelength (ZDW) is usually located at the center of this window. Distortion-less pulse delivery can be achieved when the pulse central wavelength is very close to the ZDW

[1]The name photonic bandgap highlights the analogy with the formation of forbidden electronic states (bandgaps) in periodic crystalline structures.

[53]. However, higher order dispersion is generally quite strong, which results in very steep GVD curves. Therefore, a strong dispersive broadening is experienced by pulses that are either very short in time (and large in spectrum), or centered at a wavelength different than the ZDW (see Fig. 3.2b, blue curve).

To summarize, HC-PBG offer single mode propagation with very low nonlinearity, but their main problem is related to the lack of spectral flexibility, due to the narrow transmission wavelength and the very steep GVD curves.

Kagomé fibers Kagomé-lattice fibers [24] are a very interesting type of hollow-core fibers. The fiber core is here surrounded by an air/glass microstructure whose pattern (the Kagomé lattice, Fig. 3.3b) resembles a Star of David. The photonic cladding does not exhibit PBG, and the guiding mechanism is based on a weak coupling between the core mode and the cladding modes (for a theoretical study see [110]).

Kagomé fibers generally have larger losses ($< 5\ \mathrm{dB/m}$) than HC-PBG fibers, but the low-loss transmission window is much broader ($> 400\ \mathrm{nm}$). The GVD in the Kagomé is also very low (few $\mathrm{ps \cdot nm^{-1} \cdot km^{-1}}$) over the whole transmission band. Kagomé fibers have been employed for high-power laser delivery for industrial applications, gas-based nonlinear optics [119], Raman spectroscopy probes [50].

New lattice designs, such as the hypocycloid-core Kagomé [143] (Fig. 3.3c), have led to improvements on the first Kagomé design, in terms of transmission losses and power handling (thanks to a smaller overlap between the field and silica). A new fiber design, called inhibited coupling (IC) Kagomé fiber has marked a record attenuation value of $7.7\ \mathrm{dB/km}$ at $750\ \mathrm{nm}$ and extremely broad low-loss transmission bands ($\mathrm{loss} < 20\ \mathrm{dB/km}$) spanning from $600\ \mathrm{nm}$ to $1200\ \mathrm{nm}$ [25].

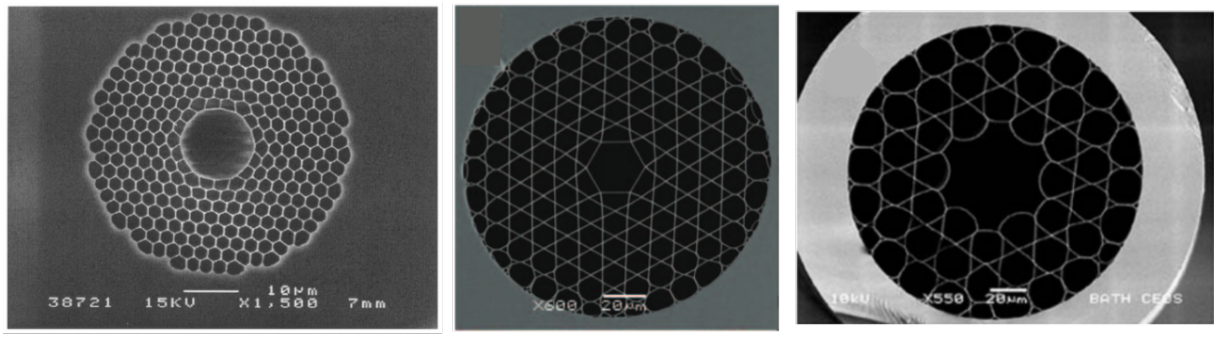

Figure 3.3: SEM micrographs of different HC-PCFs. (a) A HC-PBG fiber, (b) a Kagomé lattice HC fiber and (c) an hypocycloid-core Kagomé fiber. Images taken from [126], [24] and [143].

3.2 Fiber delivery in nonlinear endoscopy

The duration of the excitation pulses on the sample is a crucial element of nonlinear endoscopes. For an efficient endoscope, the dispersive and nonlinear effects associated to fiber propagation have to be taken into account, and compensated for most fiber types. This is true also for imaging fiber bundles, where the pulses propagate in separate SMFs. However, we will here focus on flexible endoscopes that employ a distal scanning mechanism, such as MEMS mirrors or piezo-element fiber scanning. In these systems, fibers supporting a single propagation mode, such as SMFs, small-core PCFs, LMA-PCFs or HC fibers, are generally used to deliver the excitation beams.

SMF are widely used in fiber-scanning endoscopes, where a second clad is added to increase the signal collection efficiency [12, 105, 147]. This double clad (DC)-SMF fibers are commercially available from several manufacturers. However, small-core PCFs are sometimes prefered over standard SMFs for different reasons [32]:

- Robust single mode propagation over all wavelengths.
- Double clad PCFs for endoscopy do not require addition of the dopants used in SMFs, that can absorb light and generate spurious TPEF signal.
- Adjustable GVD properties.

LMA fibers have been tested to reduce nonlinear effects in TPEF/SHG endoscopy [151] and are often used in CARS probes [5], because of the FWM background reduction [66]. HC-PBG fibers have also been used for femtosecond pulse delivery at the ZDW in two-photon microscopes [130] and in nonlinear endomicroscopes [35, 82], but also in CARS/SRS endoscope-like microscopy [13]. We will now separately discuss the problems related to pulse delivery in TPEF/SHG and CARS endoscopes.

3.2.1 Femtosecond pulse delivery

The pulse duration after the delivery fiber is an important issue in TPEF/SHG endoscopy, where a single optical pulse train is used for excitation. Shorter pulses are preferable for a more efficient activation of the nonlinear signal. Unfortunately, the broadening of femtosecond pulses can be quite strong even for short fiber lengths. The temporal broadening of a transform limited pulse can be estimated using Eq. (2.13). In SMFs, the GVD parameter is approximately $\beta_2 = +35\ \mathrm{fs}^2/\mathrm{mm}$ at 800 nm, which corresponds to a dispersion length $L_\mathrm{D} = 0.1\ \mathrm{m}$. After $1\ \mathrm{m}$ of propagation in a SMF, a transform limited $100\ \mathrm{fs}$ pulse will broaden to a duration of $993\ \mathrm{fs}$. At the same time, nonlinear effects act on the pulse: in a typical SMF the nonlinear parameter is $\gamma \approx 20\ \mathrm{W}^{-1}\mathrm{km}^{-1}$ [1]. A $100\ \mathrm{fs}$ pulse with 10 mW average power (on the order of the power levels used in NLOM), which corresponds to a peak power of $P_0 = 1000\ \mathrm{W}$ (for a $100\ \mathrm{MHz}$

repetition rate). Equation (2.22) allows the calculation of the nonlinear length, $L_{\mathrm{NL}} = 5\ \mathrm{cm}$[2]. These values highlight the importance of dispersive and nonlinear effects in optical fibers.

In order to compensate for the GVD of the fiber, a negative chirp is often introduced on the pulses before the fiber. This chirp is then compensated by the one acquired in the fiber, leading to a transform limited pulse on the sample. This chirp can be generated by means of gratings or prisms pairs, that stretch the pulse in time, with the blue frequencies at the leading edge. However, the optimal pulse delivery requires the pre-compensation of nonlinear effects as well. As already mentioned (in Sec. 2.4), negatively chirped pulses are spectrally compressed by SPM. Therefore, even if the pulses are transform limited, their output spectrum is narrower and their duration longer than the input ones [22]. Most notably, the output pulse duration increases with the delivered power, since SPM is an intensity dependent effect. This can lead to a saturation in the activation of the nonlinear signal, as the pulse duration increases with the excitation power [6].

Ducourthial et al. [32] demonstrated ultra-short pulse delivery through a small-core DC-PCF, by pre-compensation of SPM and higher order dispersion effects. The strategy consisted in using a single mode fiber to broaden the pulse spectra, pre-compensating for the spectral compression that takes place in the endoscope fiber. Then, a GRISM stretcher [134] was used to pre-compensate for second and third order dispersive effects. With this system, they reached sub-40-fs pulse duration on the sample, after 5 m of endoscope fiber. This probe was capable of imaging unlabeled tissues in-vivo, with moderate power levels and high frame rates (see Sec. 1.2.2). Murari and co-workers [103] developed a compensation-free endoscope probe by using

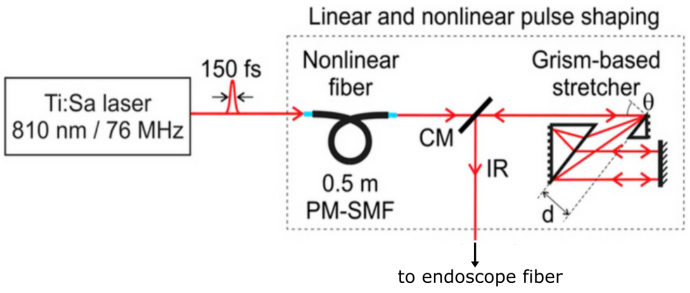

Figure 3.4: The efficient delivery of short pulses requires pre-compensation of both dispersive and nonlinear effects. In this figure, the pulse shaping setup developed by Ducourthial et al. to compensate for SPM, second-order and third-order dispersion [32].

a source at 1.5 µm, which falls in the anomalous dispersion region of the fiber and exploits soliton propagation.

HC-PBG fibers have been used in nonlinear endomicroscopes, with the femtosecond pulses delivered at the ZDW [35, 82]. One common feature of all this systems is their limited spectral tunability, which allowed them to efficiently operate either at a single wavelength or in a narrow

[2]The nonlinear length is the propagation distance that induce a spectral broadening $\delta\omega = 0.86 \cdot (T_0)^{-1}$

wavelength range.

3.2.2 Pulse delivery for CARS endoscopy

Pulse delivery in CARS endoscopes is affected by the problems described in the last section, especially when using femtosecond pulses. However, an additional issue exists in this case: a strong FWM signal is generated in the delivery fiber upon propagation of the pump and Stokes beams. This FWM background has represented the main issue in the development of Coherent Raman endoscopes so far. In solid-core fibers it can be very strong, generally overwhelming the signal collected from the sample [5]. We will now review the use of fibers for pulse delivery in CARS endoscopy.

SMFs have been used to deliver the pump and Stokes excitation beams, since picosecond pulses are less sensitive to GVD and nonlinear effects. Légaré et al. [86] found that for moderate power levels (80 mW for each beam), the SPM-induced broadening after 1 m of fiber was not compromising, in terms of spectral resolution and temporal duration. Saar et al. [120] also used a SMF for fiber delivered Coherent Raman imaging.

However, many groups have preferred to use LMA fibers, because they generate a lower FWM background as compared to SMFs [66]. However, this signal is non negligible even in LMAs. For instance, Balu et al. [5] used an LMA-PCF for beam delivery in their portable micro-endoscope. Here, the background peak generated in the fiber was found to be almost 10 times stronger than the CARS signal collected from a DMSO sample (Fig. 3.5). Filtering of this background was necessary, by means of a dichroic mirror and a separate collection fiber, which largely increased the size of the probe.

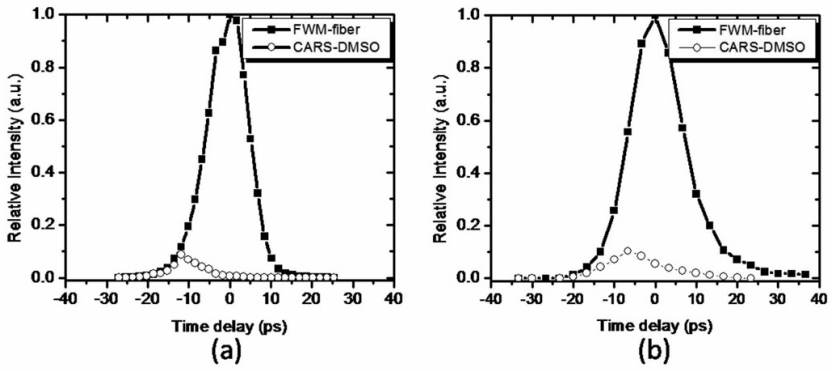

Figure 3.5: Comparison between the CARS signal intensity from a DMSO sample and the FWM generated in the fiber, as a function of the time delay between the pump and the Stokes beam. (a) The fiber is a DC-PCF (MFD = 16 μm, 80 cm long), (b) the fiber is a LMA (MFD = 16 μm, 50 cm long). Taken from [5].

Deladurantaye et al. [26] recently explored strategies to increase the imaging contrast in a CARS probe. First of all, they reported a 3 dB reduction in the FWM background in LMA

fibers, as compared to SMF fibers. They employed a LMA-DC fiber for pulse delivery and signal collection. They grew a micro-fabricated optical filter on the core, at the distal end of the fiber, to prevent the FWM background from reaching the sample. This reduced the FWM background in forward CARS images by 10 dB. However, reflection from the filter reduced the contrast in the epi images.

Other strategies to suppress the FWM background have been proposed. A very interesting approach is based on propagation of the pump and Stokes beams with orthogonal polarization in polarization maintaining fibers [144]. This scheme is able to suppress 99% of the FWM background in the fiber, but it requires a dual wavelength waveplate (DWW) after the fiber. Indeed, for efficient CARS excitation it is necessary to rotate the polarization of one beam, so that they are parallel on the sample. This scheme was adopted by the same group to develop a multimodal probe, although nonlinear images were not shown yet [18].

Another way to get rid of the FWM background is the use of HC-fibers. Brustlein and coworkers [13] have shown that this background becomes negligible when the excitation pulses propagate through an air-core. However, the accessible spectral region with this PBG fiber was limited to 1800 cm^{-1}, not reaching the interesting lipid region.

3.3 Kagome fiber for nonlinear endoscopy

In this thesis, we propose the use of a Kagomé DC fiber for nonlinear endoscopy. Kagomé fibers are hollow-core fiber with a broad low-loss and low-GVD band. Their transmission properties allow the delivery of excitation pulses over a very large wavelength range. When performing Coherent Raman imaging, vibrational frequencies as high as $4000\ \mathrm{cm}^{-1}$ can be covered. We will see in the following sections that the development of a multimodal non-linear endoscope is simplified by the use of this fibers, whose properties are:

- Low (and anomalous) GVD.
- Small nonlinearities ($\mathrm{n}_2^{\mathrm{air}} \approx 10^{-3} \cdot \mathrm{n}_2^{\mathrm{silica}}$).
- Broad spectral tunability (transmission band with similar dispersive properties, no frequency-specific pre-compensation systems required).
- Negligible FWM background generated in CARS modality.

The optical properties of the Kagomé fiber are shown in Fig. 3.6. Light propagates in a single mode (Fig. 3.6a) through the fiber hollow core (Fig. 3.6b). The mode field diameter is $\approx 18\mu\mathrm{m}$ for a measured NA of 0.02. The transmission window for the air guided mode extends from $680\ \mathrm{nm}$ to $1100\ \mathrm{nm}$, where the attenuation is lower than $5\ \mathrm{dB/m}$ (Fig. 3.6c). The minimum reaches about $2\ \mathrm{dB/m}$ between $800\ \mathrm{nm}$ and $1000\ \mathrm{nm}$, which is acceptable, considering the fiber design parameters. The Kagomé fiber can efficiently deliver pump and Stokes beams that

cover very high vibrational wavenumbers (up to 4000 cm^{-1}). In Fig. 3.6c, the wavelengths 800 nm and 1040 nm are highlighted, since they correspond to the pump and Stokes excitation wavelengths for CARS imaging of lipids in many OPO systems.

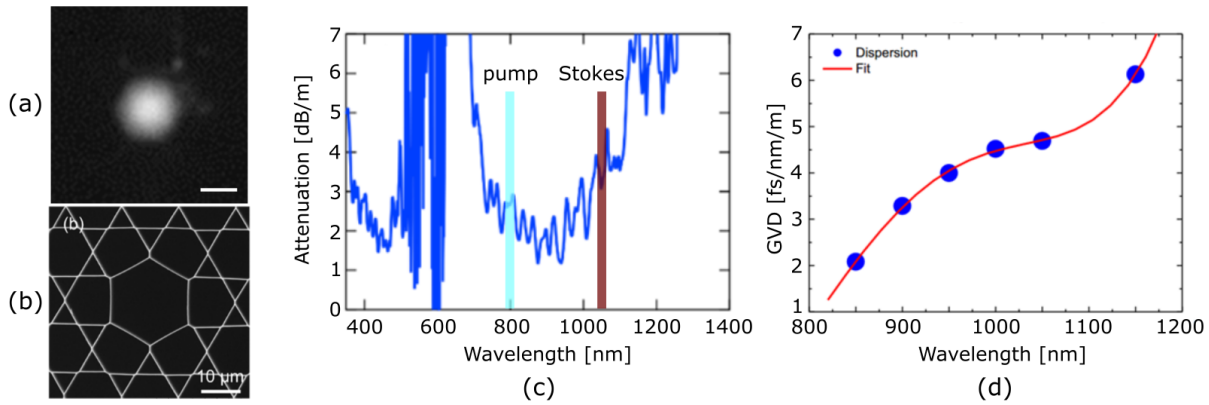

Figure 3.6: (a) Propagation mode of the Kagomé fiber, with scale bar 10 µm and (b) SEM image of the core and the surrounding photonic micro-structure. (c) Transmission spectrum of the fiber, highlighting the wavelength of the pump and Stokes beams for CARS imaging of lipids (2854 cm^{-1}). (d) GVD curve of the fiber.

The GVD was measured from 800 nm (1 $\mathrm{ps \cdot nm^{-1} \cdot km^{-1}}$) to 1150 nm (6 $\mathrm{ps \cdot nm^{-1} \cdot km^{-1}}$) and is shown in Fig. 3.6d. The dispersion lengths for the pump (800 nm) and Stokes (1040 nm) wavelengths are $L_\mathrm{D} = 10$ m and $L_\mathrm{D} = 2.4$ m ($\beta_2 = 4.5$ $\mathrm{ps \cdot nm^{-1} \cdot km^{-1}}$ at 1050 nm), which are extremely low GVD values, if compared to other fibers, especially for such a broad transmission band. Moreover, the chirp induced by the fiber comes from anomalous dispersion, advantageously compensating for the normal dispersion introduced by the preceding optical elements.

3.4 Propagation effects on femtosecond pulses

Knowing the optical properties of the Kagomé fiber, we expect that dispersion and nonlinearities have negligible effect on femtosecond pulses for propagation lengths of few meters only. In this section we will present the measurement of temporal and spectral effects, associated to the propagation of femtosecond pulses in the Kagomé fiber.

Temporal effects

This experiment was performed using a Ti:Sa laser (Chameleon, Coherent). We measured the pulse duration, before and after the fiber, for different pulse wavelengths, using an autocorrelator (Mini USB, APE). The input duration was measured before lens L1 (see Fig. 5.1). The output pulse duration was measured after propagation in 1 m of Kagomé fiber and collimation with a 25 mm lens. The results of the experiments are shown in Fig. 3.7. The input pulse duration

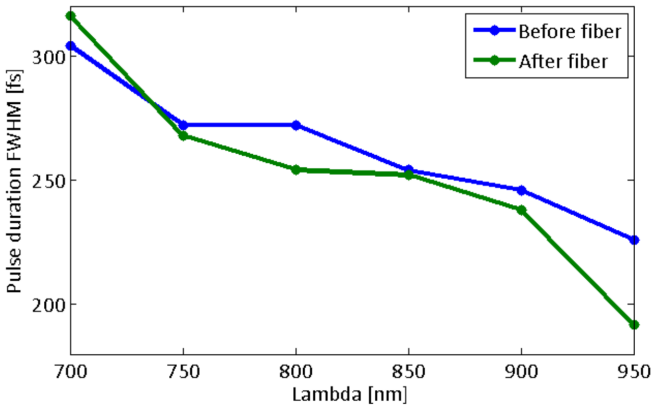

Figure 3.7: Pulse duration for different wavelengths of a Ti:Sa laser, measured with an autocorrelator. Measurements were performed before (blue curve) and after (green curve) 1 m of Kagomé fiber. The pulses do not experience significant temporal broadening, while temporal compression occurs at 950 nm.

was not uniform across the Ti:Sa spectrum. This might be due to the GVD experienced by the pulses in the glass elements of the optical setup, such as the coupling objective or the thick polarizing beamsplitters. In classical single mode fibers, femtosecond pulses of this duration would experience an important broadening, since the 700 nm - 950 nm spectral region is in the normal dispersion regime. On the contrary, the pulse duration is shorter after propagation in the Kagomé, apart from the pulse at 700 nm. This is not a surprise, since the GVD of the fiber is very low, but lies in the anomalous regime. Therefore, the chirp induced by the fiber compensate for any positive chirp introduced by preceding optical elements. This seems to be confirmed by the measured GVD values for the Kagomé (Fig. 3.6d), which are higher at longer wavelength. In fact, the strongest temporal compression occurs at 950 nm where the GVD is $4\ \mathrm{ps} \cdot \mathrm{nm}^{-1} \cdot \mathrm{km}^{-1}$. At the same time, the pulses experienced a slight broadening at 700 nm. The GVD was not measured at this wavelength, but the trend of the dispersion curve suggests that pulses at 700 nm experience normal dispersion in the fiber.

Spectral effects

Nonlinear effects such as SPM can alter the spectrum of the pulses. The effect is proportional to the peak power of the pulse and to the nonlinear index n_2 (Eq. 2.22). In the Kagomé fiber we expect this effect to be negligible for the pulse intensities used in nonlinear endoscopy. We used a spectrometer (USB4000, Ocean optics) to estimate pulse broadening of a 100 fs pulse. The spectrum of the beam, before and after propagation in 1 m of Kagomé fiber, was measured for different power levels (Fig. 3.8). We can conclude that, at the power levels used in endoscopy, the effect of SPM is negligible on 100 fs pulses propagating in the Kagomé fiber.

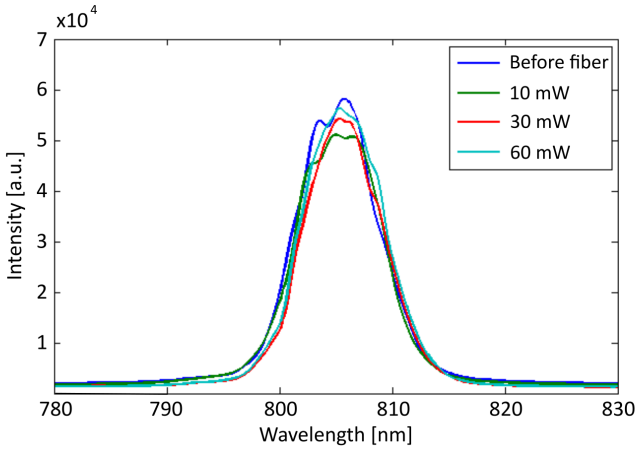

Figure 3.8: Spectrum of the pulse centered at 805 nm, measured before and after delivery through 1 m of Kagomé fiber, for increasing power levels. No detectable spectral broadening was measured, upon propagation in the hollow-core fiber.

Efficient broadband excitation

The capability of a Kagomé fiber to delivery undistorted short pulses has important implications for applications in spectroscopy. In fact, pre-compensation mechanisms used to obtain short pulse durations at the sample are generally optimized for a single wavelength, or a narrow wavelength range. This is a limit in situations where a fast tuning of the excitation wavelength is required. Pulse delivery with Kagomé fibers does not require GVD pre-compensation, and the following experiment illustrates another benefit of this feature. We performed fiber delivered two-photon excitation (TPE) spectroscopy of a fluorescein (FITC) solution, exploiting the broad transmission window of the Kagomé.

TPE spectra are often expressed in terms of the two-photon cross section, a wavelength-dependent parameter that defines the probability for a molecule to undergo TP absorption. The cross-section is conveniently expressed in units of GM[3], and is proportional to the TPEF intensity [148]:

$$I_{\mathrm{TPEF}} = K \cdot \sigma_{\mathrm{TPE}} \cdot I_{\mathrm{exc}}^2 \tag{3.1}$$

Where K is a parameter that takes into account the illumination and signal collection conditions, together with the concentration of molecules in the focal volume. I_{exc} is the excitation beam intensity and I_{TPEF} is the TPEF signal.

The TPE cross section of fluoresceine was measured by Albiota *et al.* and can be found in [2]. Because of the linear dependence in Eq. (3.1), we expect a correlation between the TPEF signal and the TPEF cross-section. In order to verify this, we excited a homogeneous FITC solution (50 mM) with femtosecond pulses delivered by 1 meter of Kagomé fiber, using a constant power of 5 mW on the sample. As we swept the laser wavelength, with 25 nm steps (from 975 nm to

[3]In honor of Maria Goppert Mayer. 1 GM=10^{-50} cm^{4}s/photon

690 nm), we integrated the TPEF signal over 1 s. The fluorescence signal was filtered using a bandpass filter (550/100 nm). The results are shown in Fig. 3.9, where a semi-logarithmic graph

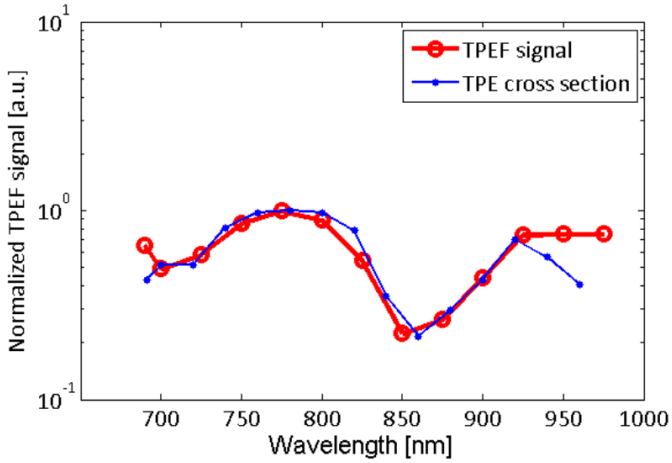

Figure 3.9: Red curve: normalized TPEF signal from an homogenous fluorescein solution with the excitation beam delivered by the Kagomé. Blue curve: normalized TPEF cross section of fluorescein in water as tabulated by Albota et al. [2].

plots the normalized cross-section (blue curve) and TPEF signal (red curve) as a function of the excitation wavelength. The wavelength dependency of the TPEF signal is in good agreement with the reported values of the FITC cross-section, apart from deviations at 690 nm and high wavelengths.

This indicates that the Kagomé fiber is suitable for multi-wavelength excitation with femtosecond pulses, something that would require much more complicated arrangements, when using classical single mode fibers.

3.5 Study of the FWM background

In the section dedicated to CRS processes (Sec. 1.1.2) we described FWM, a parametric process that generates signal at the CARS wavelength λ_{CARS}:

$$\lambda_{\mathrm{CARS}} = (\frac{2}{\lambda_{\mathrm{P}}} - \frac{1}{\lambda_{\mathrm{S}}})^{-1} \tag{3.2}$$

Where λ_{P} and λ_{S} are the pump and Stokes wavelength. As already discussed, FWM originates from the non-resonant part of the nonlinear susceptibility ${\chi_{\mathrm{NR}}}^{(3)}$ and represents an unwanted background in CARS microscopy.

As already discussed, this background has represented the main issue for the development of portable CARS endoscope probes so far. This is because the magnitude of the FWM signal generated in the delivery fiber largely overcomes the CARS signal that one collects from the

sample [5].

FWM requires the temporal overlap of the excitation beams. Therefore, we study the signal generated at λ_{CARS} upon propagation in the Kagomé fiber, as a function of the relative delay between pulses.

3.5.1 Background in Kagome fibers

For the experiments of this section we used a compact two-wavelength femtosecond fiber laser source (FemtoFiber dichro bioMP, TOPTICA). The laser pulses were ≈ 100 fs in duration (value given by the manufacturer), with spectra centered at λ_{P}=780 nm and λ_{S}=1031 nm. The FWM signal generated at a wavelength λ=627 nm was filtered with a short-pass filter (690 nm), a band-pass filter (629/53 nm) and detected using a photon-counting PMT (H7421-40, Hamamatsu). The beams were coupled in 1 m of Kagomé fiber, with a coupling efficiency of about 15% in the Pump and 8% in the Stokes, resulting in 12 mW (780 nm) and 8 mW (1031 nm) of power delivered by the fiber. Unfortunately, a slight misalignment in the beams propagation, which was not corrected in this implementation, caused an imperfect overlap of the beams when coupling in the fiber. For this reason, the fiber core had to be aligned in a position in-between the maximum efficient coupling for the two beams. We measured the signal as a function of

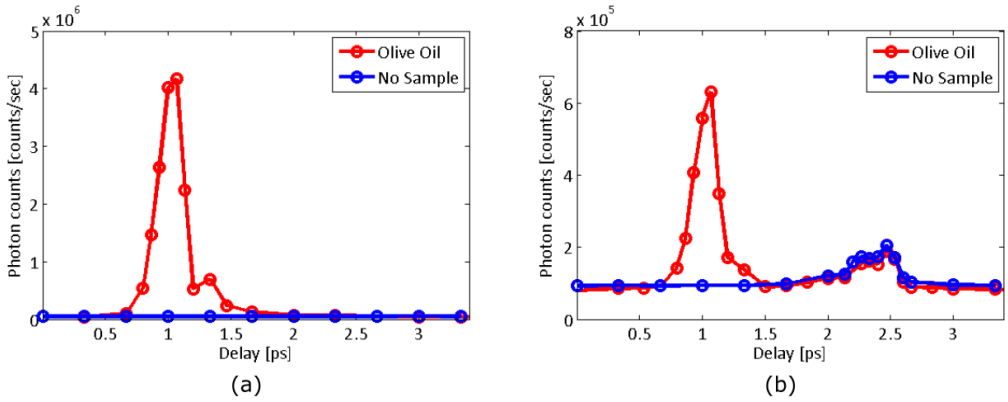

Figure 3.10: FWM signal generated in the Kagomé fiber in the forward (a) and epi directions (b) as a function of the delay between the Pump and Stokes beams. The blue curves show the FWM signal due to propagation in the fiber, while the red curves represent the detected signal when an olive oil solution is placed in the sample plane.

the delay between pulses (Fig. 3.10), both in the epi and forward directions. This signal was compared with the CARS/FWM signal generated by olive oil, which was placed after two back-to-back microscope objectives used to collimate and focus the excitation beams on the sample. In the forward direction a variable neutral density (ND) filter (transmitted power 3%) was used to avoid saturation of the detector from the CARS signal of the olive oil.

The group velocity mismatch in the microscope objectives induced a delay between the pump and Stokes pulses. This caused the temporal overlap on the sample (at 1 ps) to be separated from

the overlap in the fiber (between 2 and 2.5 ps). No signal generated in the fiber (blue curve) was detected in the forward direction, while in the epi direction a small signal was detected. However, this background is smaller than the signal generated in olive oil and might be due to the imperfect coupling of the beams in the fiber, as shown by the following experiment.

Photonic crystal structure The photonic structure surrounding the core is partly made of silica and might contribute to the generation of FWM background. In order to investigate this, we slightly misaligned the incoming beams on the fiber. The total power delivered the fiber was reduced from $20\ \mathrm{mW}$ to $4.5\ \mathrm{mW}$. The beams were still coupled in the core, but a portion of the field was incident (and would eventually propagate) in the photonic structure. The image of the distal end of the fiber is shown in Fig. 3.11a, before (top) and after (bottom) the misalignment.

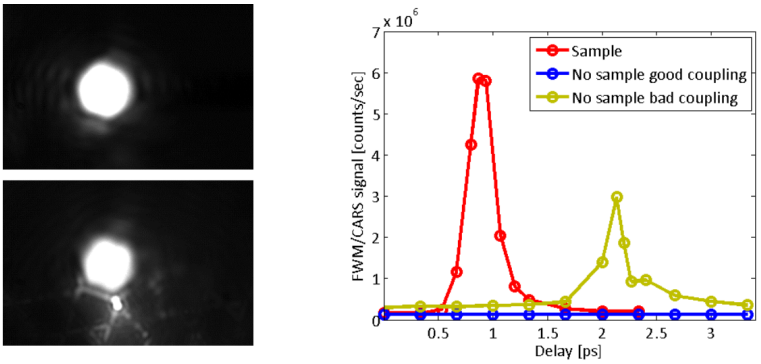

Figure 3.11: (a) Image on the camera of the distal end of the fiber, in conditions of optimal coupling (top) and bad coupling (bottom). When the beams are not optimally coupled, a portion of the beams is incident on the photonic structure surrounding the core, which generates FWM signal, as shown in the graph in (b).

The forward-detected FWM signal generated in the fiber is shown in the graph of Fig. 3.11b. The yellow curve represents the signal generated in bad coupling conditions, which appear as a strong peak with magnitude comparable to the signal from olive oil.

This experiment shows that the fiber can generate FWM background, whenever the fields (or a portion of them) are incident on the silica micro-structure. For this reason, attention must be payed to the beam coupling, when performing CARS imaging with the Kagomé fiber. Beside the power losses caused by the imperfect coupling, a strong background is generated by the silica structure.

3.6 Conclusions

This chapter was dedicated to the problem of ultrashort pulse delivery in nonlinear endoscopy. We first introduced the different type of existing optical fibers (Sec. 3.1). Their use in nonlinear endoscopy was studied in Sec. 3.2. Here, we discussed the problems of both femtosecond pulse distortion and FWM generation, that occur in most types of fibers. This introduced the innovation of our work: the use of a Kagomé hollow-core fiber for the delivery of excitation pulses. Section 3.3 was dedicated to the optical properties of the fiber, such as the transmission band and the GVD curve. The Kagomé allows pulse delivery over a broad wavelength range ($700\ \mathrm{nm}$ to 1100 nm), with no pre-compensation required. In Sec. 3.4, we have shown that the fiber delivery effects, both on the duration and the spectrum of femtosecond pulses, are minimal. Moreover, no FWM background is generated, when the pump and Stokes beams are properly coupled in the fiber (Sec. 3.5). This is very important for CARS endoscopy applications, where no background suppression scheme will be necessary. In the next chapter we will present the development of a miniature imaging device, based on a Kagomé DC fiber for pulse delivery and signal collection.

Chapter 4

Development of a fiber-scanning imaging device

In this chapter, we present the technical development of a miniature imaging device, based on the Kagomé fiber introduced in Ch. 3. In Sec. 4.1, we discuss the requirements for the development of the endoscope probe, and explain our choice of scanning mechanism. This is described in detail in Sec. 4.2, where the mechanical behavior of the scan system is also analyzed. We discuss here the implementation of a suitable imaging pattern, together with the corrections required by the deviations of the real system from the ideal one. In Sec. 4.3, we describe the electronic and software components used to control the scanner and perform imaging. In Sec. 4.4, we highlight two key additional features related to the Kagomé fiber, that are vital for NL endoscopy: the first one is the addition of a cladding in the fiber design, to increase the collection surface and NA. The second one is the insertion of a silica micro-bead on the fiber core, to increase the NA of the fiber delivered beams. In Sec. 4.5 we describe the miniature optical system designed for achromatic beam focusing and signal collection with the probe.

4.1 System Requirements

At the beginning of Sec. 1.2, we have outlined different optical and mechanical requirements for the design of a nonlinear endoscope probe. As a reminder, a nonlinear endoscope should be a miniature (few millimeters in diameter), light, portable and fast imaging device, capable of performing NLOM in remote locations and in-vivo conditions. It has to efficiently deliver excitation pulses and collect the generated nonlinear signal, using optical fibers. Moreover, a nonlinear endoscope needs to incorporate a scanning mechanism, in order to perform imaging on the sample.

We will describe here our implementation based on a piezo tube that scans a Kagomé double

clad (DC) fiber. When operated at resonance conditions, these scanners can achieve significantly large FOV ($> 400\,\mu m$) with low driving voltages (30 V) and high frame rates (<1 fps[1]). The overall diameter of these systems can reach dimensions as small as 2 mm. The Kagomé fiber allows undistorted pulse delivery and background-free multimodal imaging with high spectral tunability, with no need for pre-compensation mechanisms or filtering of the FWM background. Before starting the description of the system, we will now briefly describe the general features of fiber scanning endoscopes based on tubular piezo actuators.

4.1.1 Piezo-tube based fiber scanners

Piezo-tube fiber scanners [124] are widely used in nonlinear endoscopy, because they constitute a robust and inexpensive solution, that is relatively easy to assemble and align as compared to MEMS mirrors. Many examples of systems employing this technology can be found in literature [32, 84, 150, 151]. Figure 4.1 shows the basic principle of a fiber scanning endoscope. The

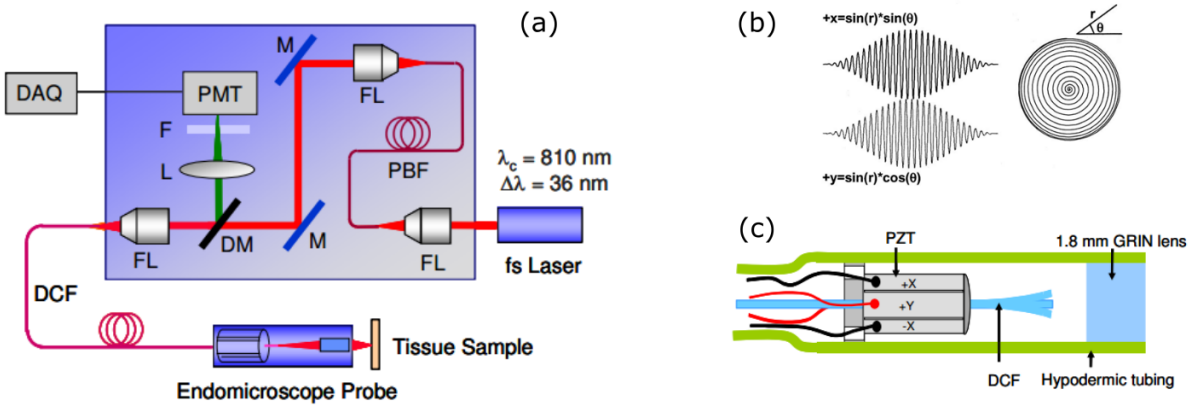

Figure 4.1: Principles of a fiber scanning endoscope based on a four quartered piezo tube. (a) The laser pulses are coupled into the endoscope fiber. The fiber is attached to the piezo tube in the endoscope probe. (b) When driving the piezo tube with appropriate waveforms (oscillating at the resonant frequency of the fiber) one can produce a symmetric scan pattern. (c) A miniature optical element re-image the fiber tip on on the sample, reproducing the scan pattern. The signal generated at the sample is then back-collected by the fiber and sent to the detectors. Images taken from [147] and [105].

fiber is attached to the piezo tube and delivers the excitation laser beams. A miniaturized lens assembly (or a GRIN[2] lens) is used to image the fiber core on the sample plane. While the fiber is moved in a controlled pattern with the piezo tube, the spot is scanned over the sample plane. The nonlinear signal, excited by the scanning laser beams, are back-collected through the same fiber and detected on the proximal end.

The FOV of the endoscope depends on the optical system, through the magnification factor that scales the fiber scan amplitude. The same holds for the resolution, which depends on the

[1]Frames per second.
[2]Gradient-index

beam size on the sample. Single mode fibers typically have core sizes on the order of few micrometers. In order to reach the spatial resolution of standard NL microscopes, demagnification from the fiber to the sample is required. Zhao et al. reported a 150 μm FOV with 1.5 μm lateral resolution, which came from a focusing optics with magnification M=0.43 [151]. Zhang et al. used a miniature achromatic lens with M=0.22 and achieved FOV of 110 μm, with relatively high driving voltages (50 V to 110 V, depending on the probe) [150]. Ducourthial et al. achieved a FOV of $400\,\mu$m with a magnification M=0.48 and a lateral resolution of 0.83 μm, using 30 V driving voltages.

The reported dimensions for this type of probes have reached a diameter of 2 mm, which can easily fit in the working channel of standard forward viewing endoscopes. The main limitation to the miniaturization comes from the size of the piezo tube and/or the optical elements, where excessive size reduction is accompanied by poor imaging properties.

4.2 The scanning mechanism

The scanning fiber attached to the piezo-tube is similar to a free standing cantilever. It behaves like a driven harmonic oscillator, when external waveforms are applied to the piezo-tube. For low voltages (30 V), the piezo-tube generate a displacement of about a few micrometers only. However, the free standing fiber can oscillate hundreds of micrometers when driven at the mechanical resonance frequency. Therefore, in order to obtain a 2D scan, both the axes have to be driven simultaneously near their resonance. Since the resonant frequency is approximately the same on both axes, the raster scan pattern typically used in microscopy cannot be employed here. In order to obtain a large and symmetric FOV, the mechanical features of the fiber scanner, such as the resonant frequency on the two axes or the phase response, have to be fully known and characterized. In this section we shall discuss all the aspects related to the fiber scanner. These include the piezo-electric tube, the mechanical behavior of the free-standing fiber and the waveform parameters to excite the fiber into an optimal imaging pattern.

4.2.1 The piezo-electric tube

Piezo-electric tubes exist in a variety of sizes and specifications, depending on the applications they are meant for. In this work we used the PT230.94, that can be found in the catalogue of Physik Instrumente (PI). It is a 30 mm long hollow ceramic tube, with an outer diameter (OD) of 3.2 mm and an inner diameter (ID) of 2.2 mm. It is made of the ceramic type PIC255, a piezo-electric material based on modified Lead Zirconate Titanate (PZT). The outer surface of the tube is divided in four isolated electrodes, which provide displacement in the two lateral directions (Fig. 4.2). A fifth electrode in the inner surface can serve as ground.

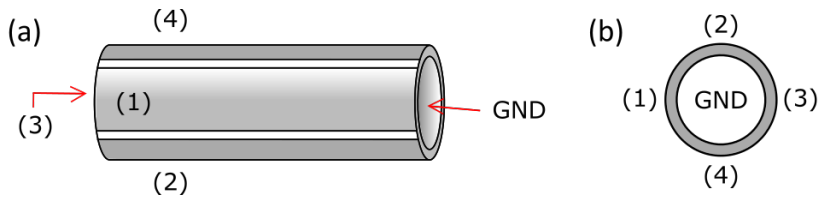

Figure 4.2: (a) Lateral view and (b) cross section of a four-quartered piezo tube. The numbers refer to the each one of the four isolated electrodes of the tube, plus the inner electrode which serves as ground.

In order to maximize the piezo deflection, we can apply opposite waveforms to the opposite electrodes. For instance, the waveforms $V_{\mathrm{x}}(\mathrm{t})$ and $-V_{\mathrm{x}}(\mathrm{t})$ are applied to electrodes 1 and 3 of the piezo tube in Fig. 4.2. Two other waveforms $V_{\mathrm{y}}(\mathrm{t})$ and $-V_{\mathrm{y}}(\mathrm{t})$ are then applied to electrodes 2 and 4. In general, when a voltage is applied to a piezo-electric material, this tends to compress or dilate depending on the sign of the voltage. In piezo tubes, this results in a bending in one lateral direction (Fig. 4.3). One can calculate the displacement along the x direction of the piezo

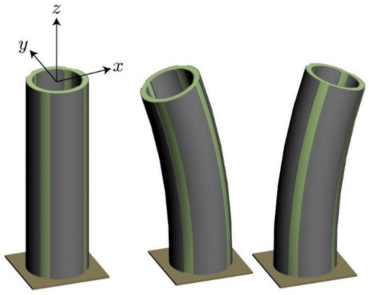

Figure 4.3: Deflection of a four-quartered piezo tube as tension is applied on its electrodes (taken from www.piezodrive.com).

tube, in response to an applied voltage V_{x}:

$$\Delta x(t) = V_x \frac{2\sqrt{2} d_{31} L^2}{\pi D h} \tag{4.1}$$

Where $\Delta x(t)$ is the deflection on the x-axis, d_{31} is the piezo-electric strain constant ($d_{31} = 180$ pC/N for the PIC255 ceramic), L the length of the tube (30 mm), D is the outside diameter (3.2 mm), h the tube thickness (1 mm). Using equation (4.1) one can find that if an external static voltage $V_{\mathrm{x}} = 30\,\mathrm{V}$ is applied, the piezo tube will experience a $1.2\,\mu\mathrm{m}$ deflection. In order to achieve sufficiently large FOVs, one has to drive the piezo at the resonant frequency of the free-standing fiber. This can be calculated, as we will see in the next section (Eq. (4.2)).

4.2.2 Fiber spiral scanning

The scan pattern typically used in nonlinear microscopes is the raster scan (Fig. 4.4a). The beam focused on the sample moves at high speed on one axis and slowly on the other one:

this produces a line scan that is multiply repeated over the sample, leading to a square FOV. In the case of resonant fiber scanning, such a pattern cannot be used, since driving out of resonance would result in very small displacements. When driving the two axes at resonance, one can perform either the so-called Lissajous pattern or a spiral pattern. The Lissajous pattern is characterized by an oversampling on the periphery of the image, which is usually not the most interesting part of the FOV. Moreover, it requires different resonant frequencies on the two axes [31]. If the two resonances are very close to the same value f_{RES}, which is usually the case for tubular actuators, one can use a spiral pattern (Fig. 4.4), which is obtained when a circular motion is slowly modulated in amplitude.
One feature of resonant scanners is that the acquisition speed (or pixel dwell time) is defined by the characteristic frequency and cannot be set arbitrarily. This leads to a series of constraints on the scan parameters, in order to obtain a correct sampling of the FOV. In fact, the distance between adjacent circles of the spiral should be as small as the PSF ($\approx 1\,\mu\mathrm{m}$). Furthermore, this distance should be smaller than the pixel size, to ensure that all the pixels in the image are sampled during the scan.

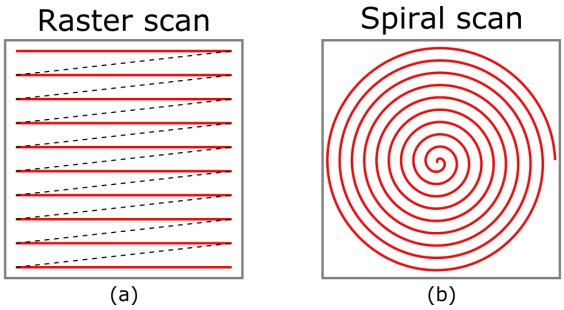

Figure 4.4: (a) Raster pattern typically used in scanning microscopy, where only one axis can be at resonance. (b) Spiral pattern, which can be obtained when the two axes are driven at the same frequency.

Free-standing cantilever

In an initial prototype, we attached the scanning fiber to the piezo tube using a 3D-printed element, where a hole of diameter 0.5 mm was drilled to let the fiber through, and some glue applied to fix the fiber. The free standing part of the fiber behaves as driven harmonic oscillator, when external waveforms are applied to the piezo tube (Fig. 4.5). When a sinusoidal waveform

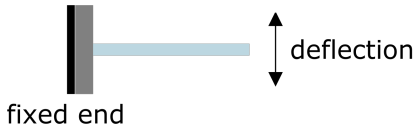

Figure 4.5: When the piezo tube's electrodes are given a voltage, the fiber behaves as a driven harmonic oscillator.

is applied to the piezo tube, the fiber oscillates with the same frequency. However, the amplitude of the displacement is not frequency independent, but shows a well defined Lorentzian peak (like the ones in Fig. 4.6). The resonant frequency of the fiber corresponds to the point of maximum displacement in response to an applied waveform. It depends on the free-standing length L and can be theoretically estimated using equation:

$$f_{RES} = \frac{\beta}{4\pi L^2}\sqrt{\frac{ER^2}{\rho}} \tag{4.2}$$

where β is a constant that depends on the order of the resonance, E is the Young modulus of silica, R is the fiber radius and ρ the volumetric mass density of the fiber. In our probe based on a Kagomé double clad (DC) fiber, a free-standing length of 23 mm results in a resonant frequency around 550 Hz. Ducourthial et al. [31] measured the resonant frequency for a standard single mode fiber of diameter 125 μm. In that case, a free-standing length of 23 mm gives a resonant frequency $f_{\mathrm{RES}} \approx 200\,\mathrm{Hz}$. The difference, with our fiber, might be due to both the bigger fiber radius R and the higher air fraction in the Kagomé, which reduces the density ρ.

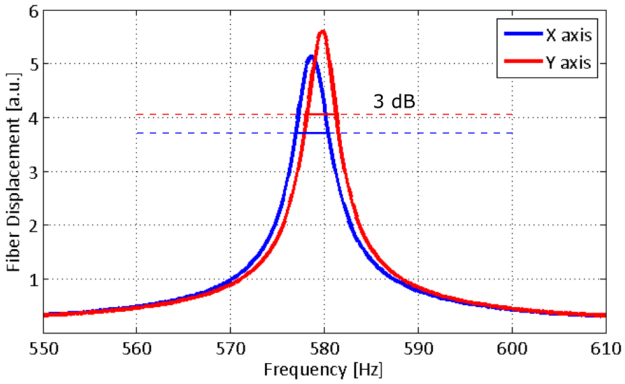

Figure 4.6: Measured spectrum of the two axes for our fiber resonator. From the resonant frequency and the width of each curve, calculated at an attenuation value of 3dB, one can measure the quality factor of the resonator (Eq. 4.3).

The measured scan amplitude of the Kagomé DC fiber in the two lateral direction, as a function of the driving frequency, is shown in Fig. 4.6. We can see that the mechanical system is not perfectly symmetric: the resonant frequencies of the two axes differ by 1 Hz.
The quality of a driven oscillator is often measured in terms of the quality factor Q. This is defined as:

$$Q = \frac{f_{\mathrm{RES}}}{\Delta f_{\mathrm{RES}}} \tag{4.3}$$

where Δf_{RES} is the full width of the resonance curve, defined at an attenuation value of 3 dB (which corresponds to a factor $\sqrt{2}$). For the spectra of Fig. 4.6, measured using a position sensitive detector with a 0.2 Hz spacing between the waveforms, Δf_{RES} is approximately 3.1

Hz on the y-axis (red curve) and 3.6 Hz on the x-axis (blue curve). This leads to a quality factor Q of approximately 186 and 159, respectively. This is a good value for such a scanner, when compared to values found in literature (Q=110 in [77], Q=200 in [32]).

Driving waveforms

In the definition of the waveforms, we first consider the ideal case of a perfectly symmetric system, so that the response of the oscillating fiber to a voltage $V(t)$ is the same on both axes. This is not exactly the case for real systems, where some corrections on the waveforms are necessary to obtain a circular FOV. We will describe these corrections in the next section.
In the ideal case, a circular pattern is obtained when the two axes are driven with a sinusoidal waveform oscillating at the same frequency f_{RES} and $\pi/2$ phase difference. In order to obtain an expanding spiral pattern, an amplitude modulation has to be imposed on the waveforms (Fig. 4.7). A functional form for the voltages passed to the piezo tube electrodes can be:

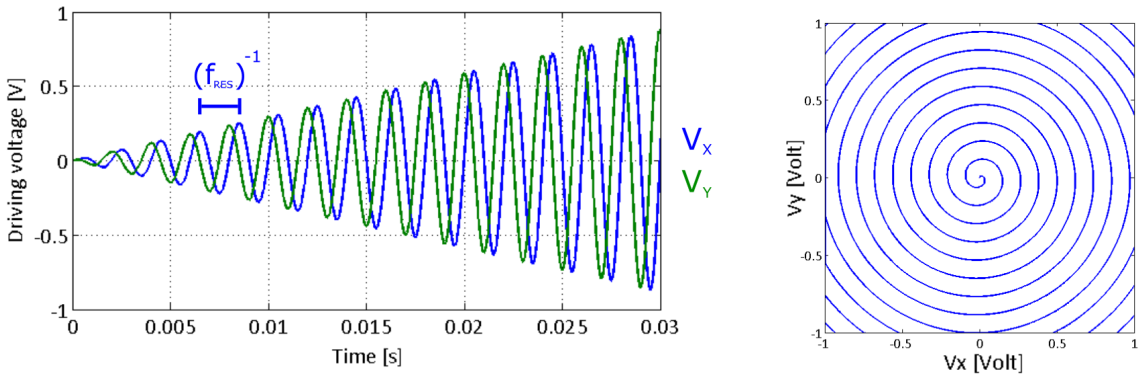

Figure 4.7: Example of the waveforms used to produce a spiral pattern in the ideal case of a perfectly symmetric system. The resonant frequency ($f_{\mathrm{RES}} = 500$ Hz) is the same for both axes, that are driven with a $\pi/2$ phase difference. The intensity modulation results in an expanding spiral pattern.

$$V_{\mathrm{x}}(t) = V_{\mathrm{max}} \cdot sin(2\pi f_{\mathrm{mod}} t) \cdot sin(2\pi f_{\mathrm{RES}} t) \tag{4.4}$$

$$V_{\mathrm{y}}(t) = V_{\mathrm{max}} \cdot sin(2\pi f_{\mathrm{mod}} t) \cdot cos(2\pi f_{\mathrm{RES}} t) \tag{4.5}$$

Where V_{max} is the maximum voltage that can be delivered, $f_{\mathrm{mod}} << f_{\mathrm{RES}}$ is the frequency of the slowly varying modulation envelope. These waveforms drive the actuator for a time:

$$t \leq T_{\mathrm{exp}} = \frac{1}{4 f_{\mathrm{mod}}} \tag{4.6}$$

Where T_{exp} is the duration of the expanding part of the scan (Fig. 4.8, red arrow). Then different types of drive are possible. In literature it is quite common to find a retrace period, usually shorter than the expansion, during which the same sinusoidal oscillations are subject

to a decreasing intensity modulation, or literally a phase inversion for active breaking (green arrow). This is usually followed by a rest period (orange arrow), with the piezo position set to zero while the fiber oscillations naturally fade [35, 105].

If no active breaking is applied, the rest period is very important, since the fiber continues the

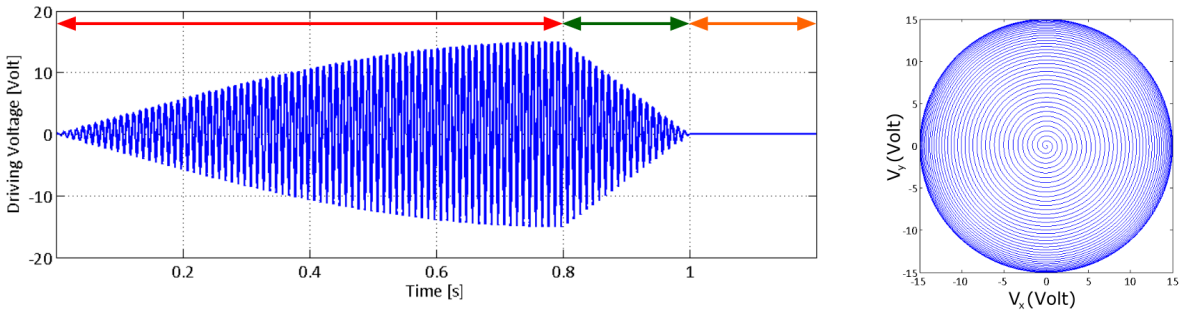

Figure 4.8: Example of a 100 Hz oscillating waveform with sinusoidal expanding modulation for 0.8 s, linear retrace for 0.2 s and zero voltage for 0.2 s.

oscillations after an expansion period, even if the piezo voltage is set to zero (it behaves like a damped oscillator). The duration of this free-decay period is proportional to the quality factor, and can be on the order of hundreds of milliseconds [31]. It is necessary to wait the end of the oscillations, otherwise image distortions will appear if a new scan pattern is started while the fiber is still moving. In order to optimize the imaging frame rate of the device, one should impose a breaking period. This can be done by changing the phase of the driving waveforms, which turns the piezo into a damping element. With a precise identification of the phase and duration of the breaking cycles, one can stop the fiber's oscillations in few cycles [31, 78].

4.2.3 Corrections for symmetric patterns

As previously mentioned, the real pattern followed by the fiber scanner is different than the waveforms (shown in Figs. 4.7 and 4.8). First of all, the response of the fiber to the driving force is not instantaneous. When a linear modulation ramp is applied, the fiber has a first transitory regime where the oscillations do not follow the modulation curve. The duration of this regime is approximately Q/f_{RES} [31], so on the order of hundreds milliseconds for our resonator. This can lead to distortions at the center of the image, if the image reconstruction is done assuming that the fiber follows instantaneously the driving waveforms. These distortions are avoided when using a Position Sensitive Detector (PSD) to trace the position of the spot during a scan. However, the oversampling at the center of the image due to the transitory regime cannot be avoided.

Correction to real axis

The second effect is the so-called whirling of the resonator. It is due to a cross-coupling effect between the axes of the resonator, and happens when driving one single electrode at the resonant frequency or very close-by. Here the fiber stops following the expected line pattern and turns into an ellipse. This is shown in Fig. 4.9, where the image of the fiber scan is acquired for different driving frequencies, including the resonant frequency. Whirling of the fiber is an

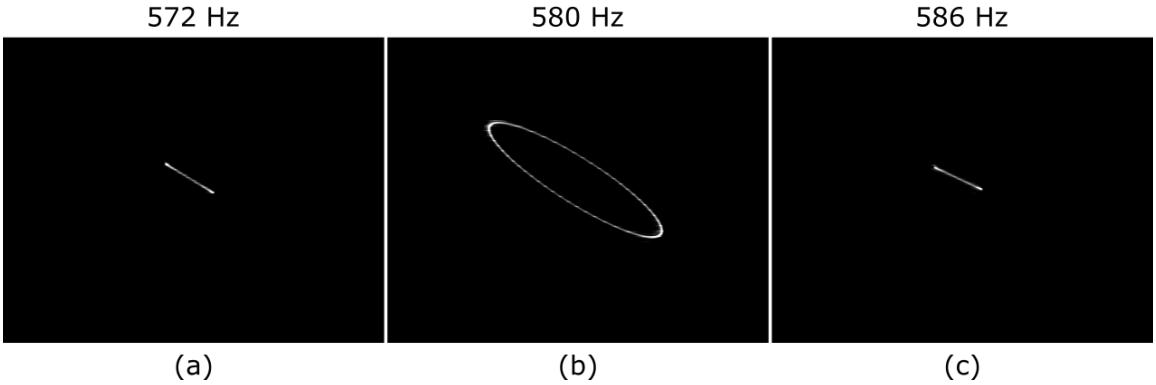

Figure 4.9: Scan pattern obtained when driving one individual electrode. Before and after the resonance, the fiber follows a line pattern (a) and (c). At resonance the fiber scan results in an elliptic trajectory, an effect called whirling (c).

undesirable effect that has to be eliminated in order to properly control the scan pattern. In fact, when the individual electrodes generate a motion on both axes, a destructive interference between the two motions can reduce the scan amplitude. A solution to the problem of whirling was first introduced by the group of E. J. Seibel [78], but can be found developed in great detail in the thesis of Guillaume Ducourthial (2014, Université de Limoges, France [31]).
The idea is that the mechanical resonator (i.e.: the fiber) can be excited along two orthogonal axes which are not coupled one to another. These are the eigen directions of the resonator and they are different than the axes of the electrodes. One has to drive the fiber motion along this directions, in order to remove the coupling between the axes. This requires the simultaneous excitation of both real electrodes (of the piezo). In fact, one can apply the transformation:

$$\hat{e}\mathrm{X} = cos(\theta)\hat{e_{\mathrm{x}}} + sin(\theta)\hat{e_{\mathrm{y}}} \tag{4.7}$$

$$\hat{e}_{\mathrm{Y}} = -sin(\theta)\hat{e_{\mathrm{x}}} + cos(\theta)\hat{e_{\mathrm{y}}} \tag{4.8}$$

which corresponds to a rotation of an angle θ on the plane of the reference system, with the new orthonormal vectors $\hat{e}_{\mathrm{X}}$ and $\hat{e}_{\mathrm{Y}}$. For a certain θ, these correspond to the eigen directions of the mechanical system and define what are called the virtual electrodes (Fig. 4.10). We refer to (V_{X},V_{Y}) for an excitation on the virtual electrodes and to (V_{x},V_{y}) for the real electrodes. Then,

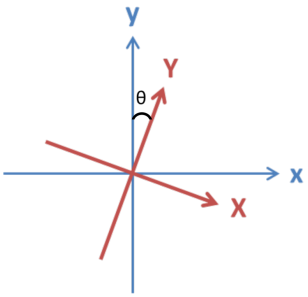

Figure 4.10: The axes of the resonator (red) do not coincide with the axes of the piezo electrodes (blue).

in order to drive only one virtual electrode (to obtain a line pattern):

$$V_{\mathrm{X}}(t) = cos(\omega t) \tag{4.9}$$

$$V_{\mathrm{Y}}(t) = 0 \tag{4.10}$$

one needs to drive the real electrodes with the waveforms:

$$V_{\mathrm{x}}(t) = cos(\omega t)cos(\theta) \tag{4.11}$$

$$V_{\mathrm{y}}(t) = cos(\omega t)sin(\theta) \tag{4.12}$$

An iterative procedure can then be followed in order to find the correct value of θ. In this case, the excitation is on the virtual electrodes and the fiber follows a line scan at resonance, as shown in figure 4.11. The same transformation can be applied on the other axis, using the same

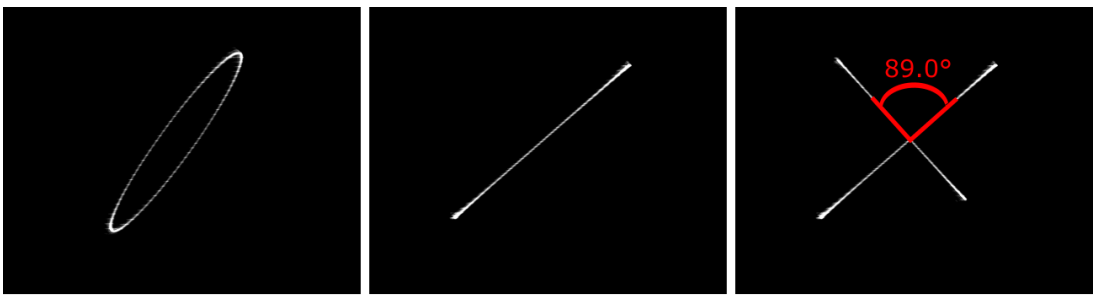

Figure 4.11: Removal of the whirling effect when using the virtual electrodes for excitation. (a) The scan pattern obtained when driving one single electrode of the piezo-tube near the mechanical resonance of the fiber. (b) The whirling effect is removed when driving the piezo along the virtual electrodes. (c) Superposed image of the scan patterns obtained when driving individually the virtual electrodes. The angle between the two directions is measured as 89°.

rotation angle θ, which removes the whirling effect on this direction. Two line patterns can be obtained at resonance, and they make an angle 89° one with respect to the other (Fig. 4.11c).

This correction allows to control the driving of the fiber in an optimal way, so that the whirling motion does not result in scan amplitude losses.

Phase control

One last correction is necessary because of the different resonant frequency of the two axes. In fact, harmonic oscillators have a characteristic phase response to the driving waveform. Before the resonance, the oscillator is in phase with the driver, but experiences a phase lag of 90° at the resonant frequency, which becomes 180° after the resonance. In Fig. 4.12 the simulated response of two harmonic oscillators is shown. The oscillators have a difference of 1 Hz between

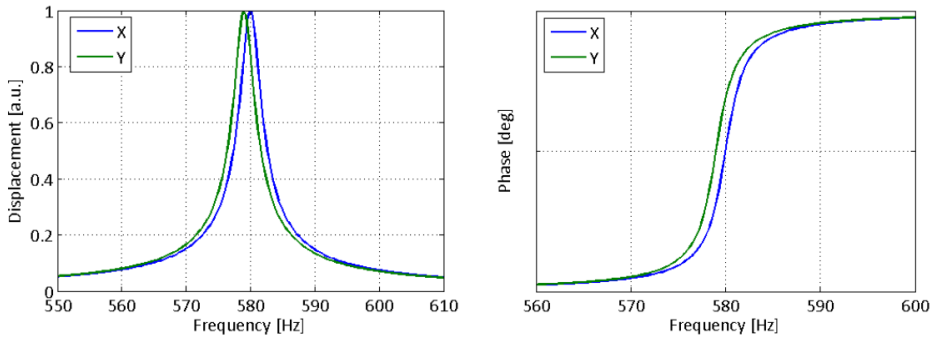

Figure 4.12: Numerically computed frequency response of a driven harmonic oscillator, in amplitude and phase. The oscillator experiences a π phase shift before and after resonance, with respect to the driving waveform.

their resonant frequencies, which is similar to the real case of our piezo tube (Fig. 4.6). From the phase graph (Fig. 4.12, right-hand side) it is clear that if we drive the fiber with a frequency in-between the two resonances, a phase adjustement has to be made. In fact, the 90° difference between the waveforms (Fig. 4.7) is not preserved by the resonator, which results in an elliptical pattern instead of a circular one.
We can correct this difference by adding a phase on one of the axis:

$$V_{\mathrm{X}}(t) = cos(\omega t) \tag{4.13}$$

$$V_{\mathrm{Y}}(t) = sin(\omega t + \Phi) \tag{4.14}$$

The right value of Φ is the one that produces a line scan whenever $V_{\mathrm{X}}(t) = cos(\omega t)$ and $V_{\mathrm{Y}}(t) = sin(\omega t + \Phi + \pi/2)$.

To summarize, when a new scanner is used, we need to identify the resonant frequencies at first. Then we identify the correct value of θ that defines the orthogoanl driving axes, and generate the appropriate corrections to the driving voltages. In the case of different resonant frequencies, the scan frequency is set to a value in-between the resonances, another iterative

procedure is used to find the right phase correction Φ. Finally a slight adjustment of the waveforms amplitudes is done to obtain a circular pattern. This concludes the waveform corrections

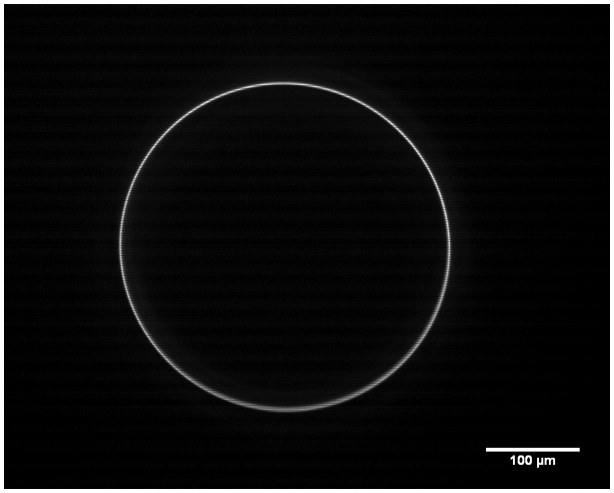

Figure 4.13: Final scan pattern obtained after all the corrections performed on the excitation waveforms.

that are required to efficiently control the fiber scanner in two dimensions at resonance. This part of the calibration phase identifies the parameters to generate the voltage waveforms, that drive the piezo-tube to perform scanning in an symmetric manner. In the following section, we shall see how these waveforms translates to spatial position and to finally image coordinates.

4.3 Imaging software and hardware

Performing imaging with a fiber scanner has distinct phases:

- Driving of the scanner and acquisition of the generated signal by a detector.
- Mapping the driving voltages to spatial positions of the beam on the sample (by means of a position measurement).
- Assigning the detected signals to the image co-ordinates and build the image.

It is important that one knows *a priori* the pattern followed by the fiber in response to the driving waveforms. In fact, this information is crucial for the reconstruction of the images.
In this section we will describe the hardware and software components that control the scanner. Then we will examine the details of the image reconstruction algorithm. We will see how images are built from the detected signal and the measured scan pattern of the fiber.

4.3.1 Imaging procedure

The general flow of the imaging algorithm is shown in Fig. 4.14. The scan parameters, such as amplitudes, frequencies, phase and virtual electrode's angle, are used to create two waveforms $V_{\mathrm{x}}(t)$ and $V_{\mathrm{y}}(t)$. These drive the fiber in a scan pattern, which can be measured with a Position Sensitive Detector (PSD) that gives two positions lists. At the same time, one can measure the signal generated on the sample during the scan to obtain an intensity vector. Then, an image can be reconstructed from the intensity values and the positions list, in the way that will be described later. These two measurements (positions and signal) can be performed at the same time (*closed-loop*). However, an endoscope probe requires a position measurement that stays valid in time. The information on the spot position is used to build all successive images, assuming the scan pattern does not change (*open-loop*).
In the open-loop configuration, the upper and lower parts of the chart (Fig. 4.14) do not need to work in parallel. The system is stable during one day, but a small drift in the fiber response to the same waveforms is observed after 24 hours. A daily calibration is then recommended to avoid small distortions in the images.

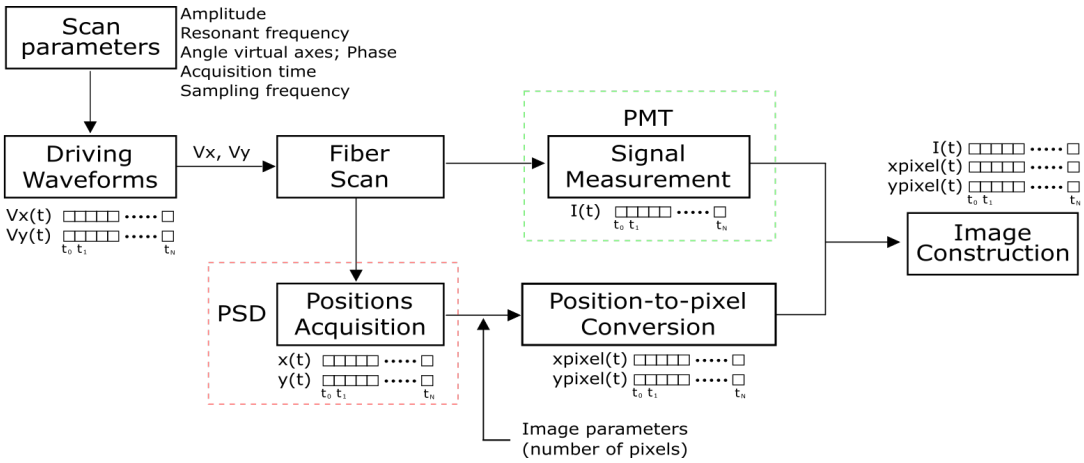

Figure 4.14: Flow chart of the imaging algorithm: two waveforms are generated from a set of parameters. They drive the fiber into a motion, that can be detected with a PSD. From the measured positions one can map the instantaneous position of the beam during the scan. This information is used to build the images, by assigning each intensity value to a specific pixel in the image. The upper and lower part of the chart do not need to work in parallel.

4.3.2 Data acquisition device

The processes of scan driving and signal acquisition need to be synchronized: to perform simultaneously the tasks we use a National Instrument USB acquisition card (NI-USB6351). This board has 2 Analog Output (AO) channels, used to drive the piezo tube, delivering voltages from -10 V to +10 V at a maximum rate 2.86 Msamples/s. The waveforms V_{x} and V_{y} from the

AO channels are used to control the scan, driving two of the four electrodes (say 1 and 2 of Fig. 4.2), while the other two are grounded.
The USB card has 16 analog inputs to perform data acquisition. The maximum sampling rate is 1.25 Msamples/s when using a single channel. When using multiple channels (with the PSD, for instance) this value is divided by the number of channels. The maximum sampling rate for position acquisitions (3 channels) is then ≈415 kHz. The analog input channels are also used with analog PMTs and photodiodes. 24 digital lines allow acquisition from detectors such as avalanche photodiodes (APDs) and photon-counting PMTs, whose output is a TTL signal whenever a detection event has occured.

4.3.3 Imaging software

The NI board is controlled by a custom made LabView software, that was developed during this thesis. The software is used to perform two main tasks: calibration of the scan patterns and image acquisition and reconstruction. The software is based on a synchronization of the output tasks (voltage delivery) and input tasks (signal acquisition, positions detection). It was built on the ground of an existing LabView software for the control of multimodal microscopes, which was developed by Patrick Ferrand (Institut Fresnel) [38].
We have developed a software with two main tasks, one for scan pattern calibrations and one for imaging. The software is based on a synchronization of the output tasks (voltage delivery) and input tasks (signal acquisition, positions detection). The synchronization is ensured by an analog trigger delivered by the board itself, that starts all the tasks at the same moment. One of the tasks consists in the periodic pixel clock, that defines the *sampling rate* at which the board performs any task. In the case of analog inputs, the acquisition of the voltage is a one-time measurement of the signal, that happens with the frequency of the pixel clock. Working at the highest sampling rate improves the signal to noise (SNR) ratio in an analog measurement. Digital channels work like open gates that store the number of TTL pulses delivered (photons detected) by the detector. Therefore the SNR does not depend on the sampling rate, but it's important to have a high readout frequency, in order to avoid that photons emitted at one pixel are assigned to another one (remember that the pixel dwell time is imposed by the resonant frequency of the scanner).

The software reads the input scan parameters, defined by the user, and builds two waveforms that are delivered by the AO channels to two broadband amplifiers (WA301, Thurlby Thandar Instruments). The amplifiers are sufficiently fast (bandwidth upper limit 1 MHz) and increase the waveforms amplitude to 30 V peak-to-peak. When all the channels are ready, LabView starts the tasks, driving the scan and acquiring the signal. The intensity and count measurements are stored in vectors that are read at the end of the execution. The process is then repeated until the user stops it.

Positions aquisition The calibration of the scan pattern can be done using a PSD (PDP90A, Thorlabs), which measures the instantaneous position of the laser beam on the sensor. We focus the beam exiting the fiber on the PSD, which has an effective sensitive area of 9x9 mm^2. This device measures the displacement of the beam relative to the center of the detector. The output from the PSD consists of three analog signals, that we call Δx, Δy and Σ. In order to avoid saturation of the detector, that would result in position measurement errors, we adjust the beam intensity so that the Σ voltage is less than 4 V (Fig. 4.15). From these three signals, we retrieve the position of the beam on the detector using the equations:

$$x = \frac{L_x \cdot \Delta x}{2 \cdot \Sigma} \quad , \quad y = \frac{L_y \cdot \Delta y}{2 \cdot \Sigma} \tag{4.15}$$

Where x and y are the beam positions on the detector, L_x and L_y the size of the detector (9 mm). The first step consists in a measurement of the scan trajectory performed by the fiber

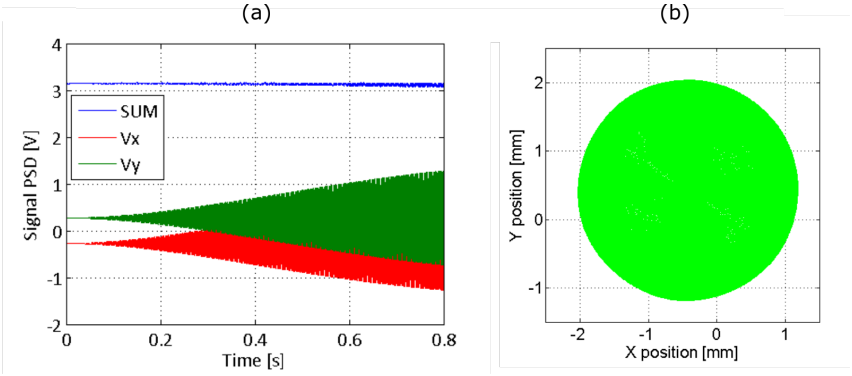

Figure 4.15: (a) The voltage traces given by the PSD are proportional to the x-position (red curve) and y-position (green curve) on the detector. The Σ signal (blue curve) is proportional to the total intensity incident on the detector, and is used to normalize the x and y signals (Eq. 4.15). This gives the positions of beam on the detector (shown in the x-y plane in (b)).

under a certain waveform. A calibration procedure is followed to identify the scan parameters that produce a circular scan pattern with the maximum amplitude. Using the waveforms based on these parameters, we make a measurement of the instantaneous position of the beam during the scan. The maximum sampling rate for three simultaneous analog detection is 250 kHz, one every 4 µs. A linear displacement of the spot between two measured positions is assumed when imaging at faster rates (1 MHz sampling). This allows to interpolate the measured positions, and generate position vectors with a finer spatial sampling (and a temporal sampling equal to the intensity measurement).

Image reconstruction After a scan cycle is performed and the corresponding signal acquired, one can reconstruct the image based on the positions. The definition of the number of pixels in the image is arbitrary and can be done *a posteriori* by the user. For the same acquisition one can

build a 100x100 image and a 300x300 image. When we perform imaging, the same scan pattern that was measured with the PSD is reproduced, as long as the same waveforms are used to drive the fiber motion. As we move the excitation spot over the sample, we detect the generated nonlinear signal, either with an analog detector or a digital one, and send it to the NI board. The detection is synchronized to the scan waveform, for which the positions were previously measured, so the signal can be assigned to the correct spatial co-ordinates in post processing. At the first execution, as the user specifies the number of desired pixels in the image, the software builds two vectors containing the pixel coordinates, using the information on the spot position.

These two vectors have the same length as the time vector and the intensity vectors. At

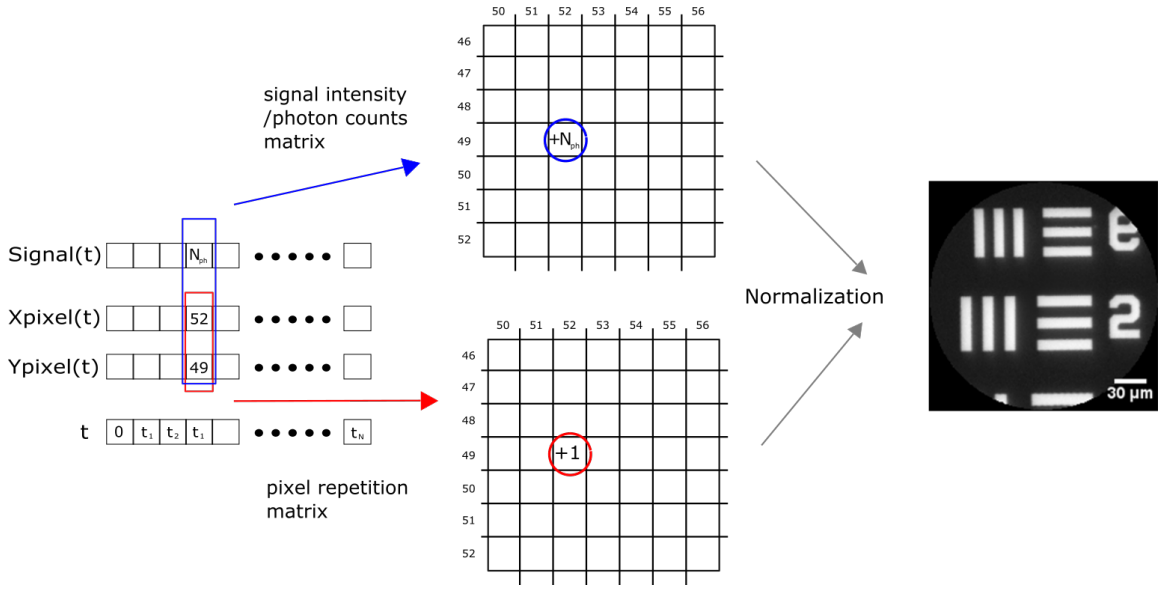

Figure 4.16: Reconstruction of an image: the positions measured with the PSD (Fig. 4.15) are converted into pixel coordinates. Then, the intensity measurements performed during the scan are assigned to the corresponding pixel coordinates. Finally, the intensity of each pixel is normalized by the number of samplings for that pixel.

the read out, the elements in the intensity vector I(t) (which contains either the analog signal or the number of photons) are assigned to the corresponding pixel of the image, using the pixel coordinate lists (Fig. 4.16). We build two matrices: the first one contains the measured intensity values. However, the number of intensity measurements per pixel is not uniform across the image, because of scanning constraints. For this reason we build a second matrix, which contains the number of measurements that have been done for each pixel (sampling). When the vectors read-out is completed, the values in the intensity matrix are normalized, using the pixel sampling matrix. The resulting matrix corresponds to the image of the sample as acquired by the fiber-scanning device.

The performance of the reconstruction algorithm can be verified by imaging a binary USAF-1951 resolution chart (see Sec. 5.2).

4.4 Kagome DC fiber for nonlinear endoscopy

As previously mentioned, the innovation of our work lies in the type of optical fiber employed for the endoscope probe. This Kagomé double-clad (DC) was designed and produced by Alexandre Kudlinski (IRCICA, Lille) for applications in nonlinear endoscopy. The pulse delivery properties of the fiber where described and characterized in Ch. 3. The Kagomé DC combines the broadband and distortion-less pulse delivery of a Kagomé with the increased collection efficiency given by the external clad.

In fact, this fiber was designed with a second annular silica core dedicated to the collection

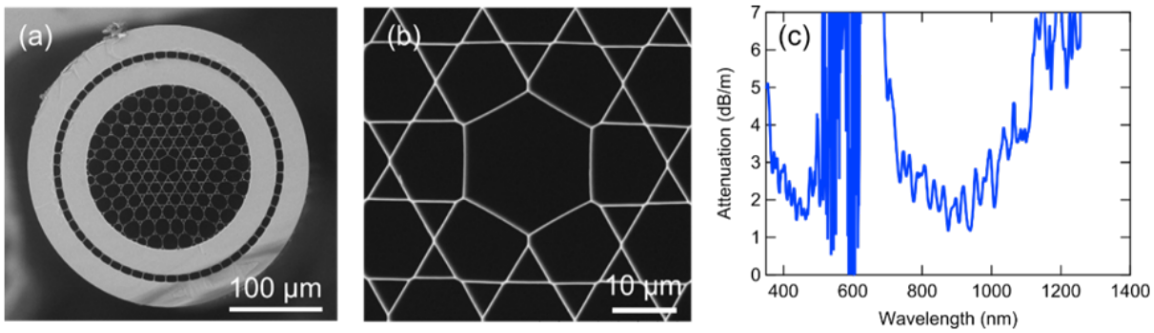

Figure 4.17: (a) SEM micrograph and (b) close-up on the hollow core region of the Kagomé double-clad fiber. (c) Measured attenuation spectrum of the air guided mode.

of nonlinear signals. Multimode guidance in this clad is ensured by the low index ring of air holes (air clad) surrounding the Kagomé structure. The measured NA of this collection clad is 0.5 at 400 nm. The inner and outer diameter of are 179 µm and 250 µm, respectively. This gives an efficient collection surface of $2400\,\mu m^2$. This external clad is necessary to increase the collection efficiency of the fiber, when imaging in scattering media, such as biological tissues. As we will in Sec. 4.4.2, light is coupled into the double-clad when the photons emitted at the focus are scattered back by the tissue. Moreover, transmission losses impair the fiber collection efficiency through the core, in the wavelength range between 450 nm and 650 nm (see Fig. 4.17c). Therefore, the multimode clad allows to collect nonlinear signals from scattering tissues in this spectral region.

4.4.1 Micro-bead focusing

As we mentioned in Sec. 4.1, in fiber-scanning endoscopy there is a close relation between FOV and resolution. These quantities both depends on the focusing optics, on the displacement of the fiber tip and on the fiber's core NA (and mode field diameter). In fact, the sample plane is the optical conjugate of the fiber tip plane. The resolution of the imaging system depends on the size of the beam exciting the sample. A large beam size corresponds to a lower spatial resolution. Moreover, a large focal spot has a lower intensity than a tightly focused one, which

means a lower excitation efficiency. A demagnification from the fiber to the sample is always performed in this type of endoscope. Here, the beam delivered by the Kagomé fiber has a mode field diameter of $\approx 18\,\mu\mathrm{m}$ with a very low NA (0.02). In this case, a 0.1x magnification would lead to an acceptable ($< 2\ \mu\mathrm{m}$) resolution. However the scan pattern would be scaled by the same factor, resulting in FOVs as small as 50 $\mu\mathrm{m}$. We addressed this problem following an original approach developed in our group, based on a transparent micro-bead attached to the fiber core. The micro-bead increases the beam NA, so that the 0.02 NA field exiting the Kagomé core is focused to a small spot ($\approx 1.2\ \mu\mathrm{m}$), a few micrometers after the bead. This removes the need for a strong demagnification from the fiber to the sample. The benefit is clear: a Kagomé with micro-bead can be integrated in a fiber scanner, providing high resolution while retaining the scan amplitude to obtain large FOVs.

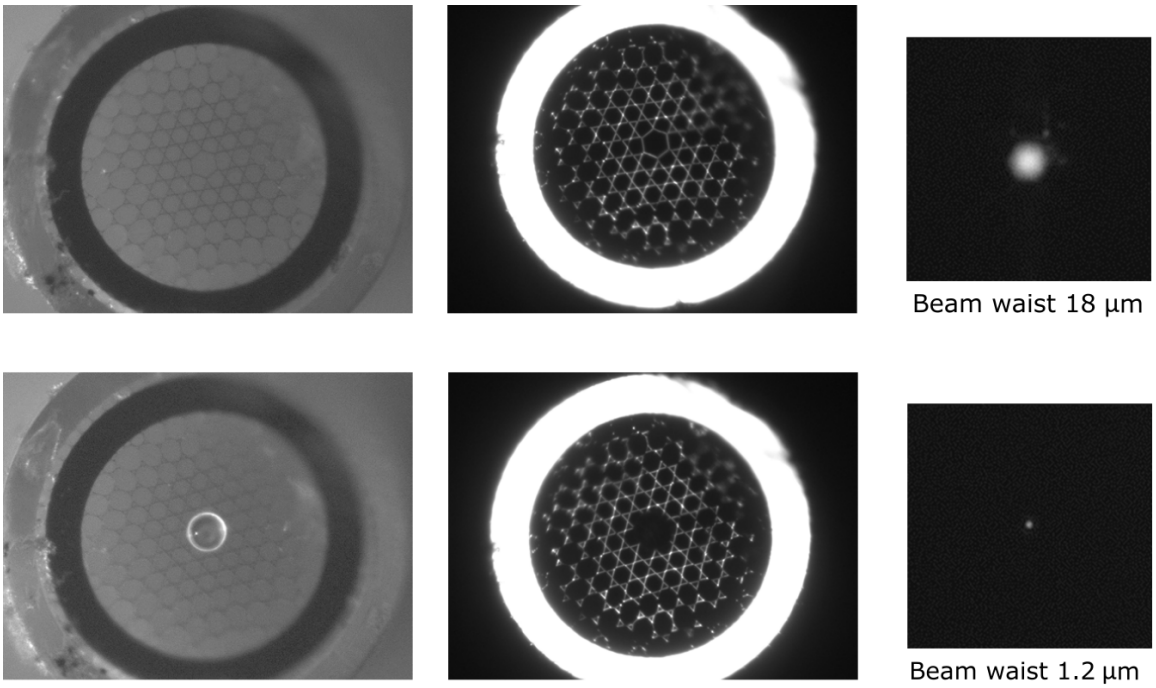

Figure 4.18: Effect of the micro-bead on the beam delivered by the fiber's core. Top: the Kagomé fiber has a large field diameter, on the order of 18 µm. Bottom: a transparent micro-bead creates a focused spot a few micrometers away from the fiber, increasing the core NA.

The spot size depends on the size of the bead and its refractive index. The higher the refractive index and the smaller the bead diameter, the tighter will be the focusing. Using polystyrene beads of few micrometers in diameter, the size of the focused beam is below the diffraction limit [39]. The effect is then called photonic nanojet and has been used with Kagomé fibers by Ghenuche et al. for a fluorescence fiber probe with single-molecule sensitivity [51].

Here, we used polystyrene beads at first, but soon realized that they would not sustain beam

powers higher than 10 mW, a threshold for damage of the bead. This power limit was too low for label-free nonlinear imaging. Therefore we moved to silica beads (diameter 30 μm), produced by Thermo Scientific (9000 Series Glass Particle Standards), which have slightly lower refractive index but can sustain higher powers. We have never observed damage of the silica beads, even for beam powers higher than 100 mW.

The procedure to fix a bead on the fiber core requires the use of a micrometric precision translator, such as the Nanomax stage (Thorlabs). The fiber is held on the translator and put into contact with the bead, which induces a slight deformation of the photonic structure surrounding the core. Electromagnetic interaction holds the bead on the fiber, and can be used for imaging. We found that the bead would sustain, without falling off, the driving frequencies and scan amplitudes that are impressed during imaging. However, a more stable fixation for handling and integration in an endoscope probe can be done by means of a CO_2 laser, which can slightly melt the bead on the fiber, without significantly affecting its focusing properties. This procedure will be described in detail in Ch. 6.

4.4.2 Signal collection through the double-clad

The double clad surrounding the photonic structure increases the collection surface, NA and therefore the overall collection efficiency of the fiber. This is well known in single fiber endoscopy, where double clad fibers are commonly used [32, 105, 151].

Moreover, these fibers reduce the sensitivity to the chromaticism of the optical systems and avoids rejection of scattered photons. This is very important in SHG and CARS imaging, where the radiation pattern is not isotropic and depends on structural features of the sample. Epi-radiation is very strong when generated by sub-wavelength objects or at the interface between two materials. In other situations the epi signal is suppressed by destructive interference of the CARS field generated in the backward direction. However, epi-CARS (and SHG) imaging is possible in thick tissues, thanks to the forward-emitted and back-scattered radiation [36]. For this reason, the use of a double-clad fiber is very important to avoid loss of the important back-scattered photons.

We performed an experiment to verify that the DC of the Kagomé can collect the nonlinear signal generated when photon scattering occurs. We studied the spatial distribution of the TPEF signal collected by the fiber when a homogeneous fluorescein (FITC) solution, placed on the fiber distal end, was excited at 900 nm (detection band 500 to 600 nm). A small area detector (APD), with a sensor square side of 160-180 μm was placed in a conjugate plane of the fiber proximal face (Fig. 4.19). The magnification from the fiber to the APD plane was approximately M=4.5, which gave an outer diameter of 1.1 mm of the collection clad's image on the APD plane. This magnification was enough to resolve the different features of the fiber cross section (collection clad, photonic structure and core), as shown in Fig. 4.20b.

We measured the TPEF signal collected by the fiber in two situations: with and without light

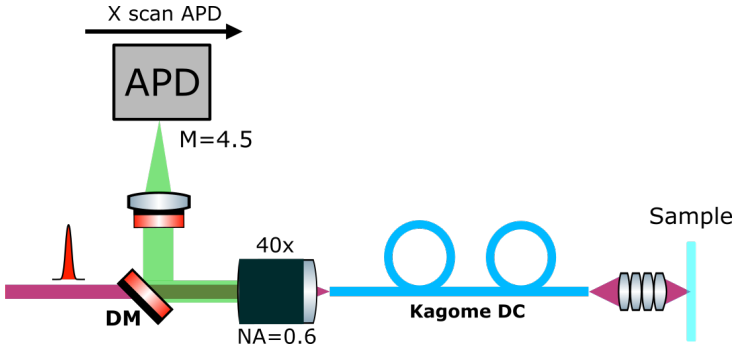

Figure 4.19: Experimental setup for the study of the spatial distribution of the collected signal, in presence and absence of scattering.

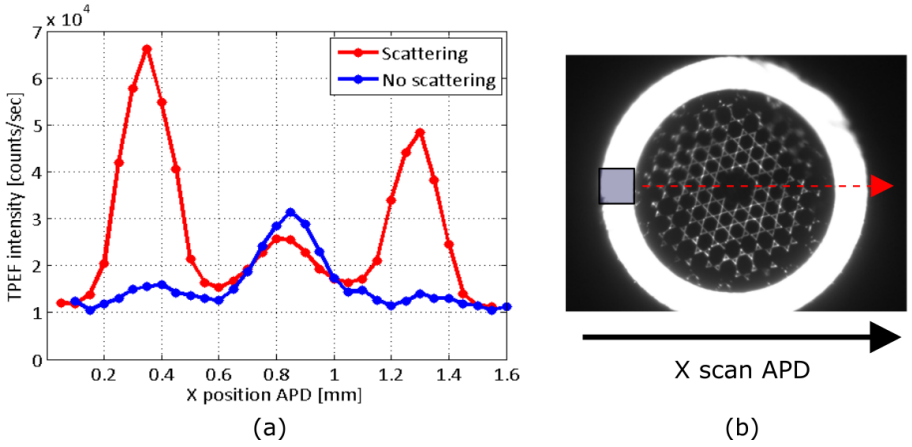

Figure 4.20: (a) Spatial distribution of the signal collected by the fiber from an homogeneous fluorescein solution. When a scattering layer is placed behind the sample, the double clad collects light as well (red curve), while in absence of scattering most of the signal is collected by the core (blue curve). (b) The square represents the dimensions of the APD, that is scanned over the fiber image.

scattering at the sample. Photon back-scattering was obtained by adding a TiO_2 layer behind the FITC solution. Titanium dioxide is a strong light scatterer and does not absorb in the visible light range. We performed a spatial lateral scan of the APD on the fiber image plane, with 50 μm scan step, and acquired the TPEF signal in the different points. The results, shown in the graph of Fig. 4.20a, are quite clear: when the fluorescence photons are not scattered (blue curve), they will be only coupled back in the fiber core. However, in presence of diffusion, the signal is collected by the fiber clad as well. Moreover, we can observe that the photonic structure does not significantly contribute to the signal collection. Future designs of the Kagomé will aim at a reduction of its dimensions, in order to increase the overall collection efficiency of the fiber.

It is important to note that, in absence of scattering, the ratio between forward and epi-detected signal from a FITC solution, when using a large area detector (PMT), is about 10^{-2}. This is due to the high transmission losses, of the fiber core, in the $450 - 650$ nm spectral region (Fig. 4.17c). If possible, a fiber design with low losses in this spectral region would certainly improve the collection efficiency of the fiber. However, this should not impair the delivery of the excitation beams. A different design should aim at a broader transmission window, rather than just shifting it to higher frequencies.

4.5 Lens assembly for the multimodal endoscope

The focusing optics plays an important role in the endoscope probe. We have discussed in Sec. 4.4.1 the relation existing between FOV, resolution and magnification of the optical system. Other parameters such as working distance, NA, transmission are also important in defining the optical behavior of the probe.

Two different type of solutions can be employed for beam focusing: GRIN lenses and miniature lens assemblies. The first ones have been used in TPEF/SHG microendoscope probes mainly because of their reduced dimensions, which can be less than 1 mm in diameter [105, 47]. Moreover, GRIN lenses optimized for nonlinear imaging are produced by companies such as GRINTECH (Jena, Germany).

The problem with this type of lenses is that in general they suffer strong chromatic aberrations [151]. For CARS imaging, it is important that the pump and Stokes beams precisely overlap on the sample. It has been shown that chromatic aberrations make normal GRIN lenses for efficient activation of CARS radiation [140]. While the use of correction elements for GRIN lenses can make them achromatic on two wavelengths, custom designed miniature lenses assemblies are the choice of preference in CARS probes [129, 18, 99]. We designed an optical system based on four achromatic doublets, using the optical design software Zemax. The lenses are produced by Edmund Optics and have different focal lengths: 9 mm (EO # 83-338), 6 mm (EO # 65-569), 4 mm (EO # 65-568) and 3 mm (EO # 65-567). These lenses are coated with MgF_2 which minimizes the reflection in the visible range.

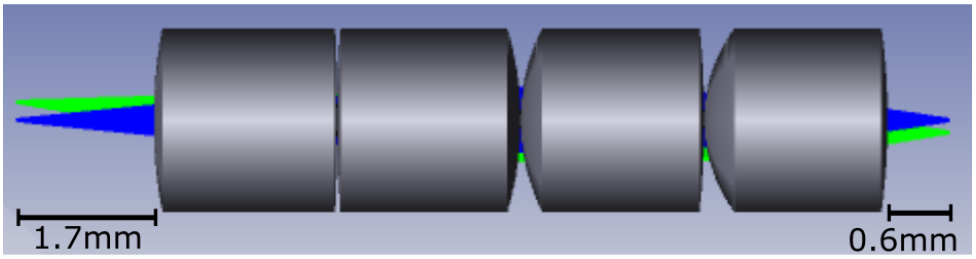

Figure 4.21: Lens assembly used for the endoscope probe. From left to right, the lenses have focal length: 9 mm, 6 mm, 4 mm, 3 mm.

We took inspiration from the miniature optical system described in [151] and [31]. Here, three lenses were used to collimate the beam and then focus it on the sample. Our system has a higher NA (0.3) on the fiber side, to efficiently collect the beams focused by the micro-bead. The overall magnification of the system is also increased (0.63), which is beneficial for the FOV of the probe, with no loss in resolution since the focusing is already at the diffraction limit To summarize, the optical properties of the 4-lenses system are:

- Distance from the front lens to the focus (working distance): W.D.=0.6 mm
- Magnification from fiber to sample: M=0.63
- Numerical aperture on the sample side: NA=0.45
- Numerical aperture on the fiber side: NA=0.3

As we will see in the next chapter, this miniaturized lens assembly gives satisfying results when performing CARS imaging using 800 nm and 1040 nm excitation beams. The results obtained with the microlenses are comparable to those obtained with bulk optics (microscope objectives). This means that chromatic aberrations of the miniature optical system are sufficiently small not to affect the CARS excitation process.

Off-axis aberrations Geometrical aberrations can cause a degradation in the quality of the focal spot. This results in a less efficient activation of the signal, as the peak of the intensity profile is reduced. This effect can be observed when imaging a homogeneous solution on a large FOV, and is typically seen as a signal drop at the periphery of the image.

In order to estimate the maximum FOV attainable with the micro-objective, we image the focal spot on a camera, as the fiber is displaced from the optical axis (Fig. 4.22). The intensity profile of the focused beam is the typical Airy disk that result from diffraction. The beam profile is not significantly as we move the fiber up to a displacement of 250 μm. However, when the fiber tip is displaced by 350 μm from the optical axis, the beam profile becomes slightly asymmetric. The focal spot becomes a line when the fiber is 450 μm from the center.

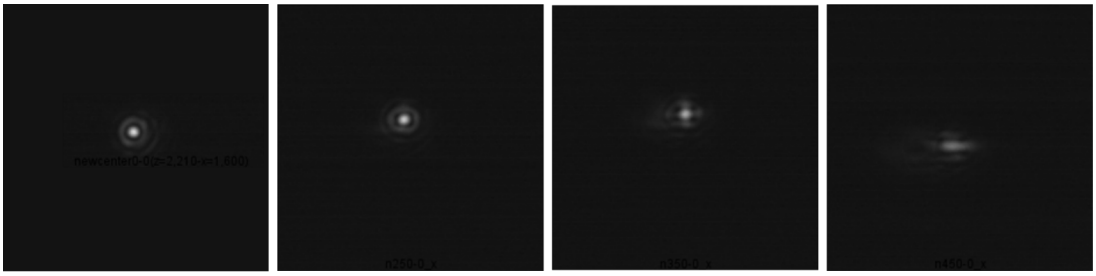

Figure 4.22: Image of the focal spot as a function of the distance from the optical axis.

From this study, we can expect that the excitation on the sample will be uniform on a FOV of at least 315 μm, which results from a 500 μm scan (with a magnification of 0.63).

4.6 Conclusions

In this chapter we have described the main features of the fiber-scanning imaging device, that constitutes the core of the nonlinear endoscope probe. We have seen that the fiber displacement can reach several hundreds of micrometers when driven at resonance. This enables to perform 2D imaging of samples with large FOVs and high resolution. We identified and optimized experimental details that allows us to achieve large FOVs at safe driving voltages. We have seen how imaging is performed using a data acquisition board and LabView softwares that synchronize the piezo driving with the signal acquisition. The use of a PSD to measure the fiber trajectory allows to reconstruct the images with no distortions due to deviations of the scanner behavior from the theoretical one. We have presented additional features of the custom designed optical fiber, such as a double-clad to enhance the collection of nonlinear signal from scattering tissues and a silica micro-bead to increase the excitation NA. At last we have described the miniature microscope objective that we designed to work in the endoscope probe.

Chapter 5

Multimodal endoscopic imaging

In the last chapter, we described the development of a miniature imaging device, based on a Kagomé DC fiber. As we will see in this chapter, the use of this novel photonic crystal fiber will allow use to perform simultaneous[1] TPEF, SHG and CARS endoscopy of biological tissues.

In Sec. 5.1 we describe the experimental setup. In Sec. 5.2 we image test samples, with different imaging modalities, using microscope objectives. This is a validation of the fiber scanner and serves as a reference to evaluate the performance of the micro-lenses. In Sec. 5.3 we characterize the miniature system, using micro-lenses, in terms of FOV and spatial resolution. The rest of the chapter is dedicated to multimodal imaging of different samples. We find that the performances of the system are close to the results obtained with bulk optical elements. This was verified in both SHG and CARS, which confirms the good chromatic performance of the micro-lenses assembly. The peculiarity of this system is the capability to activate femtosecond TPEF, SHG and CARS contrasts, something that cannot be achieved with classical optical fibers. This allows us to image ex-vivo biological tissues in endoscopic modality (in epi-detection), combining different contrast mechanisms.

5.1 The experimental setup

Figure 5.1 depicts the experimental setup for endoscopic nonlinear imaging. The laser source is a single box, dual output tunable system (Discovery, Coherent), delivering 100 fs pulses. One beam is fixed at 1040 nm, while the other one can be tuned from 700 nm to 1300 nm. The broad spectrum of these femtosecond pulses results in a low spectral resolution in CRS imaging. However, the short pulse duration increases the activation efficiency of nonlinear contrasts. This reduces the average power that needs to be delivered on the sample.

Both the pump and the Stokes beam, delivered by the laser, pass through a half-wave plate

[1] Since we use a single detector, a change of the optical filter is required, in order to image with different modalities.

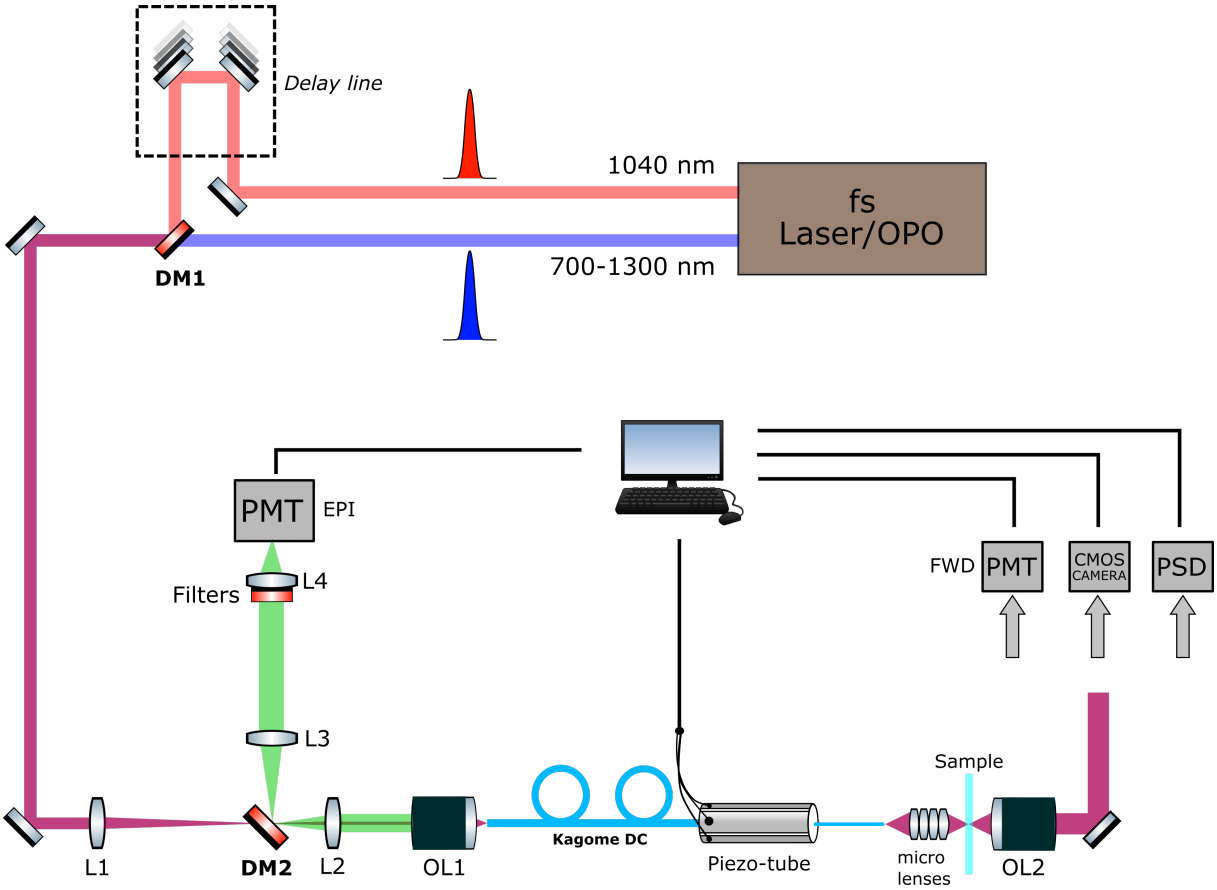

Figure 5.1: The setup for nonlinear endoscopic imaging. Legend for the optical elements: L1: f=400mm, L2: f=40mm, L3=100mm, L4:50mm; OL1 and OL4: 60x Olympus, NA=0.6; OL2 and OL3: 40x Olympus NA=0.45; DM: Dichroic Mirror, Long-pass (LP) 650nm. Filters: Short-pass 690nm. PMT: Photomultiplier tube. PSD: Position sensitive detector.

(HWP) and a Glan Taylor polarizer, to control the delivered power. A mechanical delay line, consisting of two mirrors mounted on a translation stage, changes the optical path length of the 1040 nm beam. This allows to adjust the temporal overlap between the pump and Stokes pulses. The beams are then spatially combined using a notch dichroic filter (NFD01-1040, Semrock), optimized for the reflection of the 1040 nm beam, with the transmission coefficient $T < 2\%$ at 1040 nm and $T > 93\%$ between 400 nm and 980 nm, and between 1110 nm and 1300 nm.

The excitation beam size is adjusted using a telescope, before being injected into the fiber with a 40x microscope objective (Olympus, NA=0.6). We use the 0.6 NA objective to avoid losses in the signal collected by the external clad of the fiber, whose NA is 0.5 at 400 nm. Therefore it is necessary to reduce the excitation beams size (by a factor x10). In fact, for an efficient coupling, the NA of the incoming beams has to match the NA of the Kagomé fiber core (NA=0.02).

The excitation beams are delivered by the Kagomé fiber and focused by the micro-bead. The focal spot is then re-imaged on the sample plane by some optical elements. For a first characterization of the fiber-scanner we used two back-to-back microscope objectives (Olympus 20x, NA=0.45). This system yields to a magnification M=1 from the fiber to the sample plane. The imaging results obtained with the microscope objectives are presented in Sec. 5.2. All the other results were obtained with the miniature lens assembly described in Sec. 4.5. The NA of the miniature objective is 0.3 on the fiber side and 0.45 on the sample side. The magnification from the fiber to the sample is M=0.63.

The nonlinear signal generated at the sample is collected by the focusing optics and coupled in the Kagomé fiber. We use a dichroic mirror (long-pass, 720 nm) to separate the signal from the excitation beams at the proximal end of the fiber. Wavelengths lower than 720 nm are reflected to the detector. The dichroic mirror reflects the SHG signal (400 nm) excited at 800 nm and the TPEF signal (between 400 nm and 600 nm, depending on the fluorescence emitters). In CARS imaging, when we target the CH_2 anti-symmetric stretch (2854 cm^{-1}), the pump and Stokes wavelengths are 800 nm and 1040 nm, respectively. The anti-Stokes radiation is then generated at the wavelength λ_{CARS}=650 nm, which is reflected by the mirror. The detection path is composed of the following optical elements: the objective lens (OL1, $\mathrm{f} = 4.5\ \mathrm{mm}$), a 40 mm lens (L2), a 100 mm lens (L3) and a 50 mm lens (L4). The overall magnification of the system, from the fiber to the detector, is $\mathrm{M} = 4.5$. The fiber (d=250 $\mu\mathrm{m}$) is easily imaged within the photocatode of the detector (5 mm side). The detector is a photon counting PMT[2] (H7421-40, Hamamatsu). The GaAsP/GaAs photocathode ensures a high quantum efficiency (QE), as compared to other types of PMTs. The sensitive wavelength range goes from 300 nm to 720 nm, with a 40% QE peak at 580 nm.

In the forward direction, we use a 40x objective (Olympus, NA=0.6) to collect both the excitation beams and the forward emitted signal. The sample plane is imaged on a CCD camera,

[2]Photomultiplier tube.

through the 40x objective and a tube lens (f=150 mm, $M \approx 33$). A flip-mirror, placed behind the objective, is used to image the scan pattern on the PSD (PDP90A, Thorlabs) and acquire the scan positions. Another flip-mirror in front of the PMT allows to detect the forward emitted signal in thin samples, such as fluorescent beads or polystyrene beads.

This represents the core of the endoscope setup. It is a compact system and does not require pre-compensation schemes to correct for dispersion/non-linearity occurring in the fiber. Excitation over the 400 nm width of the Kagomé transmission window can be accessed by simple tuning of the laser. No FWM suppression element needs to be inserted after the delivery fiber. The same fiber can be used both for excitation and collection of the CARS signal. These are unique features made possible by the Kagomé DC fiber.

5.2 Characterization with bulk optics

In order to validate the imaging capabilities of the system described in Ch. 4, we first performed a characterization using microscope objectives to relay the spot from the fiber to the sample. Two air objectives (Olympus, 20x, NA=0.45), in back-to-back configuration, made an image of the fiber tip on the sample. The focal spot and the scan pattern were reproduced, with no magnification (M=1). Images obtained using bulk optics are considered as a reference, since imaging is performed in the best optical conditions, in terms of geometric and chromatic aberrations. They will be compared to those obtained with the micro-lenses.

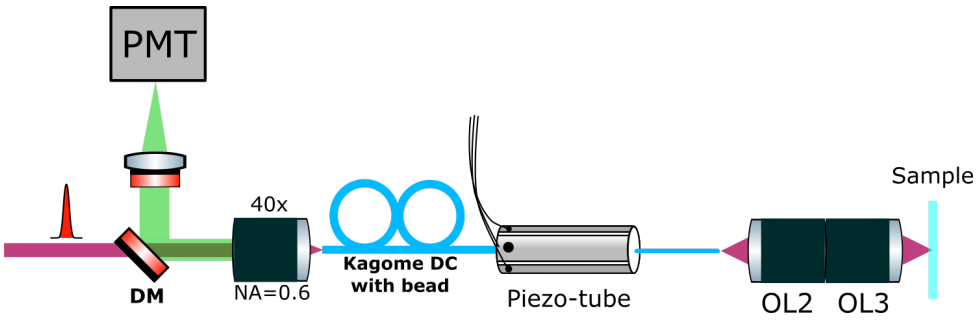

Figure 5.2: Characterization of the imaging system was first performed with bulk optical elements to focus on the sample (OL2 and OL3 in the setup). Two back-to-back microscope objectives (20x, NA=0.45, Olympus) were used as imaging elements from the fiber to sample. The overall magnification of the system was M=1.

For all the images, we used the spiral pattern described in Sec. 4.2, with a 0.8 s expanding pattern and a rest time of 0.5 s. We imaged thin samples, such as fluorescent and polystyrene beads, in the forward direction. Thick samples, such as rat tail tendon and lipid-rich colon tissues, were imaged in endoscopic modality.

5.2.1 Transmission images

The USAF-1951 resolution test chart is a periodic pattern composed of several groups, containing 6 elements each. Groups -2 and -1 are on the outer sides of the chart, with their elements ordered from 1 to 6. The pattern repeats as we go closer to the center, where elements are smaller. Increasing group numbers correspond to smaller elements in the chart. Every element is characterized by three vertical and horizontal bars. For each element, the number of line pairs per millimeter (lp/mm) is specified. The inverse of this number is the distance between the bars (in mm).

We imaged the USAF-1951 resolution test chart in transmission. The laser intensity was detected with a photodiode (DET10A, Thorlabs), as the laser spot was scanned on the transmission chart. Imaging the USAF-1951 chart is a very important step, since it is a precise measure of the FOV of the imaging system. In addition, it allows to validate the scan and reconstruction algorithms. Finally it will reveal the presence of different optical aberrations. The FOV of a scan is

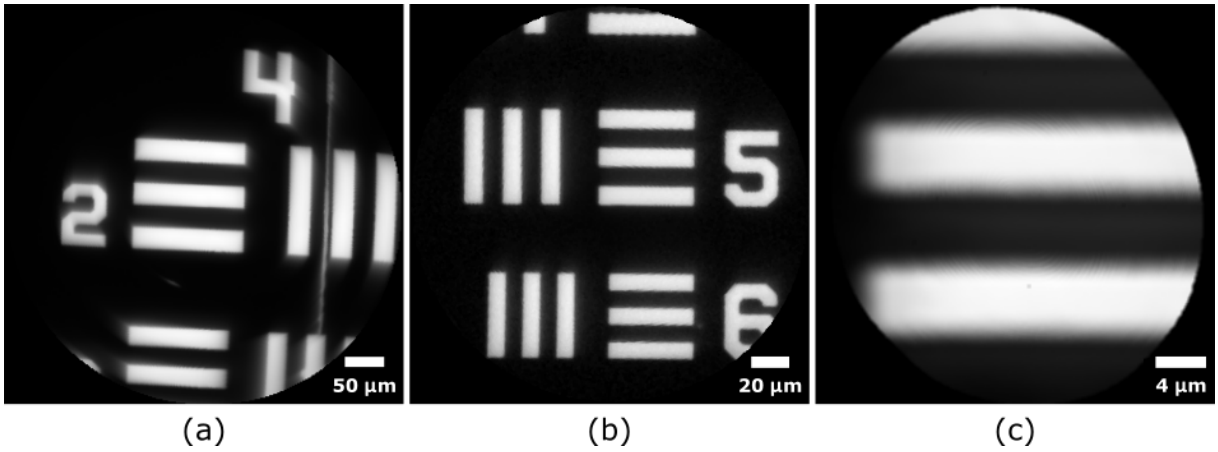

Figure 5.3: (a) Element 2 of group 4 in the USAF-1951 resolution chart, imaged with 15V. (b) and (c), element 5 of group 5 in the chart, imaged with 7.5 V (b) and 3.75 V (c).

obtained by measuring the distance between the bars in an image. This distance is measured in pixel units in the image, while it is known in millimeters for all elements of the chart. Then, the ratio between the distance in micrometers and the one in pixels gives the pixel size. The FOV is the pixel size times the number of pixels in the image. As an example, Fig. 5.3a shows element 2 of group 4, imaged with the maximum voltage amplitude (± 15 V). This element has 17.96 lp/mm, which corresponds to a distance between the bars of 55.7 μm. The distance between the bars in the image is expressed in pixel, and can be converted to micrometers. This gives the size of the imaged area, also known as the FOV, which is 510 μm for Fig. 5.3a. One can notice a slight defocus on the side elements. This might be due to the fiber trajectory, that describes an arc (resulting in a curved surface when the spot is scanned over the sample). In fact, this aberration effect disappears when imaging smaller FOVs (Fig. 5.3b and 5.3c).

5.2.2 TPEF and SHG

TPEF and SHG can be activated with a single laser source, such as a tunable Ti:Sa laser. We demonstrate hereafter, by imaging different samples, that the fiber delivered excitation beam can excite such contrasts.

Fluorescent beads

Images of 2 μm fluorescent beads are shown in Fig. 5.4. The emission peak of these beads is at 510 nm. We used a 550/100 nm bandpass filter to block the 900 nm excitation wavelength, whose power on the sample was 5 mW. The FOV is 51.5 μm in the image of Fig. 5.4a and 20 μm in Fig. 5.4b. The scan amplitude was 1.5 V and 0.6 V, respectively. The TPEF signal was detected in the forward direction with the PMT. Figure 5.4a demonstrates that the system is capable of resolving $2\,\mu$m objects. The measurement of the PSF (measured from the images of 200 nm fluorescent beads) was performed with the micro-lenses system and can be found by the reader in Sec. 5.3.2.

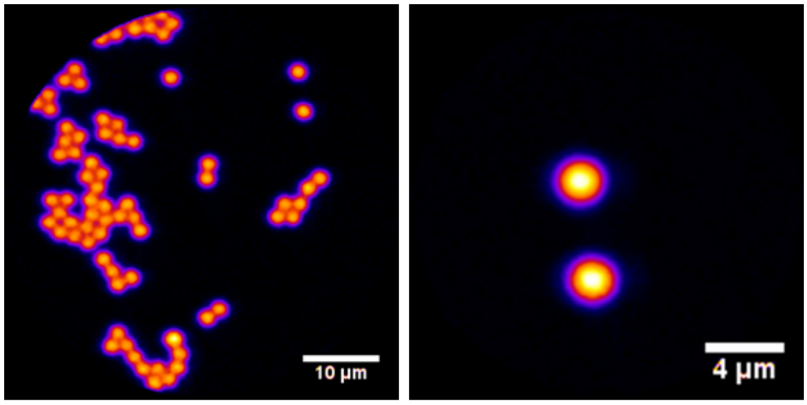

Figure 5.4: Forward detected TPEF images of 2 µm fluorescent images, using a scan amplitude of 1.5V (a) and 0.6 V (b).

Rat tail tendon

Collagen type I is the main component of connective tissues, so it is naturally present and very abundant in biological tissues. Collagen tends to aggregate in polar fibers that generate a very strong SHG signal. Rat tail tendon is one of the biological samples typically used to test SHG imaging systems. Its dry mass is composed by 80% of collagen type I fibers. Fig. 5.5 shows two different epi-detected images of a rat tail tendon, excited at 800 nm and detected at 400 nm, with 45 mW on the sample. SHG images of rat tail tendon, obtained with the micro-lenses system, can be found in Sec. 5.5.

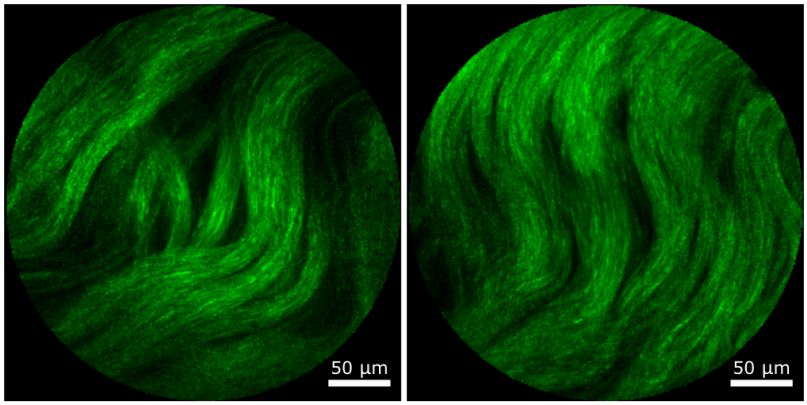

Figure 5.5: Epi-detected SHG images of two different regions in rat tail tendon, with 45 mW on the sample (average 10 images).

5.2.3 CARS imaging

We performed CARS imaging using λ_{P}=800 nm and λ_{S}=1040 nm for the pump and Stokes excitation beam. Under these conditions, the targeted vibrational frequency is $2880\,\mathrm{cm}^{-1}$ and the anti-Stokes radiation is generated at λ_{CARS}=650 nm. The use of femtosecond pulses allows to target multiple Raman lines at the same time. Therefore, we can simultaneously record both the aliphatic CH vibrations (2851 cm^{-1} and 2902 cm^{-1}) for polystyrene beads, and the $\mathrm{CH_2}$ antisymmetric stretch (2854 cm^{-1}) for lipids [154].

FWM background from the microbead

The experiments performed in Ch. 3, to characterize the FWM background in the fiber, were done using a bare Kagomé fiber (see Sec. 3.5). However, when performing imaging, we use a silica micro-bead (diameter 30 $\mu\mathrm{m}$) attached to the fiber core. In order to assess whether the micro-bead contributes to generating FWM background, we measured again the CARS signal as a function of the delay between the pump and Stokes beams. This was done with an olive oil sample, generating CARS radiation, to compare the delay position and the relative intensity of the different contributions to the signal. The laser source was the same of the experiment in Sec. 3.5. The red curves in Fig. 5.6 show the signal detected in both the forward (a) and epi (b) directions, when delivering the beams through the Kagomé fiber with the silica bead. The excitation powers on the samples were P_{P}=0.8 mW and P_{S}=0.5 mW. A neutral density filter was used in the forward detection path, transmitting 1.8% of the light. In the measurement without the micro-bead, light transmission through the filter was 3%. Therefore the intensity values of the two curves in Fig. 5.6a should not be directly compared.

From the results of Fig. 5.6, it becomes clear that the silica micro-bead on the fiber generates a FWM signal, at the delay position of 2.8 ps in this case. One can see in Fig. 5.6b that the FWM

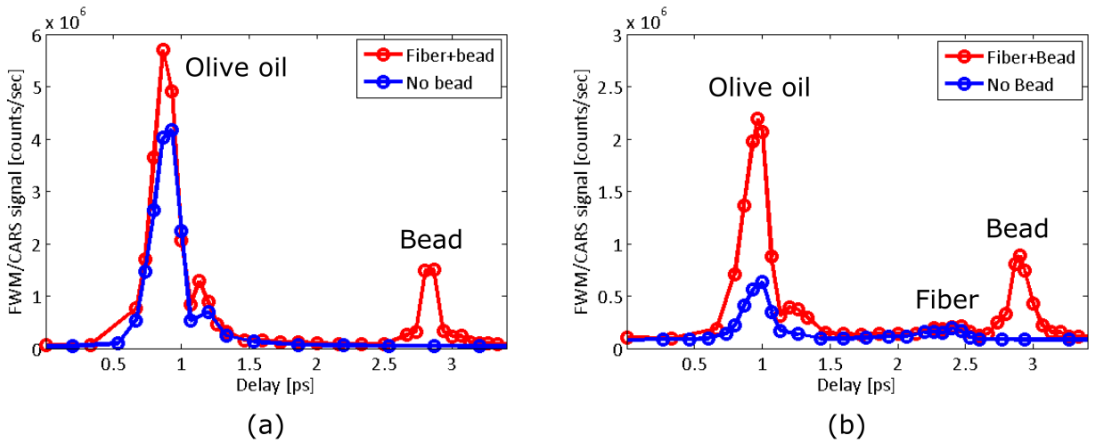

Figure 5.6: Forward (a) and epi-detected (b) FWM signal generated with an olive oil sample, for a bare Kagomé and one with the micro-bead on the core.

from the bead is separated from the one of the fiber (between 2.3 ps and 2.5 ps). This suggests that the latter one is generated at the fiber entrance. Then the pulses travel at different speed in the fiber, because of the anomalous dispersion. The CARS signal generated from olive oil occurs at a delay position of about 1 ps. The peak separation between the bead and the sample is due to the GVD of the microscope objectives.

The FWM background generated by the bead might affect CARS imaging, whether it overlaps with the signal from the sample. This is not the case when using microscope objectives, because the GVD of the lenses introduces a time difference between the microbead and the sample. CARS images obtained with this optical system are free of FWM background due to the fiber delivery. In Sec. 5.4 we will study the FWM background when using the 4 micro-lenses system.

Polystyrene beads

Polystyrene beads generate a strong CARS signal, when excited near 2900 cm^{-1}. Figure 5.7 shows CARS images of 30 μm (a) and (b) and 5 μm (c) beads, that we acquired with the fiber scanning device. The CARS signal, detected in the forward direction, was excited with P_{P}=0.8 mW and $\mathrm{P_S}$=0.5 mW on the sample. When the pump and Stokes pulses do not overlap, the signal from the beads vanishes (images not shown). When the pulses temporally overlap on the sample, no FWM background is generated by the micro-bead. As a consequence, the images are characterized by a very good SNR.

We obtained images of the same beads in the epi direction (Fig. 5.8b), but using higher excitation powers (P_{P}=5.6 mW and $\mathrm{P_S}$=3 mW.).

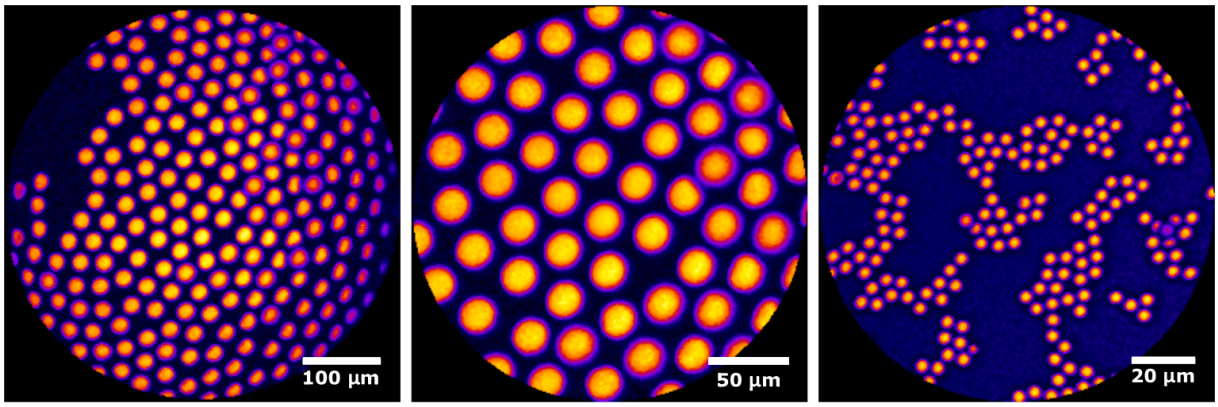

Figure 5.7: Forward detected CARS images of 30 µm (a) and (b), and 5 µm (c) polystyrene beads.

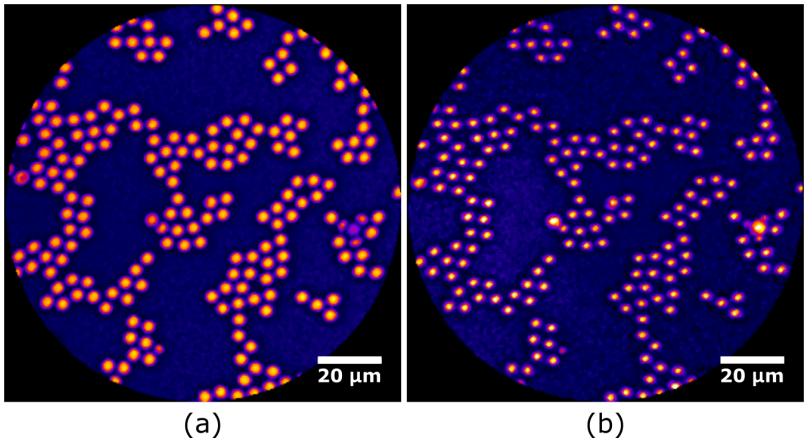

Figure 5.8: CARS images of 5 µm polystyrene beads obtained in the (a) forward direction (P_{P}=0.8 mW and P_{S}=0.5 mW), and in the (b) epi direction (P_{P}=5.6 mW and P_{S}=3 mW).

Biological tissue

In biological tissues, lipid droplets can generate a strong CARS signal. This can be explained by the abundance of CH_2 bonds in lipids, which can be targeted through its Raman active antisymmetric stretch vibration. The characteristic frequency of this vibration is around 2854 cm^{-1}. We stimulated the CARS process at this frequency by using λ_P=800 nm and λ_S=1040 nm excitation wavelengths.

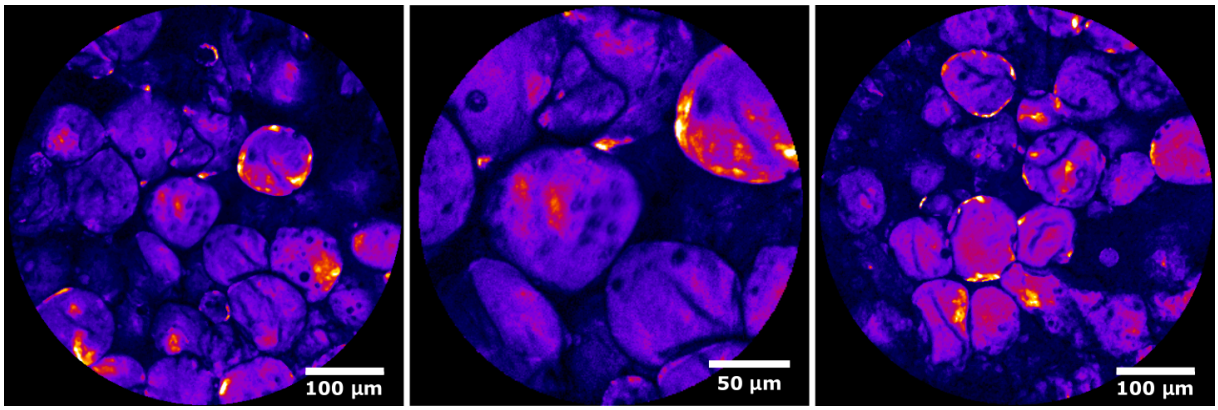

Figure 5.9: CARS images ex-vivo of the lipid cells in a human colon tissue (x10 average). The average power on the sample was 30 mW (P_P=20 mW, P_S=10 mW).

The epi-detected images of Fig. 5.9 show the CARS response from the adipose tissue of a fresh human colon tissue. The pump and Stokes excitation powers on the sample were P_P=20 mW and P_S=10 mW.

5.3 Characterization of the miniature device

We introduced in the last section the first imaging tests of our fiber-scanning device for nonlinear endoscopy. We performed imaging over large FOVs, using two back to back objectives, resolving objects as small as 2 μm. We have proved the capability of activating multiple contrast mechanisms on unlabeled biological samples (rat tail, human colon), by delivering short pulses at different wavelengths. The signal back-collected through the same fiber is then detected on the proximal side and the nonlinear images successfully reconstructed.

Microscope objectives were an important benchmark for the device, but the micro-lenses assembly has to be characterized before integration in a portable probe. For instance, the chromatic behavior of the micro-lenses system is crucial for CARS microscopy. The results will be discussed in the remaining sections of the chapter. In Fig. 5.10 we show the imaging part of the setup. One can see the piezo-tube, the free-standing fiber and the micro-lens system (described in Sec. 4.5). The integration of these elements in a portable probe will be described in Ch. 6.

This section is dedicated to the characterization of the endoscope system, in terms of both

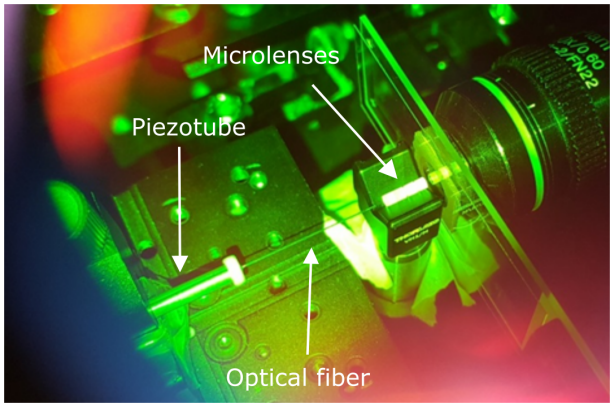

Figure 5.10: Photo of the distal part of the setup, comprising the piezo-tube, the free-standing Kagomé fiber, the microlenses and the sample. The microscope objective is used for forward detected images, for the calibration of the scan pattern and imaging on a CMOS camera.

the spatial resolution and the FOV. We will show that we achieve sub-micrometer resolution with large FOV ($> 300\,\mu m$), using low driving voltages (± 15 V).

5.3.1 Transmission images

At first we imaged a USAF resolution chart to measure the FOV. From the group 6 of the chart (Fig. 5.11), we retrieved the FOV corresponding to the maximum scan amplitude (320 μm). This is consistent with the scan amplitude measured in the last section (510 μm) and the magnification from the fiber to the sample with the miniature objective (M=0.63). The quality of these images is comparable to the ones obtained with microscope objectives (Sec. 5.2.1).

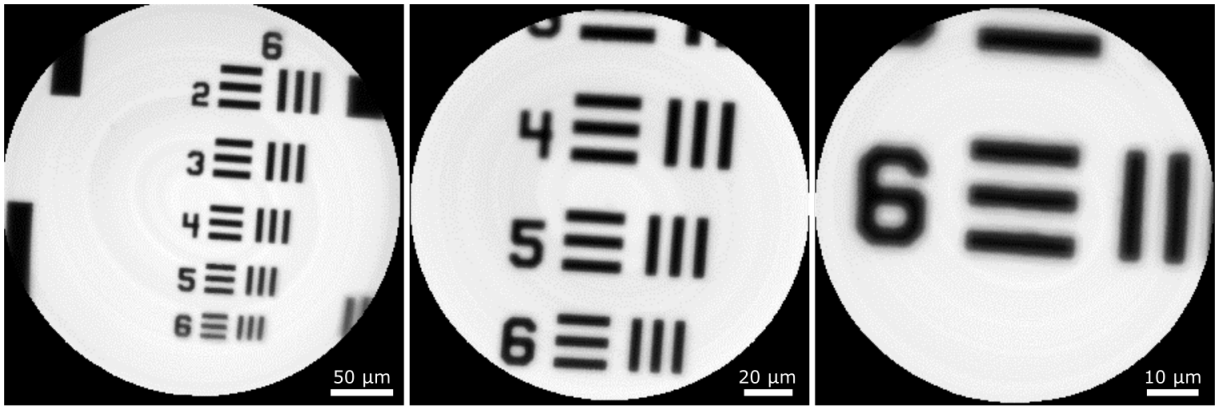

Figure 5.11: Transmission images of group 5 in the USAF-1951 resolution chart. The images were obtained with 15 V (a), 7.5 V (b) and 2 V (c) scan amplitudes.

5.3.2 Point spread function

The Point Spread Function (PSF) is defined as the response of an imaging system to a point source. As a result of the finite size of optical elements, any imaging system is limited in spatial resolution by the diffraction of light. The resolution of an optical system is closely related to the PSF, but its definition is arbitrary and different criteria can be adopted. However, it is common use in NLOM to define the resolution of a microscope as the FWHM of the PSF [29].

The PSF of a TPEF microscope depends on the spatial intensity profile of the excitation beam. The extension of the beam in the lateral and axial directions defines the size of the volume where molecules are excited. This in turns depends on the NA of the focusing lens and on the excitation wavelength λ. The theoretical values of r_{xy} and r_{z}, the lateral and axial resolutions, are [29]:

$$r_{\mathrm{xy}} = \frac{0.46\lambda}{NA} \tag{5.1}$$

$$r_{\mathrm{z}} = \frac{1.4n\lambda}{NA^2} \tag{5.2}$$

In order to measure the PSF of the endoscope, we imaged fluorescent beads with 200 nm diameter. The size of the beads is below the expected resolving power of the imaging system, which makes them suitable to mimic a point source. Therefore, the shape of these beads in the TPEF images represents the PSF of the system. The beads were deposed on a glass cover-slip

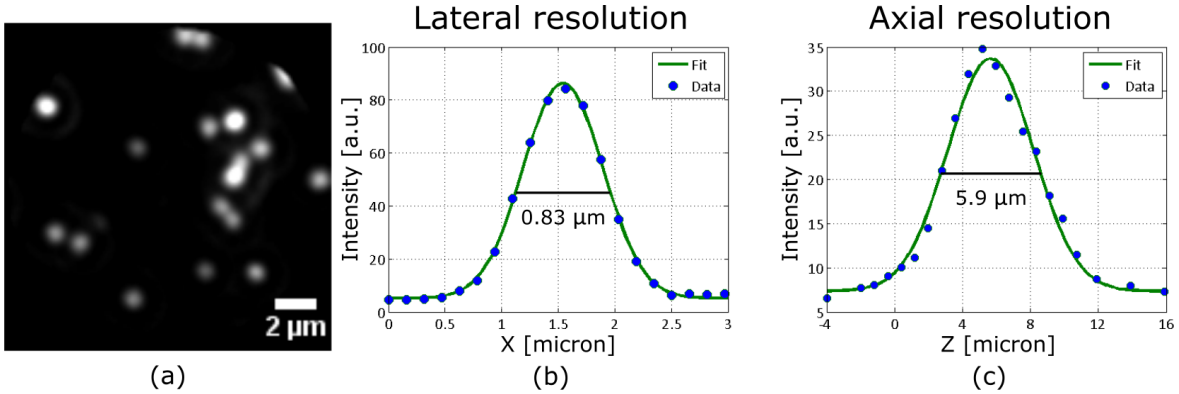

Figure 5.12: (a) Forward detected TPEF images of 200 nm fluorescent beads. The graphs show the data points and the Gaussian fit for the lateral (b) and axial (c) resolution.

and excited at 800 nm. The signal was collected in the forward direction, with the 40x objective (Fig. 5.1). Different images, such as the one in Fig. 5.12a, were acquired. The FOV of the image was approximately 16 μm in diameter (scan voltage 0.5 V), which was measured with the USAF-1951 resolution chart (Sec. 5.3.1). The intensity profile of 6 different beads was averaged and fitted with a Gaussian curve. The lateral resolution of the endoscope was measured, as the average FWHM of the beads intensity profile: $r_{\mathrm{xy}} = 0.83\,\mu\mathrm{m}$.

In order to measure the axial resolution, we exploited the fine translation of the fiber holder,

rather than moving the sample. We acquired images of the beads as the fiber was moved in steps of 2 μm in the axial direction. This corresponded to a 0.8 μm displacement of the focus in the axial direction on the sample, since the axial magnification is equal to M^2. The axial profile of three different beads was averaged and fitted with a Gaussian curve, the FWHM of which was measured to be $r_z = 5.9\,\mu$m.

The measured values of the PSF are close to the theoretical values of a system with a focusing NA=0.45 and excitation wavelength λ=800 nm. From Eqs. 5.1 and 5.2, we can find the expected values for our system: r_{xy}=0.82 μm and r_z=5.5 μm.

The PSF measurement highlights the capability of the endoscope to perform nonlinear imaging over large FOVs ($> 300\,\mu$m), with a sub-micrometer lateral resolution, thanks to the focusing micro-bead placed on the fiber core.

5.4 CARS imaging: background and polystyrene beads

The use of miniature optics for CARS imaging can cause two issues. The first one is related the FWM generated by the micro-bead on the fiber. This was not a problem with bulk optics, because the GVD of the microscope objectives introduced a delay between the pulses. This shifted the position of the overlap on the bead from the one on the sample (see Fig. 5.6). The second question is about the chromatic performance of the micro-lens system. As said before, a shift in the focal position of pump and Stokes beams, due to chromatic aberrations, would reduce the efficiency of activation of the CARS signal. In order to compare the miniature system to the microscope objectives, we imaged polystyrene beads using the same power levels used with microscope objectives.

Background with the micro-lenses system

Figure 5.13 shows the signal generated at the CARS wavelength, when delivering the Pump (800 nm) and Stokes (1040 nm) beam to the sample. The epi-detected signal in presence and absence of an olive oil sample was measured, as a function of the input delay between the pulses. The peak generated by the micro-bead can be identified in the blue curve, which represents the signal with no sample. The background signal is increased by reflection from the glass coverslip of the sample (red curve). An inspection of the red curve makes clear that the micro-bead background is zero when the pulses overlap on the sample. This must be due to the group velocity mismatch introduced by micro-lenses. This means that femtosecond CARS imaging with the Kagomé endoscope does not require elements to suppress the FWM background after the fiber, in contrast to what happens with all the fiber-delivered CARS probes developed so far.

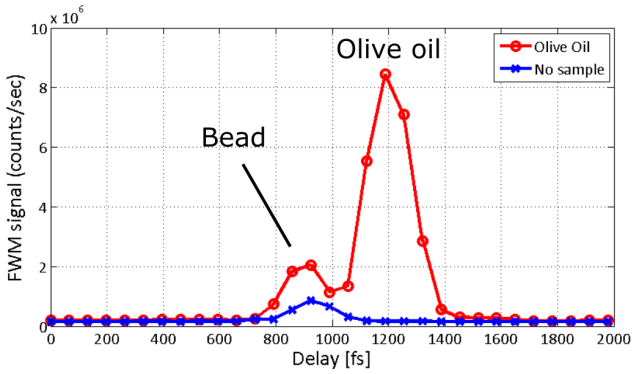

Figure 5.13: Epi-detected FWM signal with an olive oil sample (red curve) and no sample (blue curve). The GVD of the micro-lenses is sufficient to separate the pulses in time from the micro-bead to the sample.

Polystyrene beads

Figure 5.14 shows the images of 30 μm polystyrene beads. These were obtained in the same excitation conditions (P_P=0.8 mW and P_S=0.5 mW) of the ones obtained with microscope objectives (Fig. 5.7). The CARS signal was forward collected with the 40x objective lens (OL2 in Fig. 5.1). The SNR of these images is comparable to that obtained with the objective lenses, with a CARS signal from the polystyrene beads on the order of few million counts per second. The elongated shape of the beads in the images might be due to an angle of the sample or a

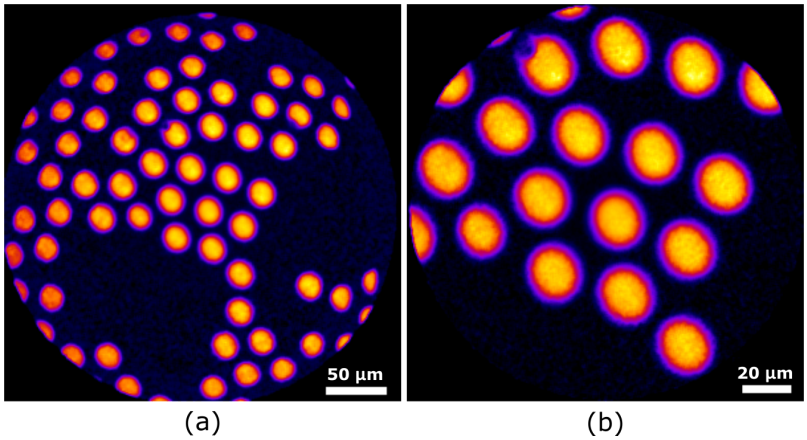

Figure 5.14: (a) 10 V and (b) 5 V scan images of 30 micron polystyrene beads, acquired in the forward direction (x5 average, P_P=0.8 mW and P_S=0.5 mW).

slight change in the fiber scan pattern, as compared to the measured reference positions.

5.5 SHG imaging of rat tail tendon

We imaged a rat tail tendon sample, whose collagen fibers give a strong SHG response. We excited the sample with 48 mW, using 800 nm excitation wavelength 400 nm signal detection. In Fig. 5.15, the same area of the sample is imaged with different scan amplitude. The FOV of the image in Fig. 5.15c is 31 μm, and one can appreciate the high resolution of the imaging system, which allows to distinguish parallel fibers with sub-micrometer width. Figure 5.16 shows a

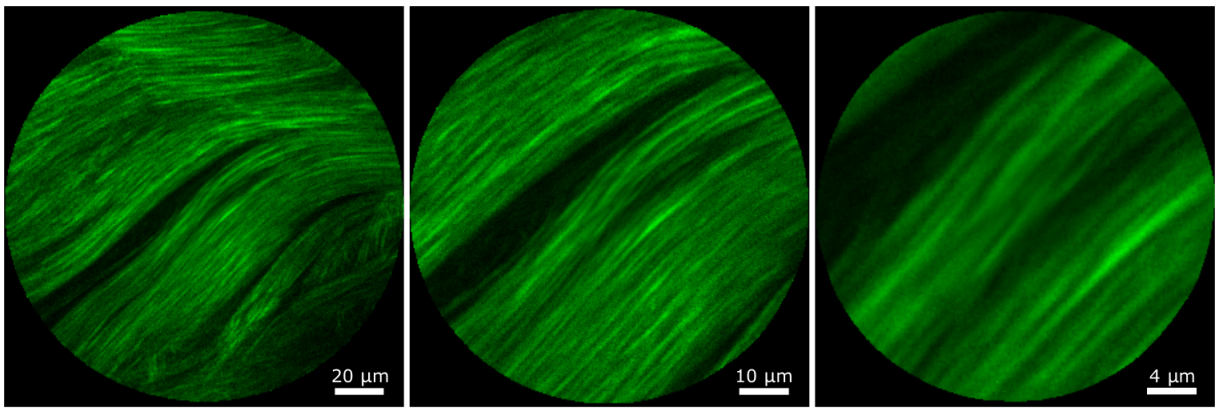

Figure 5.15: Collagen fibers in a rat tail tendon, imaged ex vivo with SHG contrast (x10 averaged frames). The excitation power on the sample was 48 mW. The images show the same area of the sample with a scan amplitude of 7.5 V (a), 3.75 V (b) and 1.5 V (c).

comparison between a raw image obtained with a single acquisition (a) and the average of 10 acquisitions (b). The SNR is clearly improved by averaging over multiple images, however the quality of a single acquisition is sufficiently high to resolve the different fibers. The SNR at the center of the image is higher than in the periphery. This effect is due to the highest sampling of the central area, a consequence of the transitory regime at the beginning of the scan (see Sec. 4.2).

5.6 Multimodal imaging of human colon

In this section, we describe the application of the endoscope to multimodal nonlinear imaging of human colon tissues. Colon is in the last part of the gastrointestinal tract. Here, water is absorbed and the remaining wastes from food are converted to faeces and subsequently expelled by the anus. Colon is an organ where endoscopic exams are routinely performed in hospitals, in order to assess the presence of abnormal tissues, such as polyps. The nature of polyps is not always malignant, and histological analysis is necessary to determine whether they are associated to a tumor. In the colon, tumors usually first develop in the mucosa, which is the inner part of the gastrointestinal (GI) tract (fig. 5.17). As the disease progresses, cancer cells invade deeper

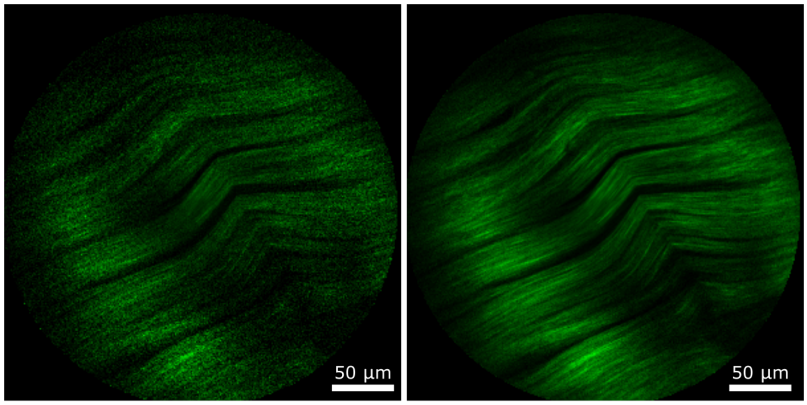

Figure 5.16: SHG image of rat tail tendon: comparison between a single acquisition (a) and the average of 10 frames (b). Excitation power on the sample P_{exc}=48 mW.

in the tissues below the mucosa, reaching the submucosa and circular muscle. Multiphoton imaging of these tissues relies on a combination of TPEF, SHG and CARS, to visualize proteins, collagen and lipids (see Sec. 1.1.5). In-situ diagnosis, based on nonlinear endoscopy, would avoid biopsy and save the time required by histological fixation and staining (≈ 24 hours). This technique could be equally applied to the whole digestive system (esophagus, rectum, pancreas, etc...).

5.6.1 Imaging of the muscle layer in histology slides

The images in Fig. 5.18 show the combined forward-detected TPEF (red) and SHG (green) response from a 30 μm thick slice of human colon tissue. The samples were unstained, but fixed using the common procedure used for histology samples. The tissue was prepared by the histopathologist at IPC (Institut Paoli-Calmette, Marseille), in the frame of a collaboration with Mosaic group at Institut Fresnel. The goal of this project is to test different NLOM techniques as potential optical biopsy methods. Multiphoton imaging of healthy and cancerous colon tissues is performed, comparing the results with conventional H&E histology images. This is an interesting study for the future of our system, since colon is an organ where endoscopy is routinely performed in clinics with forward-viewing endoscopes.

The multiphoton images of the histology samples (Fig. 5.18) demonstrate that we can activate intrinsic contrasts from unlabeled biological tissues with the fiber-scanning system. The SHG response comes from the collagen fibers, while the TPEF signal is due to the autofluorescence of proteins present in the tissue, such as the elastin. The structure of the tissue suggests that the muscle layer of the colon was imaged.

In absence of scattering from the tissue, most of the SHG signal propagated freely in the forward direction, while the epi-fluorescence signal was not intense enough. Therefore, we

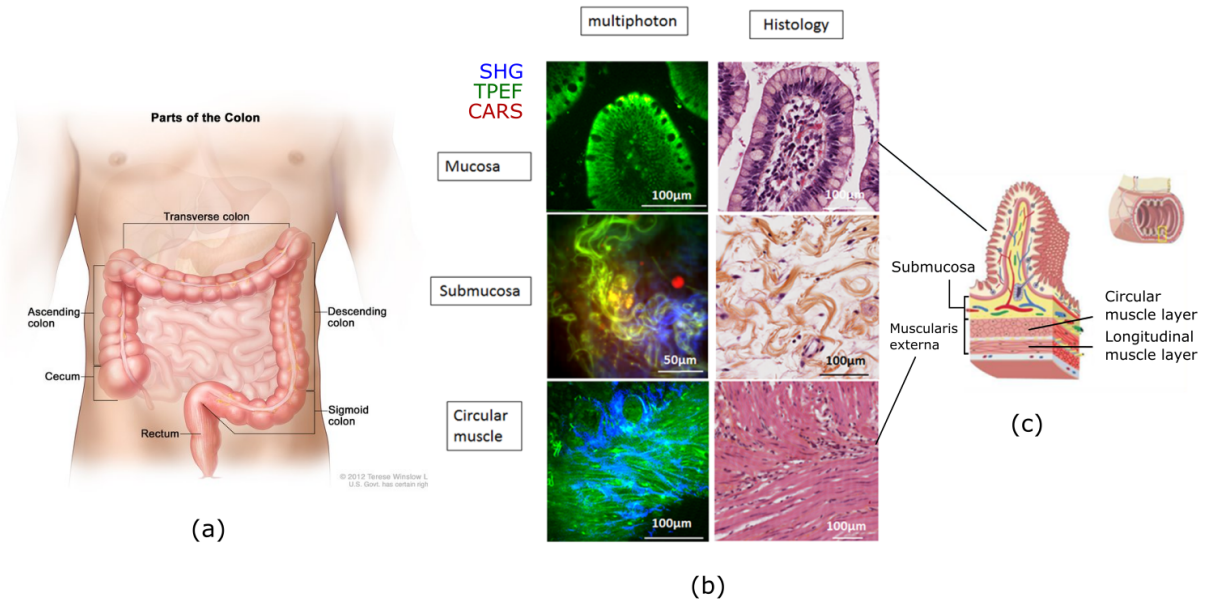

Figure 5.17: (a) Colon is the last part of the gastrointestinal tract. (b) Multiphoton microscopy techniques can be used to perform label-free imaging of unlabeled colon tissues and compare it with conventional H& E histological imaging. The nonlinear response reveals the morphology and molecular content of the different parts of the colon, such as the mucosa, the muscle layer or the adipose tissue (c). Image (a) was taken from *cancerquest.org*, while (b) and (c) are courtesy of Barbara Sarri (Institut Fresnel).

detected the signal in the forward direction. We excited the sample with 20 mW at 800 nm, detecting the TPEF signal between 500 nm and 600 nm, and the SHG signal at 400 nm. The signal was detected with the same PMT, so the filters had to be changed, in order to switch between different modalities.

5.6.2 CARS imaging of adipocytes

Adipocytes are cells specialized in storing fat and represent the main components of the adipose tissue. Their size is on the order of tens to a hundred micrometers. Colorectal tumors generally do not develop in the adipose tissue, but they invade it only during the last stages of the disease. For this reason, the histological information from the adipose tissue is generally not considered a relevant one for cancer detection.

However, adipocytes are suspected to play a role in the development of colon cancer. In fact, cancer cells grow in the anatomic proximity of the adipose tissue, where they find an important energy storage. Adipocytes were found to differentiate in cancer-associated adipocytes (CAA) during their interaction with cancer cells. CAA help tumor progression and growth by releasing adipokines, which stimulate adhesion and migration of cancer cells [106].

Anyhow, the abundance of lipids in the adipocytes makes them an interesting test sample for CARS imaging with our endoscope. The adipose tissue was extracted from a fresh colon tissue

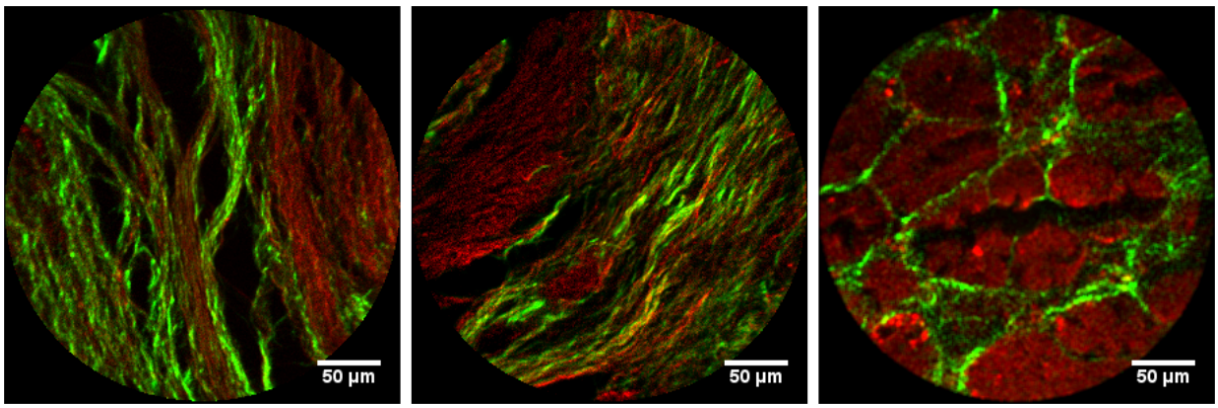

Figure 5.18: Forward detected multiphoton images of histology slides (x10 averaged frames). The abundance of collagen, imaged by SHG (green), and the fibrillar shape of the proteins emitting TPEF (red), suggests that we are imaging the muscle layer. The excitation power on the sample was P_{800}=20 mW.

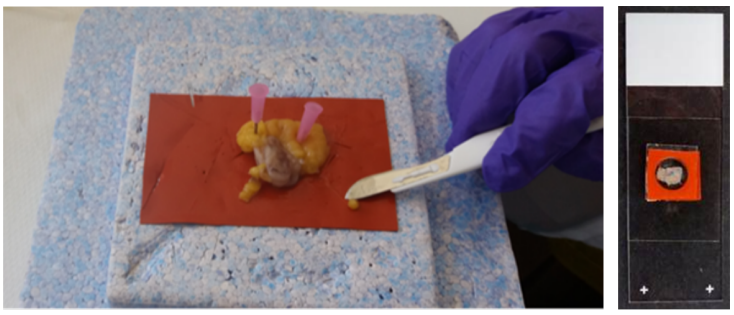

Figure 5.19: Preparation of the fresh colon tissue (a) in a microscope slide (b).

(5.19a) and sandwiched between two microscope slides (Fig. 5.19b).

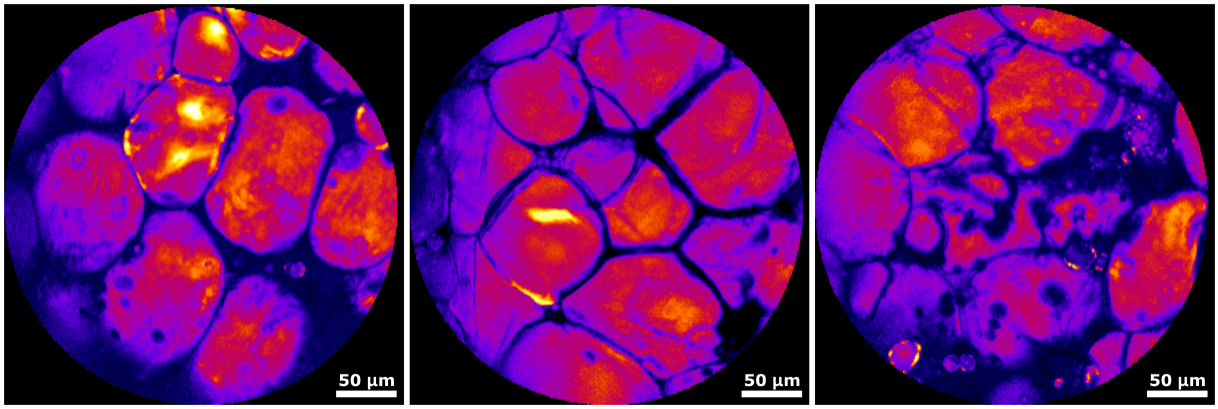

Figure 5.20: Different epi-detected CARS images of lipid cells and droplets in a fresh human colon tissue (x5 average). P_{P}=20 mW and P_{S}=10 mW were used.

We probed the CH_2 antisymmetric stretch vibration (2854 cm^{-1}) with 20 mW of the pump beam (800 nm) and 10 mW of the Stokes beam (1040 nm). Images of Fig. 5.20 were averaged over 5 acquisitions. However, the SNR is really good even in a single acquisition, as shown in Fig. 5.21.

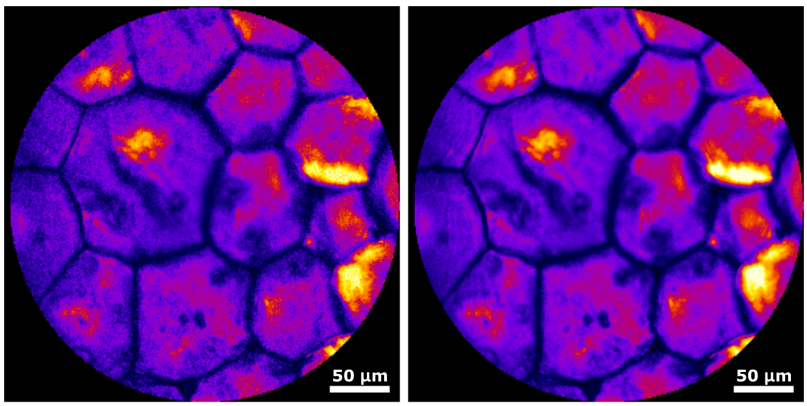

Figure 5.21: Comparison of the epi-detected CARS image of the human colon tissue for a single acquisition (a) and x5 average (b). P_{P}=20 mW and P_{S}=10 mW were used.

5.6.3 CARS and SHG imaging

We performed multimodal SHG and CARS imaging of other thick slices of colon tissue. Some of the results are shown in Fig. 5.22, 5.23 and 5.24. The much sparser density of adipocytes, together with abundance of collagen fibers might indicate either an adipose tissue with developed fibrosis or a different type of loose connective tissue.

The images were acquired with 30 mW of power onto the sample for CARS (P_{P}=20 mW and P_{S}=10 mW), and 60 mW for SHG. These images show the great potential of our miniature system to perform multimodal imaging of unlabeled biological tissues using a compact fiber delivered probe.

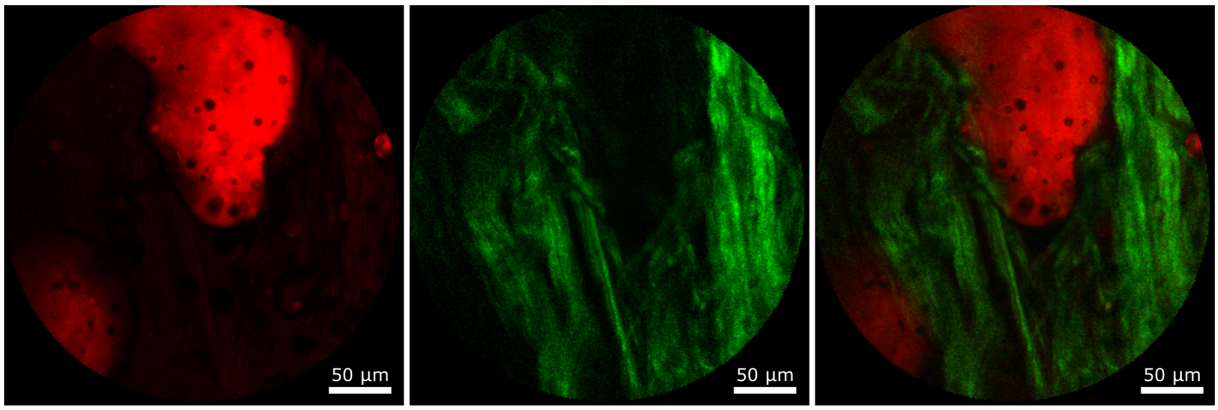

Figure 5.22: Epi-detected CARS (a) and SHG (b) images of a human colon tissue (x10 average). The two channels are combined in (c). P_{P}=20 mW and P_{S}=10 mW were used for CARS, P=60 mW for SHG.

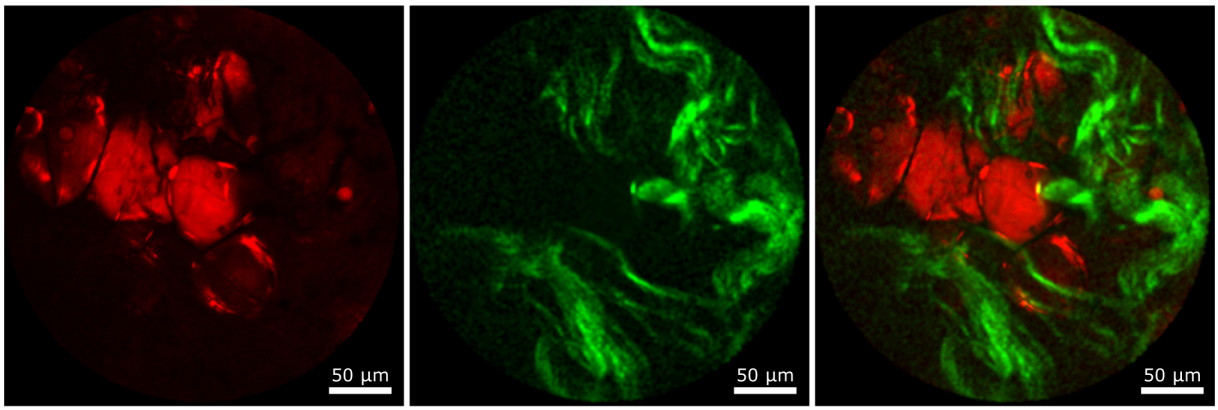

Figure 5.23: Epi-detected CARS (a) and SHG (b) images of a human colon tissue (x10 average). The two channels are combined in (c). P_{P}=20 mW and P_{S}=10 mW were used for CARS, P=60 mW for SHG.

5.6.4 Perspectives

In this section we provided a proof of principle for the application of our miniature system to multimodal endoscopy of unlabeled biological tissues. We demonstrated the capability of detecting the CARS and the SHG responses from different connective tissues. The information from different contrasts can be combined in a single image, to colocalize the different molecular

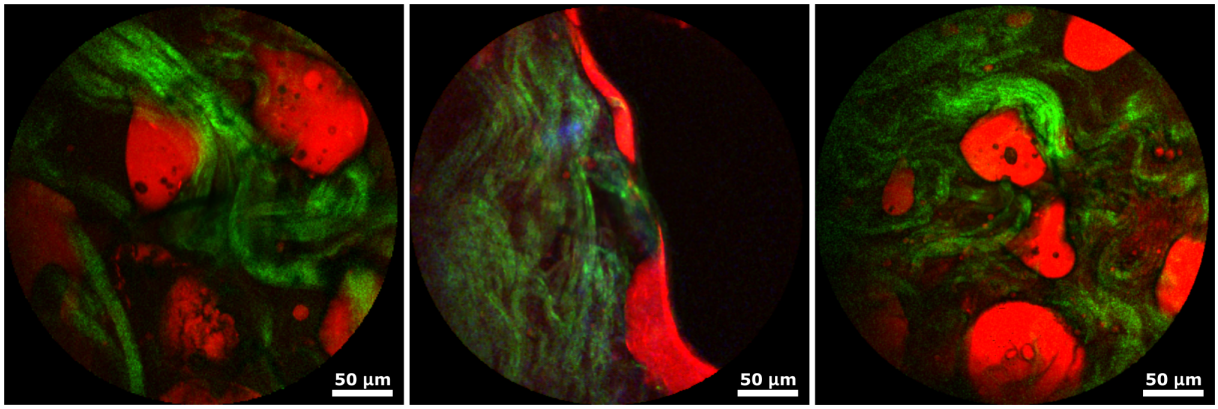

Figure 5.24: Combined epi-detected SHG (green) and CARS (red) images of different regions in a human colon tissue (x10 average). P_{P}=20 mW and P_{S}=10 mW were used for CARS, P=60 mW for SHG.

components of the tissue. Unfortunately, no two-photon autofluorescence signal was detected in endoscope modality. By increasing the sensitivity of the probe, with the strategies discussed in the next chapter, we expect to be able to perform endoscopic imaging of proteins in tissues. This would be very important to image the mucosa, which is the part of the colon where tumors develop first.

5.7 Conclusions

In this chapter we have shown that the endoscope is capable of performing multimodal nonlinear imaging. We first characterized the system using bulk optics, which served as a benchmark for the micro-lenses assembly we designed. We have seen that the miniature optics has comparable performance to the one of microscope objectives. The low chromatic aberrations enable high contrast CARS imaging. We performed label-free imaging of biological tissues, such as rat-tail tendon, and both histology slides and fresh human colon.

This is the first endoscope with a size compatible with use in clinical endoscopy, that is capable of combining CARS imaging with TPEF and SHG. In then next chapter, the efforts to develop the first portable version of the endoscope are reported.

Chapter 6

Integration in a portable probe

In this chapter, we present the integration of the system described in Ch. 4 into a portable, miniature probe. In Sec. 6.1 we describe how we sealed the micro-bead on the fiber, using a CO_2 laser splicer at IRCICA institute (Lille, France). In Sec. 6.2 we present the integrated probe and the different mechanical components. The mechanical integration of the probe was designed and carried out at XLIM institute (Limoges, France). In Sec. 6.3 we discuss the characterization and the imaging results obtained with the probe. Section 6.4 is a discussion on the possible future improvements of the probe design, in order to reduce its size and increase its sensitivity.

6.1 Micro-bead sealing on the fiber

The glass micro-bead on the Kagomé fiber is an essential component, which allows to perform high resolution imaging over large FOVs. All the images presented in Ch. 5 were obtained using a bead attached exerting a pressure on the core. The bead remained fixed on the fiber, thanks to electrostatic interactions, and resisted to the centrifugal forces experienced during the scan. For integration in a permanent probe, it is desirable to have the bead permanently fixed on the fiber core. This was made possible, using of a laser splicing system present at the IRCICA institute (Lille, France). The work on the bead sealing was conducted in Lille with Alexandre Kudlinski and Damien Labat (IRCICA).

Laser splicing

Glass is a transparent material in the visible and near IR regions. However, at longer wavelengths and in the UV region, it absorbs electromagnetic radiation. The emission wavelength of a CO_2 laser is typically 9.4 μm. In glass, it is strongly absorbed and released as heat, which can cause the material to melt. For this reason, CO_2 lasers are used to process glass materials, such as optical fibers.

The LAZERMaster LZM-100 Laser Splicing System from AFL's is a glass processing and splicing system. The LZM-100 can be used to splice or taper fibers, to create ball lenses and perform other fiber processing tasks. Using a CO_2 laser is very convenient over electrode or filament systems, that heat the fibers by creating a plasma in the air. A laser based system ensures a higher repeatability of the performances and eliminates electrode or filament instability. Moreover, as we will see, it is more adapted to seal the bead on the fiber without altering the fiber structure. The bead was sealed by melting it up to a point where it would be permanently attached to the fiber, but with the frontal spherical shape, essential for a correct focusing, still preserved. On the other hand, the fiber micro-structure was not affected.

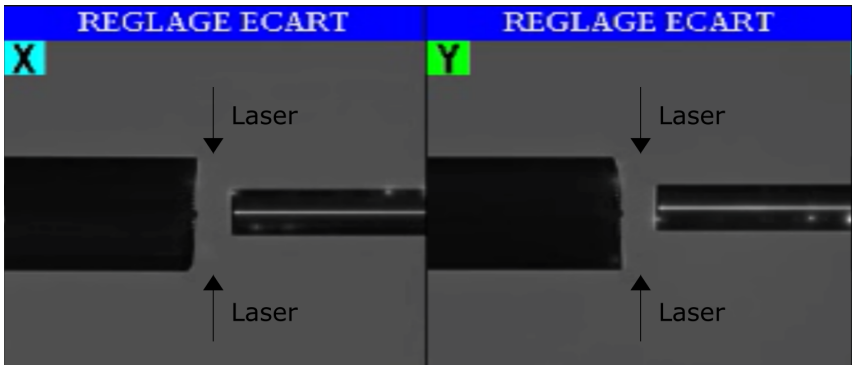

Figure 6.1: Image of the fibers during the splicing process. The cameras in the machine ensure two lateral views of the fibers during the splicing.

In Fig. 6.1, an image taken with two cameras in the LZM-100. One can notice the presence of the bead on the Kagomé fiber (on the left). On the right, an SMF which was used to add a local source of heat in front of the bead. The laser was focused over an area of 300 μm from two directions, as indicated by the arrows.

Preliminary tests

Different parameters can be controlled when using the laser splicer. We found out that the first laser discharge (generally used to clean the fibers from dust before the processing) was sufficient to melt the bead. Different parameters could be controlled, such as the distance between the Kagomé and the SMF, the laser radiation intensity or its duration. We noticed that, while the fiber structure was not affected by the laser radiation, the bead would completely melt when exposed for an excessive time. We identified a good set parameters, that caused the bead to melt without excessively deforming it. In fact, as one can see in Fig. 6.2, when the heating is too strong, it leads to an important deformation of the bead shape (Fig. 6.2b). This results in a bad focal spot profile (Fig. 6.2c).

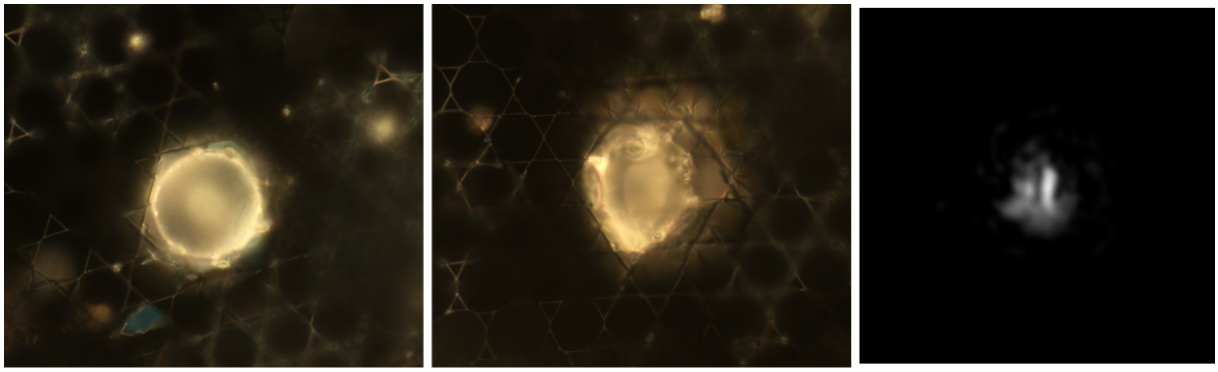

Figure 6.2: The bead on the Kagomé fiber before (a) and after the splicing (b). The exposure to an excessive radiation causes a strong deformation in the shape of the bead. The profile of the beam focused by the bead is severely affected (c).

Final result

Starting from the set of parameters, that led to the results of Fig. 6.2, we progressively reduced the intensity of radiation. The final result is shown in Fig. 6.3. In this case the bead has started melting, as one can see from Fig. 6.3b, but the focal spot produced by the bead has a symmetric Gaussian shape (Fig. 6.3c). The FWHM of this spot is 1.5 μm (data not shown), which is slightly bigger than the one before sealing (approximately 1.2 μm). We performed some mechanical tests, which confirmed that the bead was effectively sealed on the fiber. The SEM image of the

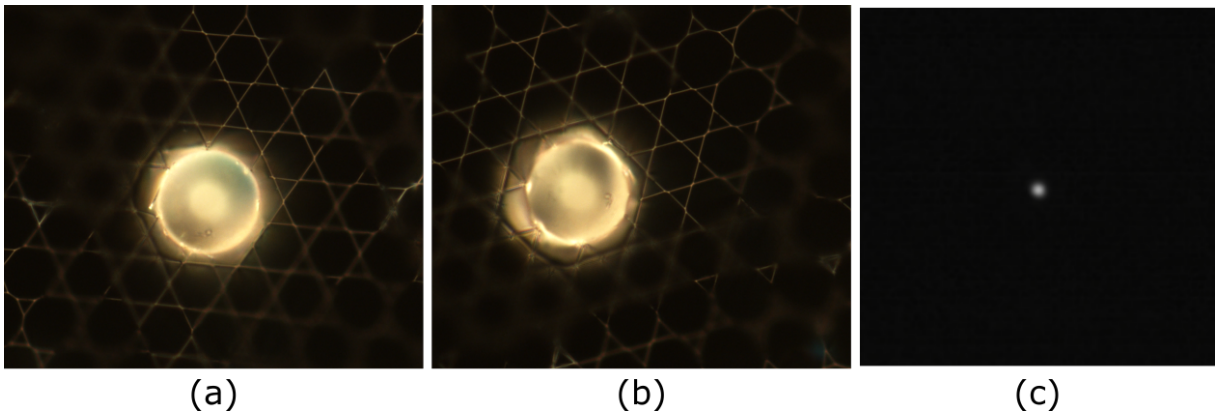

Figure 6.3: The bead on the Kagomé fiber before (a) and after the splicing (b), with the correct exposure time and intensity of the laser. The bead is slightly deformed, and is melt on the fiber, but the frontal shape is preserved. This results in a clean focal spot (c).

bead sealed on the fiber, is shown in Fig. 6.4. We can clearly see from this image that the fiber structure was not affected by the CO_2 laser, while the bead is slightly deformed on the side of the fiber. The front surface of the bead, which is important for beam focusing, has preserved a nice round shape.

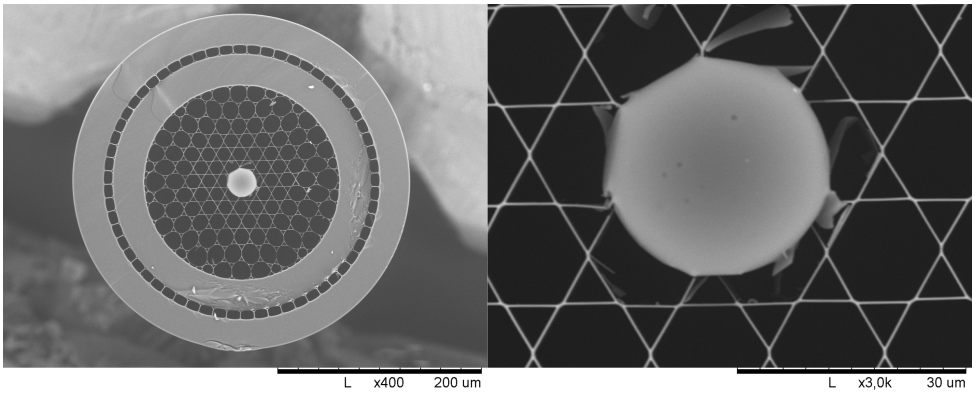

Figure 6.4: SEM images of the fiber with the glass bead after splicing.

6.2 Integration in a portable probe

The Kagomé fiber with the sealed microbead was used for integration in a portable probe. We performed this work at XLIM institute (Limoges, France) with Prof. Frederic Louradour and Marc Fabert, who designed the probe and carried out the manual integration. The design was based on the components used during the PhD for endoscopic imaging: the 3.2 mm piezo-tube, the 2 mm lenses and the Kagomé fiber. The probe design is shown in Fig. 6.5. The rigid length is

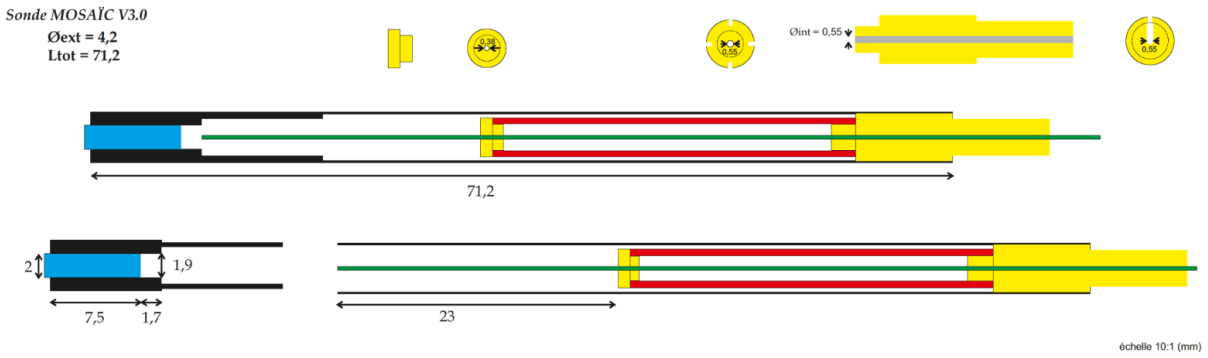

Figure 6.5: Mechanical design of the integrated probe, dimensions are indicated in mm. Courtesy of Marc Fabert (XLIM).

71.2 mm for an external diameter of 4.2 mm. This fits the size of standard colonscopes working channels (2.8-4.2 mm). However it is slightly larger than gastroscopes or enteroscopes working channels (2.0-3.8 mm) [137]. Further reduction of the probe size will be possible, since the biggest component is the piezo-electric tube and it can be purchased in smaller diameters.

The probe is encapsulated in a stainless steel, bio-compatible tube. The micro-lenses are stacked together in a detachable steel tube, which fits in the rest of the probe, but can be

removed in case of need. The front lens slightly exceeds the tube length, and some glue was applied to fix the lens on the tube. A ceramic piece, with a 380 μm hole, holds the fiber on the piezo-tube. The fiber free-standing length was set at 23 mm and glue was applied for fixation. Another ceramic piece, with a central hole of 550 μm diameter to let the fiber through, is the support for the piezo-tube inserted inside the metal tube. It was designed in such a way that the electrode wires could pass inside the support. These ceramic components were designed in XLIM and manufactured in the institute's workshop. The final hand-held probe is shown in Fig.

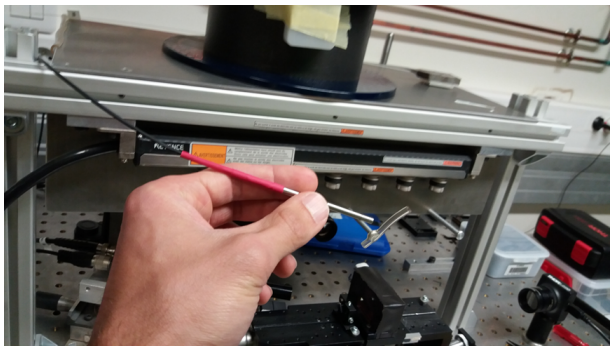

Figure 6.6: The flexible and miniature Kagomé DC probe.

6.6. The assembly of all the pieces was performed by Marc Fabert. This required a high degree of attention and care, given the non reversible nature of the procedure, and the availability of a single Kagomé fiber with micro-bead.

6.3 Characterization of the miniature probe

In this section, some preliminary results with the probe will be presented. This is an ongoing work and the probe is still under characterization. However, a few conclusions can already be drawn, together with indications for future improvements of the endoscope probe.

Unfortunately, the force exerted by the solidifying glue induced an angle on the fiber, with respect to the optical axis of the system. This angle cannot be corrected, as the elements in the probe are fixed. This misalignment has important consequences on the optical performance of the probe, as we will see in the remaining of the section.

6.3.1 Image of the focal spot

In Fig. 6.7 the focal spot of the probe is imaged on a CMOS camera. If we compare this to the beam profile of Fig. 6.3c (corresponding to the focal spot after the micro-bead) one can clearly see that aberrations are introduced in the relay from the bead to the sample. When we characterized the micro-lenses system, we saw that optical aberrations in the beam profile started to appear, as the fiber was displaced by 300-350 μm, with respect to the optical axes

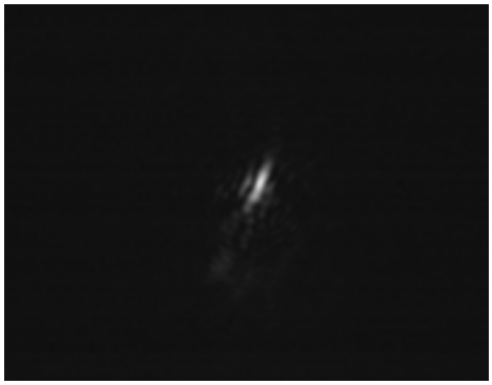

Figure 6.7: Image on the camera of the spot focused by the probe. The spot presents important aberrations, as compared to the focus generated by the bead (Fig. 6.3c).

(Fig. 4.22). This is probably the reason for the aberrated profile of the focal spot on the sample plane. Because of the angle acquired upon fixation, the tip of the fiber is not centered on the micro-lenses, which causes the aberrations of Fig. 6.7.

This is certainly an issue for linear and nonlinear imaging. It causes a degradation of the PSF and it reduces the peak intensity of the beam in the focal area. One consequence is that the nonlinear excitation efficiency is reduced and asymmetric with respect to the center of the images. Other effects take place, as we will see in the following sections, such as a stronger aplanaticity of the imaging system.

6.3.2 USAF-1951 chart

We first imaged the USAF-1951 resolution chart, to estimate the FOV of the images. The resonant frequency of the fiber is close to 580 Hz. For a scan amplitude of 11 V (lower than the maximum 15 V that we can deliver), we have a FOV of 440 μm. This means that we have an increase of the quality factor of the scanner, as compared to the system of Ch. 5.

However, from Fig. 6.9 we can see that different parts of the imaged area are not simultaneously in focus. This aberration is due to the angle between the fiber and the optical axis. In general, the fiber tip does not move on a plane during a scan, but describes a curved surface. Therefore, the axial position of the focal spot depends on the lateral position on the sample. This effect can be observed, for instance, in transmission images acquired with microscope objectives (Fig. 5.3a), where the center of the image is in focus, while elements at the periphery are slightly defocused. However, this effect is worsened, when the fiber initial position makes an angle with respect to the optical axis.

This can be seen in Fig. 6.9, where the USAF-1951 chart was imaged in different z-position on the sample plane. However, this effect was not symmetric. When the lower part of the image is in focus, the center of the image is slightly out of focus, while the upper part of the image is strongly defocused (Fig. 6.9a). However, when the upper part of the image is in focus (Fig.

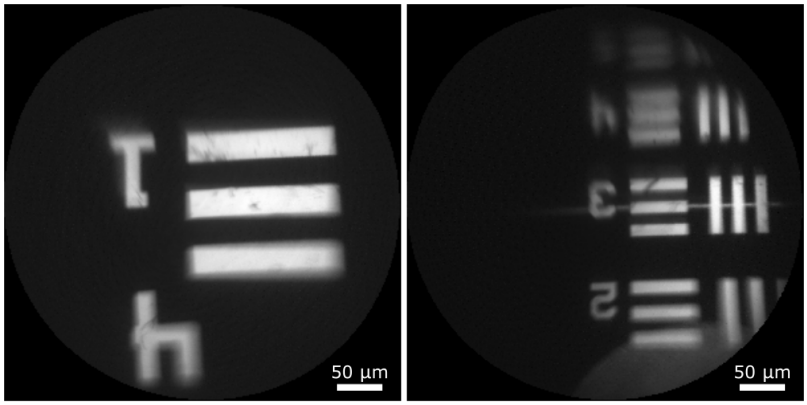

Figure 6.8: Transmission image of the USAF chart, group 4 element 1 (a) and group 5 (b). The scan amplitude was 11 V, for a FOV of 441 µm.

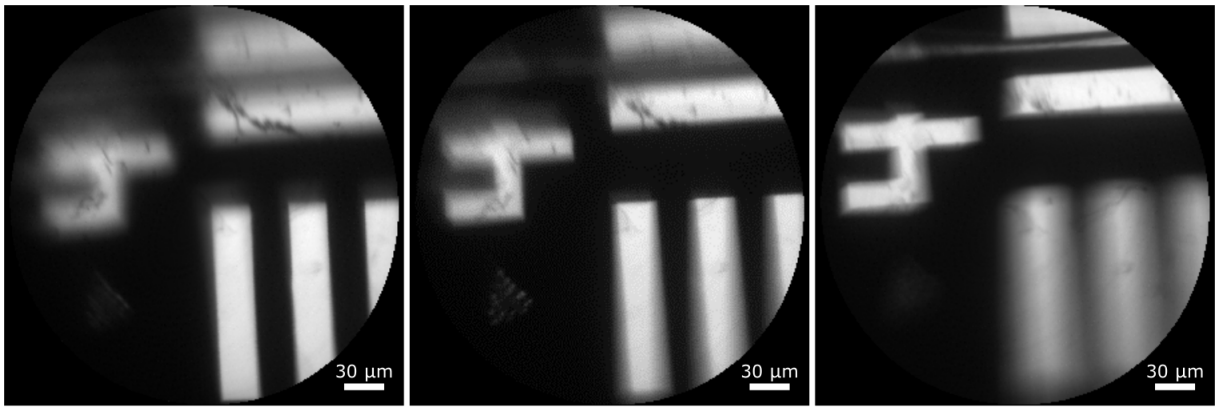

Figure 6.9: Transmission image of the USAF chart, group 4 element 2. These images illustrate the problem of the aplanaticity of the probe. Images (a), (b) and (c) are acquired while the sample was placed in different z positions. The upper part of the FOV suffers from the strongest aplanaticity. The scan amplitude was 7.5 V, for a FOV of 293 µm.

6.9c), the center of the image is clearly out of focus.

This effect can be understood using geometrical optics and simple trigonometry (see Fig. 6.10). The red line represents the fiber attached to the piezo, at different positions. The z-axis is the optical axis and the y-axis is a lateral direction. If β is the angle between the fiber and the optical axis, the projection on the optical axis $z = L \cdot \cos(\beta)$ of the fiber tip can be calculated. The lateral displacement is $y = L \cdot \sin(\beta)$, where L is the free-standing length of the fiber (23 mm in our case).

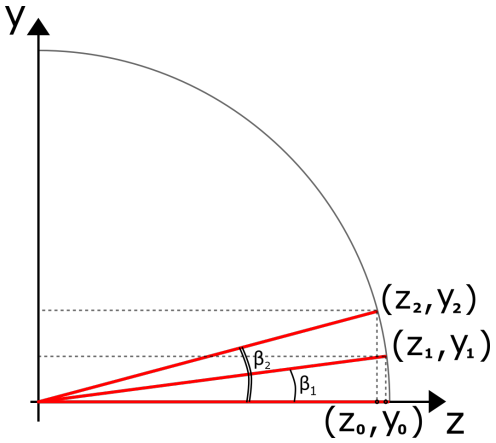

Figure 6.10: The optical fiber performs an arc during the scan. The initial position of the fiber (i.e.: its angle with respect to the optical axis) influences the magnitude of the axial translation on the sample.

One can consider a practical case, where the fiber moves in the lateral direction by $y = 250$ μm, from an initial position parallel to the optical axis ($\beta = 0$). This corresponds to a scan of 500 μm in diameter and FOV 315 μm, through the micro-lenses (M=0.63). Then $\beta = \sin^{-1}(y/L) = 6.2°$ and $z_1 = 2286$ μm. The focal spot on the sample will experience an axial displacement of $\Delta z = (z_0 - z_1) \cdot M^2 = 14$ $\mu m \cdot 0.4 = 5.6$ μm.

Let us now consider the case where the fiber is fixed with an angle, say $\beta_1 = 6.2°$. This corresponds to an initial lateral translation of 250 μm with respect to the optical axis. This might be an underestimation of the real case, if we compare the image of the spot (Fig. 6.7) with the aberrations as a function of the fiber position (Fig. 4.22). It can be calculated that, during the scan, a lateral displacement of 250 μm will make the fiber reach an angle of $\beta_2 = 12.6°$. In this case, the z-coordinate of the fiber tip will be $z_2 = 2245$ μm, which corresponds to an axial translation on the sample of $\Delta z = (z_1 - z_2) \cdot M^2 = 41$ $\mu m \cdot 0.4 = 16.4$ μm.

This simple calculation shows how the axial translation of the focal spot (Δz), and the subsequent defocusing effect, are highly dependent on the initial position of the fiber and the direction of the scan. In fact, when the fiber scan starts from an uncentered position, the value of Δz will be smaller as the fiber moves in the direction of the optical axis. This explains why the center of the image in Fig. 6.9 is less blurred when the lower part of the image is in focus (a), while it gets worse when the upper part of the image is in focus (c). Moreover, this effect is

more pronounced for a larger initial angle β.

A strategy to reduce the probe sensitivity with the initial angle and reduce the aberrations, would consist in reducing the fiber free-standing length L, as will be discussed in Sec. 6.4.

6.3.3 CARS imaging

In this section we will show the results in CARS imaging using the portable probe. From the spot profile (Fig. 6.7), we expect a decrease in the excitation efficiency. Moreover, since the aberrations increase as we scan the tip far from the optical axis, we expect to have an asymmetric imaging FOV. Figure 6.11b shows the CARS image obtained from a uniform olive oil sample. It

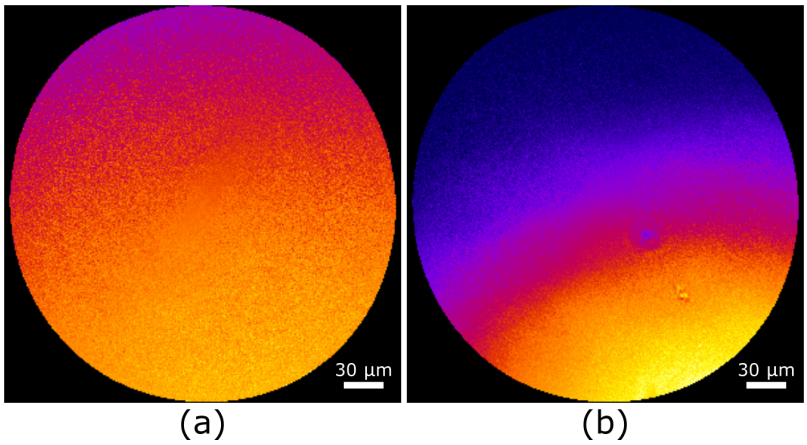

Figure 6.11: Epi-detected TPEF (a) and CARS (b) signal from FITC and olive oil, respectively.

is clear that the signal level drops on one side of the image, while it decreases on the other side. We have already estimated, from the transmission images, that the lower part of the image corresponds to the scan position where the fiber is close to the optical axis. The signal drops as the focused beam is more affected by aberrations, which are reduced when fiber tip moves closer to the center of the lenses. The signal inhomogeneity seems more pronounced in the CARS image than in the TPEF image. This might be due to both the 3rd power dependence of the CARS signal on the excitation power (against the 2nd order of TPEF), and to possible off-axis chromatic aberrations.

Fig. 6.12 shows forward detected images of $30\ \mu\mathrm{m}$ polystyrene beads. Higher excitation power ($P_\mathrm{P} = 6\ \mathrm{mW}$ and $P_\mathrm{S} = 3\ \mathrm{mW}$) were required, in order to reach the signal levels of the reference images (Fig. 5.14, where $P_\mathrm{P} = 0.8\ \mathrm{mW}$ and $P_\mathrm{S} = 0.5\ \mathrm{mW}$). This indicates that the activation of CARS signal is deeply affected by aberrations.

Moreover, similarly to linear imaging, we observed an aplanaticity problem. One can see (Fig. 6.12a) that the beads in the lower part and central part of the image are both efficiently excited. However the beads in the upper part of the image give much lower signal in both images, included Fig. 6.12b, even when they are brought closer to the focus. The background

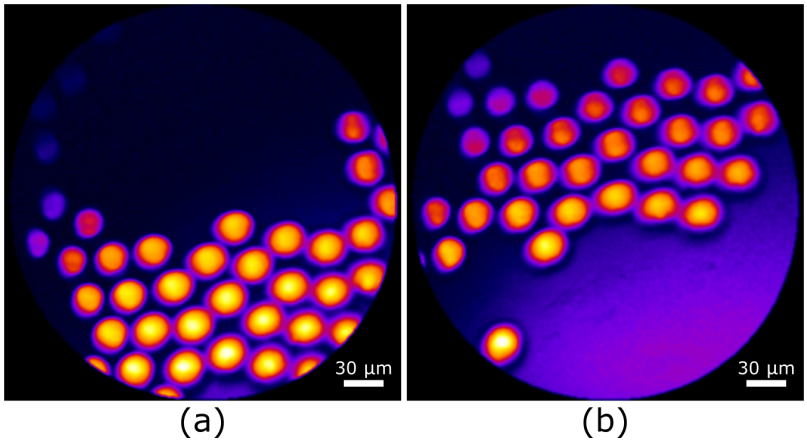

Figure 6.12: Forward detected CARS images of 30 µm polystyrene beads.

in the lower part of the image is probably due to the FWM generated on the glass coverslip.

Using the probe we were able to image lipid cells in the adipose tissue. 60 mW were used to

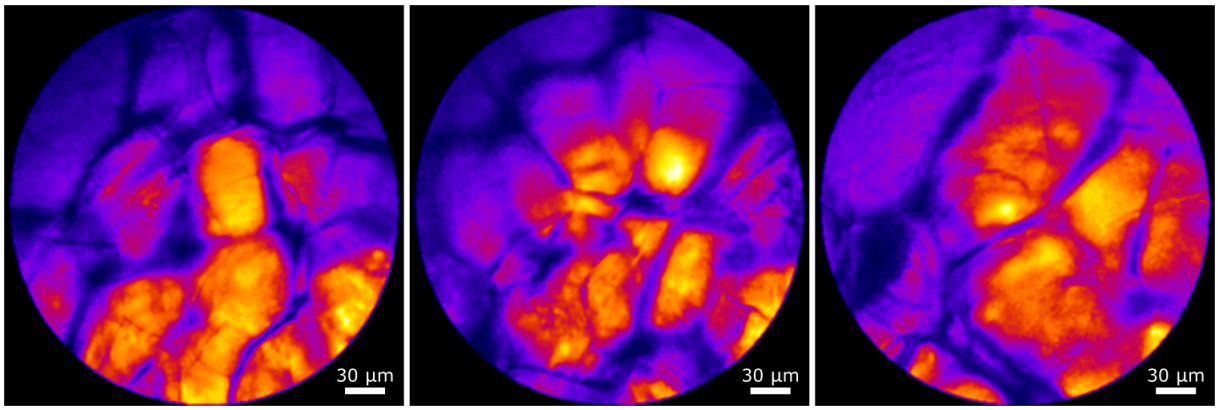

Figure 6.13: Epi-detected CARS images of lipid cells in the adipose tissue (x10 average).

excite the sample ($P_{\mathrm{P}} = 40$ mW and $P_{\mathrm{S}} = 20$ mW). This is twice the power we used for images in Fig. 5.20. The quality of the image is also degraded, but this might be due both to a lower SNR and a degradation of the sample used. Nevertheless, we can still clearly distinguish the different lipid cells and droplets.

6.4 Outlook on future improvements

In this chapter we introduced a first portable version of the probe, which was manufactured at the end of the PhD. We are still in the process of characterizing the probe in details, but some improvements for future versions can be already envisioned. These include both a reduction of the probe size and the optical aberrations, as well as an increase in both the frame rate and the imaging sensitivity.

The following improvements will be considered for the next version of the endoscope probe:

- Further **reduction of the probe size**. This is possible using a smaller piezo-tube. Custom designs are available on demand from Physik Instrumente (PI), with diameters that can as small as 2 mm, or even below. This will allow us to reduce the overall size of the probe.

- Reduce **optical aberrations**. We have seen in this chapter that the initial angle of the fiber, acquired upon fixation, had important consequences on the probe performance. While it is difficult to control the fiber behavior when glue is applied, a simple way to make the probe less sensitive to the angle consists in reducing the free-standing length of the fiber L. This will reduce, for a same angle, the displacement with respect to the center of the lenses (Δy), which is responsible for the aberrations in the focal spot. Moreover, it will reduce the distortions caused by the axial translation (Δz) of the spot on the sample plane over a scan, since this is proportional to L.

- Increase the **imaging frame rate**. There are different ways we can improve the imaging frame rate:

  On the one hand, the resonant frequency of the fiber can be increased with a shorter fiber length. In general, the ratio between the resonant frequency f_{RES} and the imaging frequency has to be high enough, to avoid incorrect sampling of the image. This happens when the distance between the arcs of the spiral is too large. A general condition on the scan period T_{exp} is given by: $f_{\mathrm{RES}} \cdot T_{\mathrm{exp}} = N_{\mathrm{pixels}}$, where N_{pixels} is the number of pixels in the image. A higher $\mathrm{f_{RES}}$ allows to reduce the duration of the scan pattern.

  We can also work on the active breaking of the fiber, during retrace. In the work we described, imaging was performed during a driven expanding spiral pattern, where the scan amplitude was increased up to a maximum value. This was followed by a rest period (0.5 s), with the voltage set to zero and the oscillations naturally contracting until the fiber stopped. The duration of this rest period can be reduced to few tens of millisecond, by active breaking of the fiber's oscillations. This would allow to further increase the imaging rate.

- Faster imaging will require a higher sensitivity of the probe. A **new fiber design** could significantly improve the collection efficiency. The experiment on the spatial distribution of the signal collected by the fiber (presented in Sec. 4.4.2), suggested that the photonic structure surrounding the core doesn't actively participate in the signal collection and transmission. Reducing the size of this structure in a future fiber design should be possible, and we expect it to enhance the signal collection, increasing the probe sensitivity.
  Moreover, our system is highly dependent on the scattering of light from tissues. When scattering does not occur, signal is mostly collected from the core. The losses in the core are quite important in the wavelength range of the nonlinear signals. Enhancing the fiber

transmission in the 500 nm - 700 nm wavelength range, would certainly be beneficial in terms of sensitivity.

6.5 Conclusions

We have described, in this chapter, the main components necessary to integrate the system of Ch. 5 in a portable probe. The various steps are somehow tricky, and require precise machines (like the laser splicer), experience and care. However they are all, starting from the sealing of bead, reproducible. The first version of the probe is not optimal, but this prototype was certainly useful to understand where future improvements can be made.

Chapter 7

Fiber delivery for SRS microscopy and endoscopy

We dedicate this last chapter to the study of fiber pulse delivery for Stimulated Raman Scattering (SRS) applications. This is the result of a collaboration with APE GmbH (Berlin, Germany) for the delivery of 2 picoseconds pulses in a SRS micro-spectroscopy setup, using Kagome hollow-core fibers. The results described hereafter have a strong importance for the implementation of SRS imaging in the Kagome fiber-based endoscope developed during this thesis work. Indeed, we find out that a parasitic signal is generated in the fiber, whose origin lies in the interplay between nonlinear effects and frequency dependent fiber losses.

In Sec. 7.1, we describe the basic principles of SRS microscopy. In Sec. 7.2, we show how the XPM-induced frequency shift can induce a change in the power transmitted by a fiber, when this has a highly frequency dependent loss spectrum. Section 7.3 is dedicated to the numerical simulations, by means of the split-step Fourier method, of pulse propagation in the Kagome's hollow-core. We evaluate the effect of XPM-induced spectral changes, on the total transmitted power, for different shapes of the loss spectrum. The experimental setup, including the lock-in detection scheme, for the measurement of the signal generated in Kagome fibers, is described in Sec. 7.4. The experimental results are discussed in Sec. 7.5 and compared to the numerical simulations.

7.1 SRS microscopy

SRS microscopy is performed with two synchronized trains of laser pulses at frequencies ω_{P} and ω_{S} ($\omega_{\mathrm{P}} > \omega_{\mathrm{S}}$) that are focused on the sample. The frequency difference $\omega_{\mathrm{P}} - \omega_{\mathrm{S}}$ is tuned so that it matches the resonant frequency Ω_R of a molecular vibration. A molecule in the vibrational ground state $|f\rangle$ is excited to the vibrational level $|v\rangle$ and a Stokes photon is emitted (Fig. 7.1a). On a macroscopic scale, this process leads to the coherent oscillation of molecular vibrations

and the pump beam is depleted (SRL) while the Stokes beam experiences a gain (SRG) (Fig. 7.1b). In SRS microscopy the pump and Stokes beams are focused and scanned over the sample,

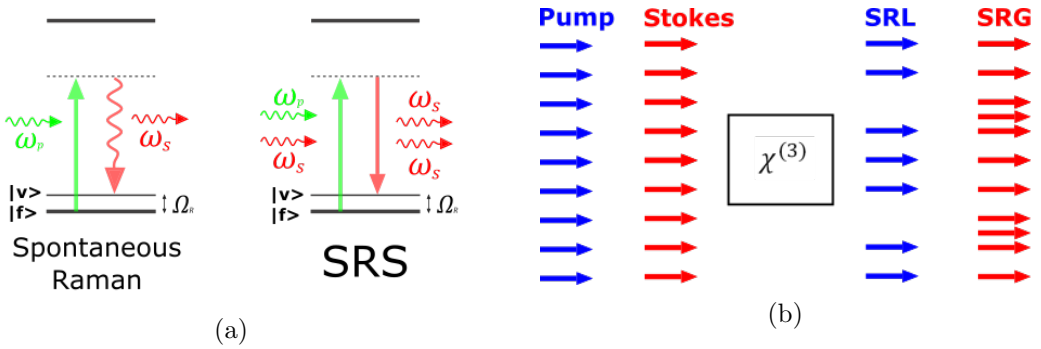

Figure 7.1: (a) Spontaneous Raman and Stimulated Raman Scattering energy diagrams and (b) field depletion due to SRS.

the intensity variation in one of the two beams is measured (ΔI_{P} for SRL detection). For bio-compatible power levels, and because the pump-Stokes beams interaction is restricted to few microns when performing tight focus microscopy, the magnitude of this change is small compared to the beam intensity ($\Delta I_{\mathrm{P}}/I_{\mathrm{P}} < 10^{-3}$) [16]. Therefore a modulation scheme has to be employed to extract the SRS contribution from the total signal.

In the SRL configuration, the Stokes intensity is modulated at a frequency f using an electro-optical (EOM) or acousto-optical modulator (AOM). The pump beam is unmodulated and detected with a photo-diode after interaction with the Stokes beam on the sample. The signal from the photo-diode is sent to a lock-in amplifier, where the frequency component f of the signal is amplified. This corresponds to the SRL contribution to the total signal. By choosing a modulation frequency $f > 1$ MHz, the lock-in amplifier filters out the laser average intensity (zero-frequency component) and any intensity oscillation occurring at frequencies lower than f. In fact, laser noise occurs primarily at low frequencies (up to hundreds of kHz), and decreases at high frequencies with a $1/f$ dependence (reference here). As f enters the MHz region, the laser noise figure can reach the shot noise limit associated with the Poisson distribution of photon counts (Fig. 7.2). A high-modulation (> 1 MHz) frequency cancels out laser noise, together with the low-frequency intensity changes due to variations in transmittance of the sample, for example.
However, it was found that a residual background exists at high frequencies f when performing SRS microscopy. This is caused by a mixture of thermal effects [92], Kerr nonlinearities [123] and two-photon two-colors absorption [45], phenomena that can generate a signal at the frequency f. A three-beam, opposite-phase modulation scheme to remove these artifacts was shown to increase the imaging sensitivity of an SRS microscope [10].

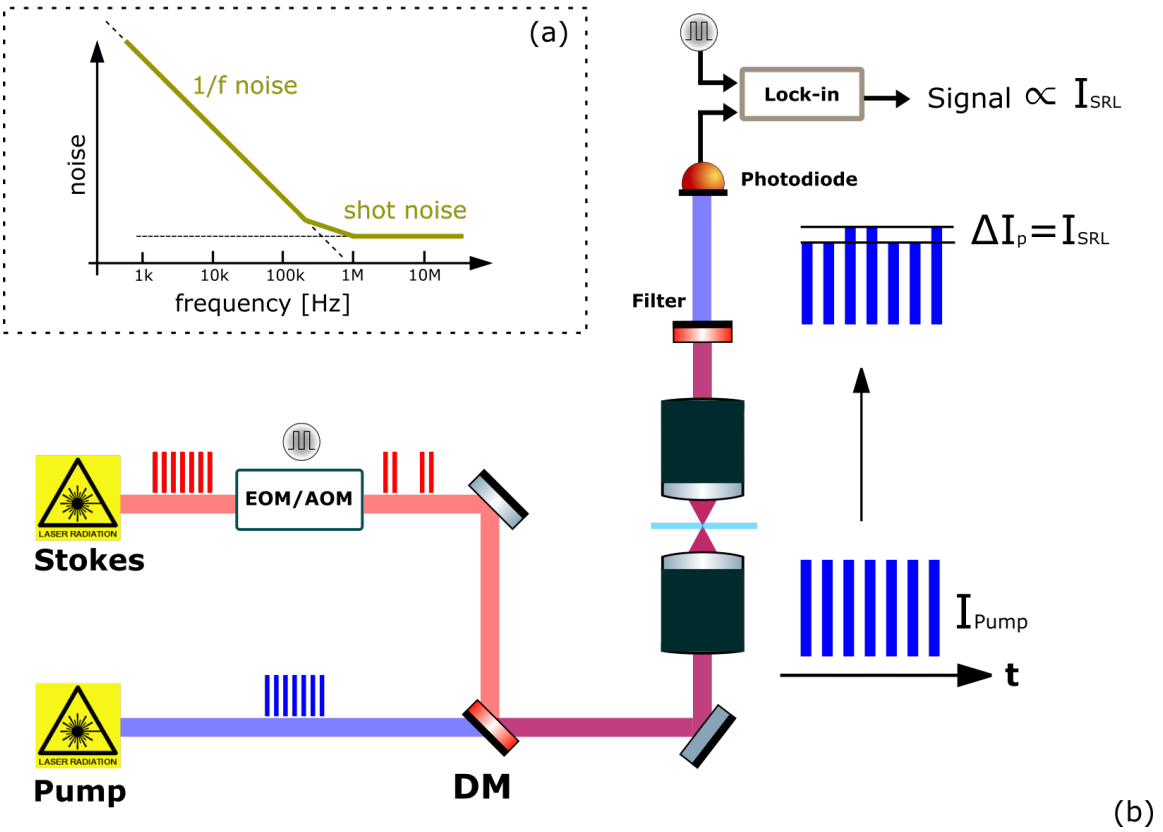

Figure 7.2: (a) Typical noise spectrum of a laser source and (b) operation principle of an SRS microscope.

7.2 Modulation transfer via XPM

In Sec. 2.5 we described the process of XPM, occurring whenever two fields propagate in the same medium. XPM changes the spectra of the pulses, through a nonlinear phase shift term. In the lock-in amplification scheme used for SRS, what we detect is an intensity change in one of the two beams. The loss (SRL) in the pump energy is due to the presence of the Stokes beam, that transfers its high-frequency modulation to the other beam. XPM does not involve any energy transfer between the two fields, but it can induce a transfer of modulation from the Stokes to the pump beam, through the frequency-dependent loss spectrum of the Kagome fiber. In other words, the spectral features of the pulses are affected by XPM, but the total energy of each pulse is conserved. However if the pulses propagate in a lossy medium, such as an optical fiber, the energy after propagation will depend on the losses. Now, if the fiber losses are frequency dependent, the total transmitted energy will depend on the pulse spectrum. If the transmitted pump power changes with the presence of the Stokes beam, through XPM and fiber losses, then the pump beam exiting the fiber will carry a modulation at the same frequency f of the Stokes field. This modulation will be detected in the lock-in amplification scheme.

7.2.1 XPM induced frequency shift

We shall start by an estimation of the frequency shift occurring in the Kagome fiber because of XPM. The fiber we used for the experiment was produced in IRCICA (Lille). It has an hexagonal core shape, the diameter of the internal circle being $17.5\ \mu\mathrm{m}$ and that of the external circle being $20.6\ \mu\mathrm{m}$ (Fig. 7.3). The core propagation mode can be fitted with a Gaussian distribution, whose radius is $w{=}\ 0.849 \cdot \mathrm{FWHM} = 8.4\ \mu\mathrm{m}$ (defined as the distance from the peak to the $1/e^2$ intensity point) The effective area for a Gaussian beam is then calculated as:

$$A_{\mathrm{eff}} = \pi w^2 \approx 220\ \mu m^2$$

from which we can estimate the non linear coefficient γ of the Kagome fiber. Assuming that the nonlinear refractive for the propagating field is that of air, $\mathrm{n_2} = 3 \cdot 10^{-23}\ \mathrm{m^2/W}$ (see [136] and [55]), we have:

$$\gamma = \frac{2 \cdot \pi \cdot n_2}{\lambda \cdot A_{\mathrm{eff}}} \approx 1.07 \cdot 10^{-6}\,(W \cdot m)^{-1}$$

The fiber has a low GVD, which means that the pulses interact along the whole fiber length $\mathrm{L_W} > 1\ \mathrm{m}$. Then the nonlinear phase accumulated over 1 m of propagation in the Kagome fiber can be estimated with Eq. (2.18):

$$d\phi = \gamma \cdot P_0 \cdot L = 6.7 \cdot 10^{-4}$$

where the peak power of the pulse P_0 is derived from the average power, through the repetition rate (80 MHz) and the pulse duration ($\mathrm{T}_0 = 2$ ps) of the laser, as

$$P_0 = \frac{P_{\mathrm{avg}}}{f_{\mathrm{rep}} \cdot T_0} = 625\,W \tag{7.1}$$

for an average power $P_{\mathrm{avg}} = 100$ mW. Then the frequency shift imposed on the pump spectrum can be calculated using Eq. (2.30):

$$d\nu = d\omega/2\pi = \frac{d\phi}{T_0 \cdot \pi} \approx 1.07 \cdot 10^8 Hz$$

Which corresponds to a wavelength shift

$$d\lambda = 2.3 \cdot 10^{-3}\mathrm{nm}$$

For a pulse centered at $\lambda = 800$ nm pulse.

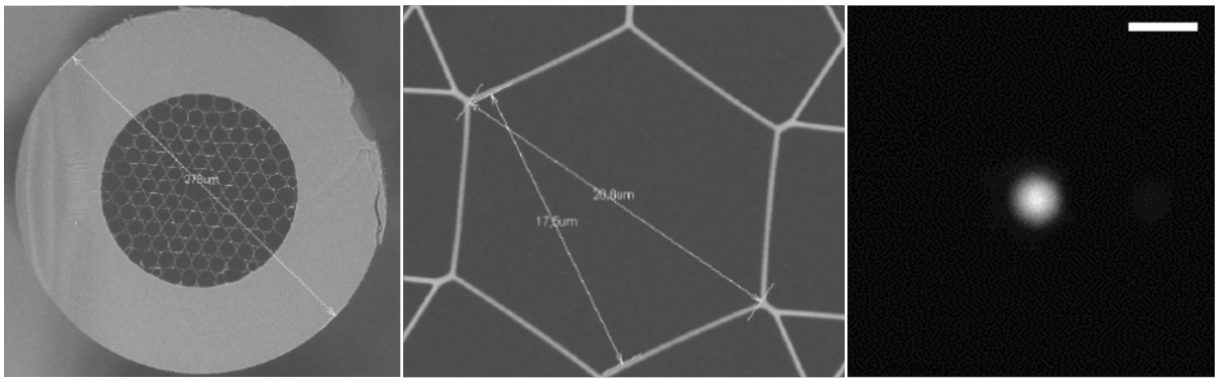

Figure 7.3: SEM image of the Kagome T1675E fiber (a), detail on the fiber's core (b). Fiber core's mode at 800 nm (c), scale bar is 10 micron.

7.2.2 Kagome loss spectrum

The loss spectrum of a fiber defines the attenuation of the beam intensity due to propagation, thus not taking into account injection losses. It is typically defined in units of decibel per unit length (dB/m) or (dB/km). A ratio expressed as decibels is given:

$$\left(\frac{P_1}{P_2}\right)_{\mathrm{dB}} = 10 \cdot \log_{10}\left(\frac{P_1}{P_2}\right) \tag{7.2}$$

Therefore the absolute ratio between two powers is:

$$\left(\frac{P_1}{P_2}\right) = 10^{\left[\left(\frac{P_1}{P_2}\right)_{\mathrm{dB}}\right]/10} \tag{7.3}$$

As an example, we consider a beam propagating in a fiber who has a loss of $3\ \mathrm{dB/m}$ at that wavelength. This means that after one meter of propagation the beam power P is:

$$\frac{P_{\mathrm{in}}}{P} = 10^{0.3} = 1.995 \approx 2$$

where P_{in} is the initial power.
The attenuation in a fiber is measured as the ratio in the output optical power for two different fiber lengths. Repetition of this measurement over a broad wavelength range gives the loss spectrum of the optical fiber. Figure 7.4 shows the loss spectrum of the Kagome fiber, which

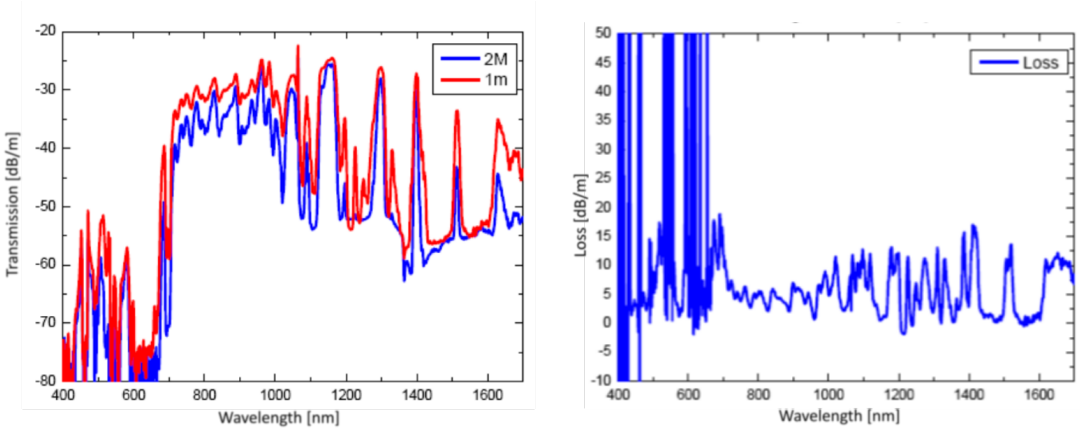

Figure 7.4: Loss spectrum of the Kagome fiber.

a non-flat structure with both long range oscillations together with some finer structures. The local slope of the loss spectrum reaches easily $0.1 - 0.3\ \mathrm{dB/nm}$.

7.2.3 XPM induced modulation transfer

The two previous sections contain the elements to estimate the loss/gain in transmitted pump power due to the presence of the Stokes beam. Using Eq. (2.30) we calculated the maximum XPM-induced frequency shift to be $\mathrm{d}\lambda \approx 2.3 \cdot 10^{-3}\ \mathrm{nm}$ for a $100\ \mathrm{mW}$ Stokes beam.
Let us now consider the case of the pump spectrum being in a spectral region where the loss is a linear function of the wavelength, with a positive slope of 0.2 $\mathrm{dB/nm}$. Then the presence of the Stokes beam will cause a spectral shift that leads to a loss (gain) on the pump beam transmitted power, depending on the direction of the shift. The magnitude of this modulation is

easily estimated:

$$0.2\frac{\mathrm{dB}}{\mathrm{nm}} \cdot 2.3 \cdot 10^{-3}\ \mathrm{nm} = 4.6 \cdot 10^{-4}\ \mathrm{dB}.$$

Therefore the power modulation M induced by the coupling between nonlinear effects and the fiber loss spectrum can be as high as:

$$M = 1 - \frac{P_{\mathrm{XPM}}}{P_{\mathrm{noXPM}}} = 1 - 10^{4.6 \cdot 10^{-4}/10} = 1.06 \cdot 10^{-4}$$

This intensity variations occur at the high frequency f of the Stokes beam modulation, and are detected by the lock-in amplifier (described in Sec. 7.1).

To summarize, in this section we showed that even when no energy transfer between beams is involved, the spectral shift induced by XPM coupled with fiber losses can generate a signal at the modulation frequency f. From a practical point of view, this signal will constitute a background in fiber delivered SRS microscopy and endoscopy and it is of primary importance.

7.3 Simulation of nonlinear pulse propagation

In order to simulate propagation in the Kagome's hollow-core, and estimate the XPM-induced modulation transfer, we will we use the split-step Fourier method, which was described in Sec. 2.6. We will first describe the field parameters, used to simulate propagation of a pump and Stokes beam in the fiber, in conditions as close as possible to the experimental ones. Then we will discuss the results obtained from the simulations.

7.3.1 Definition of the field

We describe the field as being composed by a Gaussian pulse (pump) and an hyperbolic secant pulse (Stokes): as we will see later, this corresponds to the experimental situation. We shift the spectrum so that it is centered on the pump central frequency, which leads to the following form for input field:

$$E_{\mathrm{t}} = {E_{\mathrm{P}}}^{0} \cdot e^{(-2{,}77 \cdot t^2/{\tau_{\mathrm{P}}}^2) + i\delta t^2} + {E_{\mathrm{S}}}^{0} \cdot \mathrm{sech}^2(t/\tau_{\mathrm{S}}) \cdot e^{[i \cdot 2\pi \cdot (\nu_{\mathrm{P}} - \nu_{\mathrm{S}}) \cdot (t - t_{in})]} \tag{7.4}$$

where τ_{P}=1800 fs is the FWHM of the Gaussian pulse, and $\tau_{\mathrm{S}} \approx 1.76^{-1} \cdot \mathrm{FWHM_S}$, with $\mathrm{FWHM_S}$ $= 2\ \mathrm{ps}$. The initial time delay between pulses is set with the parameter t_{in}. The frequencies ν_{P} and ν_{S} are the frequencies of the pump and Stokes beam, found from the respective wavelengths $800\ \mathrm{nm}$ and $1031\ \mathrm{nm}$ using $\nu = c/\lambda$ ($\mathrm{c} = 3 \cdot 10^8\ \mathrm{m/s}$ is the speed of light). The discretization of the time axis is 3 fs while in the frequency domain it is $0.3\ \mathrm{cm}^{-1}$. The field propagates in 1 meter of fiber, which is divided in 200 steps over which the effect of dispersion and nonlinearities are computed. The parameter δ is an initial chirp term on the Gaussian pulse, that is used to match

the time-spectral duration of the simulated pulse with the one used for experiment (7.7). The Kagome dispersion is negative and low, for which we impose a value of $\beta_2 = -3000\ \mathrm{fs}^2/\mathrm{m}$. This value was chosen after comparison between the simulated and experimental zero-modulation points, whose delay position depends on the group velocity mismatch between the pulses. Like in Sec. 7.2, the nonlinear index is of air is taken as $\mathrm{n}_2 = 3 \cdot 10^{-23}\ \mathrm{m}^2/\mathrm{W}$, which gives a nonlinear coefficient of $\gamma = 1.07 \cdot 10^{-6}\ (\mathrm{W} \cdot \mathrm{m})^{-1}$ for a field with effective area $\mathrm{A}_{\mathrm{eff}} = 220\ \mu\mathrm{m}^2$. Precise

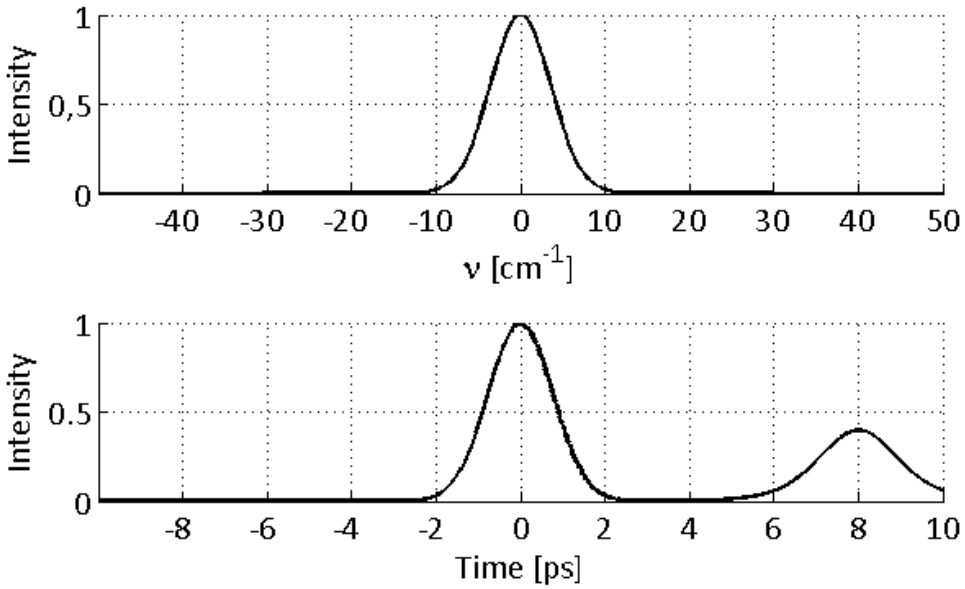

Figure 7.5: The input field in the frequency (top) and time domain (bottom), for the case of pulses with initial delay of 8 ps. The range on the frequency axis contains only the pump pulse.

modeling of propagation in the fiber would require the computation of the exact mode in the Kagome with a Finite Element Method (FEM) calculation [111, 93], to take into account the exact beam shape and the portion of field that is coupled in the glass structure. Here, we will simulate the case where a Gaussian beam, having the size of the field in the Kagome core, is propagating in air. In a work from 2004 [93], the comparison of computational and experimental results on soliton propagation in a HC-PBG fiber, drew the authors to the conclusion that the glass structure surrounding the core is contributing to the nonlinear index. If such is the case, the nonlinear spectral broadening would be even more important than the one we compute here.

7.3.2 Results of the simulations

XPM induces a modulation through the frequency dependent losses of the fiber. Such losses are computed at the end of propagation, where $S(\nu)$ and $S_{\mathrm{loss}}(\nu)$ are the input and exit spectra

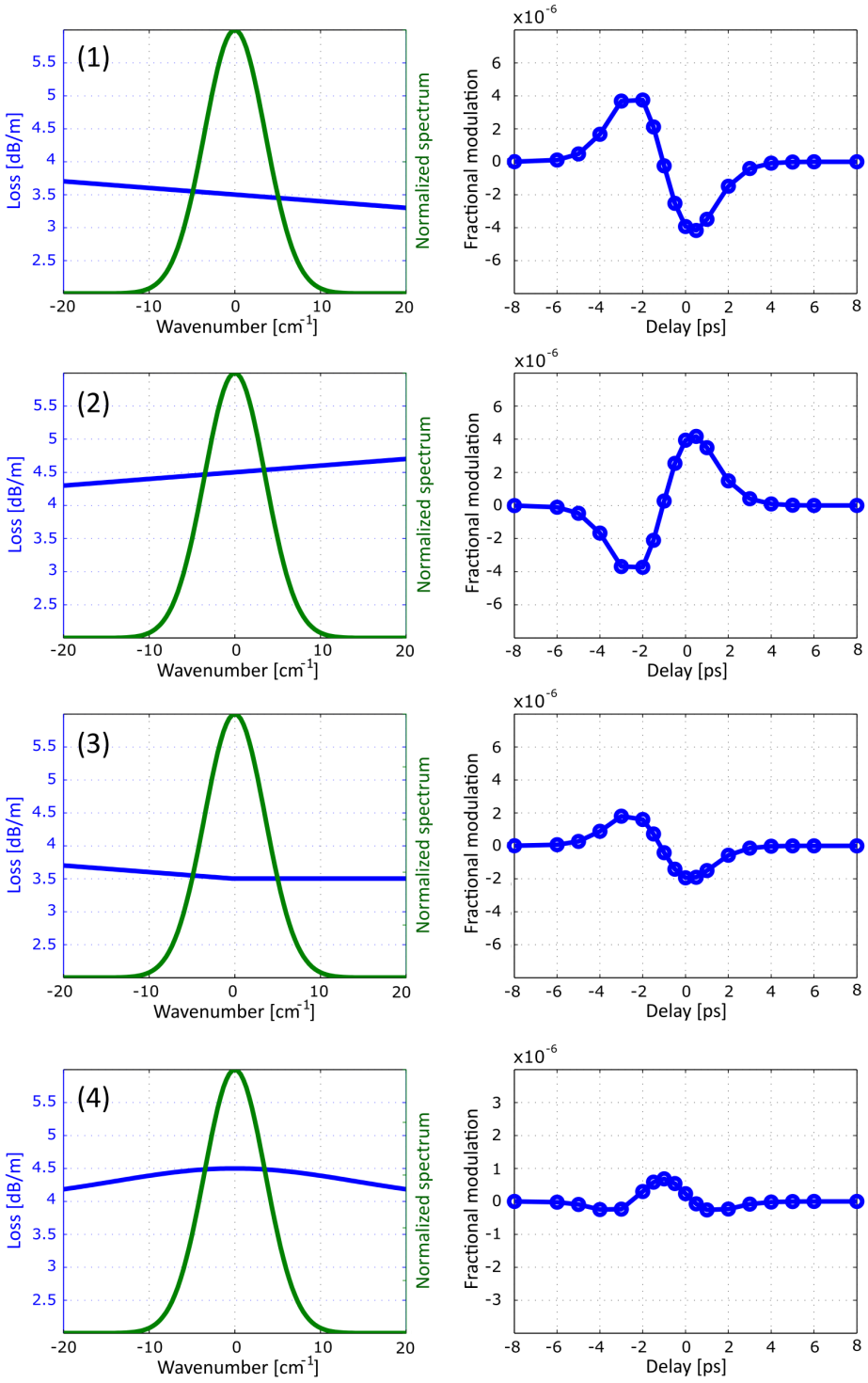

Figure 7.6: Fractional modulation obtained by the simulations as a function of the pulses' initial delay, for different loss spectrum profiles. From top to bottom: negative and positive linear curves (0.3 db/nm), negative linear until $\nu = 0$ then flat, Gaussian centered on pump spectrum. Negative time delays mean that the 1031 nm beam is leading in the fiber.

of the pump beam propagating within the fiber. This is done by accounting for spectral losses $\mathrm{loss}_{\mathrm{dB}}(\nu)$ as:

$$S_{\mathrm{loss}}(\nu) = S(\nu)/10^{(\mathrm{loss}_{\mathrm{dB}}(\nu)/10)} \tag{7.5}$$

The spectrum is then integrated over the pump pulse bandwidth, in order to find its total energy $P_{\mathrm{out}}^{\mathrm{pump}}$ after propagation. The modulation induced by XPM is then found as the difference between $P_{\mathrm{out}}^{\mathrm{pump}}$ in the SPM case (only pump pulse in the fiber) and the XPM case (with the Stokes pulse).

We show here a simulation of the fractional modulation induced by XPM as a function of the relative delay between pulses, for different fiber loss spectrum shapes (Fig. 7.12). Negative time delays mean that the $1031\ \mathrm{nm}$ beam is leading in the fiber, while positive time delays have the $800\ \mathrm{nm}$ beam leading. Therefore, negative time delays correspond to an XPM-induced blue-shift in the $800\ \mathrm{nm}$ spectrum. The delay-dependence of the modulation is due to the XPM asymmetric spectral broadening (see Fig. 2.3). In fact, the transmitted energy changes when we take into account the fiber losses, leading to dispersive-like line shapes in certain cases. These include the cases of a linear profile with slope $\approx 0.3\ \mathrm{dB/nm}$. The modulation curve as a function of the delay is reversed when the slope changes sign. The modulations are on the order of 10^{-6} and have a local maximum and one minimum when the frequency shift is maximized. For linear loss curves we could expect no total energy change when the spectral broadening is perfectly symmetric. This point lies somewhere near $-1\ \mathrm{ps}$, because of the group velocity mismatch between the two pulses in the fiber. When the loss spectrum is flat on one side, we still have a positive, then negative modulation as a function of the delay.

We consider also the case in which the pump beam is centered on a local maximum of the loss spectrum, described by a Gaussian loss profile concave downward. In this case any broadening is expected to lead to a gain in the total transmitted energy. The curve of the modulation vs delay shows a global maximum, centered at the delay point giving maximum broadening, follow by two local minima corresponding to negative modulation (loss). This might be due to an interplay of SPM and XPM effects. Simulations were also performed in the case of a flat transmission spectrum, giving rise to very small modulations, on the order of 10^{-15} (data not shown).

7.4 Experimental setup

We performed the experiment with the picoEmerald system (APE GmbH) for SRS spectroscopy and microscopy. This system provides a user-friendly, software controlled and an all-in-a-box platform for SRS experiments, removing the complexity often associated with the development of such setups. The excitation beams are spatially overlapped at the laser output. The delay control and high frequency beam modulation ($f = 20\ \mathrm{MHz}$) both happen inside the laser box

and can be controlled by the software.
The picoEmerald delivers two synchronized pulsed trains of 2 ps pulse duration and $80\ \mathrm{MHz}$ repetition rate. This pulse duration is a good compromise between high peak power and good vibrational resolution ($\Delta\nu < 10\ \mathrm{cm}^{-1}$). The Stokes beam ($1030\ \mathrm{nm}$), generated by a fiber laser,

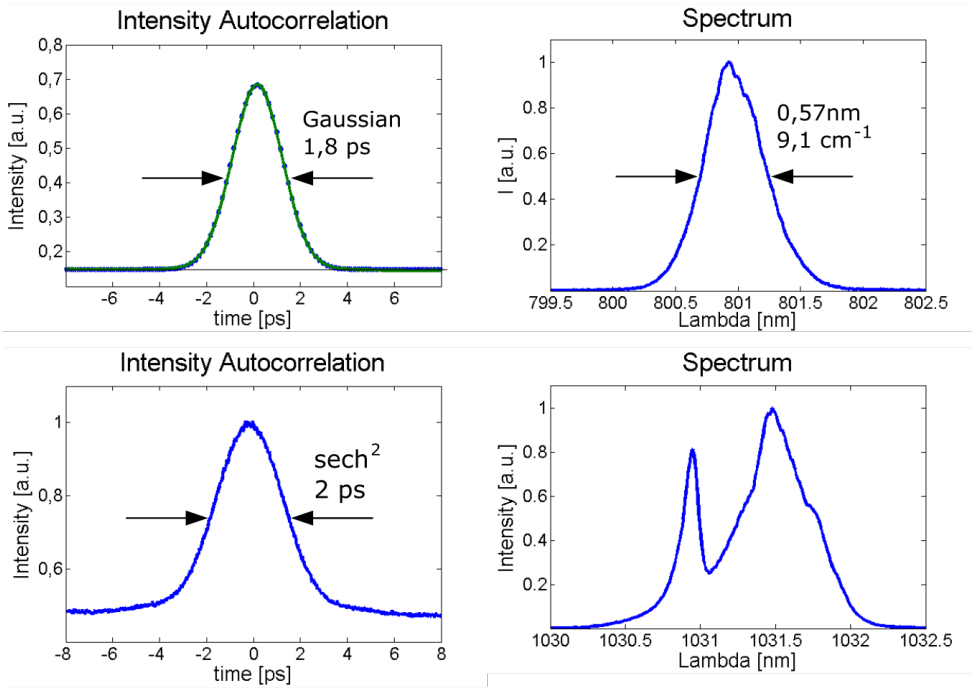

Figure 7.7: Intensity autocorrelation and spectrum of the pump beam at 800 nm (top row) and of the Stokes beam (bottom row).

is frequency doubled and used to pump the OPO, which delivers the tunable pump beam. The OPO acts as a low-pass filter for laser noise, which can be strong for fiber lasers, ensuring that the pump beam is shot noise limited at high frequencies. Inside the laser box an electro-optical modulator (EOM) synchronized with the laser can be activated, providing a modulation at $1/4$ the repetition rate. When the phase of the EOM is properly adjusted, the Stokes beam consists of two pulses "on" and two pulses "off" (Fig. 7.8). A mechanical delay line on the Stokes beam allows for precise control of the beams temporal overlap. The beams generated are spatially overlapped at the picoEmerald exit: the alignment can be controlled, with the aid of a TPA[1] sensitive detector, or manually by acting on two mirrors that are placed inside the box. For coupling inside the fiber we first align the pump and then optimize the Stokes coupled power by aid of the two mirrors. In order to control the temporal overlap at the fiber output, we use a cross-correlator (*pulseCheck USB*, APE GmbH).

[1]Two-photon absorption.

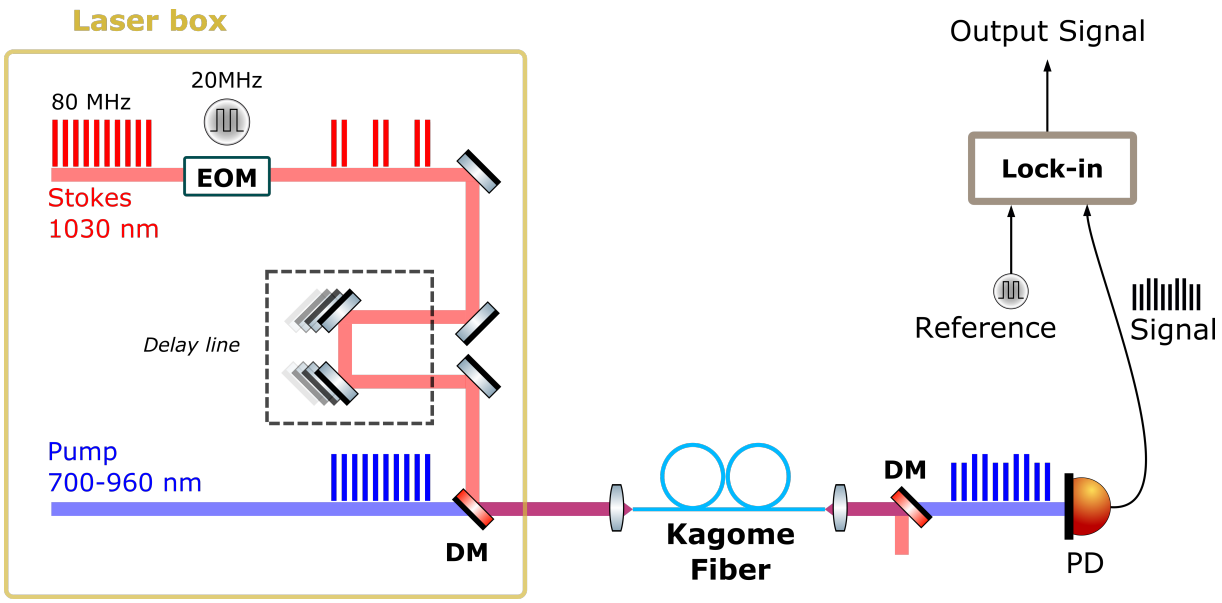

Figure 7.8: Experimental setup for the measurement of XPM signal generated in the Kagome hollow-core fiber.

7.4.1 Lock-in detection

After propagation in 1 m of Kagome fiber, the Stokes beam is filtered using two laser line filters centered at 1030 nm. The pump beam is enlarged with a negative lens to overfill the detector's sensitive area. The detection at the EOM modulation frequency (20 MHz) in the pump beam is done by the APE Lock-in Amplifier (LIA), an integrated module for detection and locked-in amplification. Developed for fast-imaging applications, the detector allows for very short integration times (100 ns to 20 µs). During these experiments we will use an integration time of 20 µs, which gives the highest SNR. The waveform that modulates the Stokes beam is sent to the lock-in amplifier, which extracts the signal at that frequency. The output of the lock-in amplifier consists of an amplitude and a phase. The phase is very important because it defines whether the intensity variation of the pump beam is a loss or a gain. In order to adjust the phase to the right value we let a very small portion of the modulated Stokes beam (≈ 1 µW) on the detector, and adjust the phase in order to maximize the positive signal. This synchronizes the phase of the lock-in to the beam modulation.

The lock-in output consists of a signal that can go up more than 1 V. Special care has to be taken for this high values because saturation of the detector might be approaching. In such a case the post-amplification (postAmp) of the detector and the gain might be reduced.

From the output signal, we can retrieve the fractional modulation in the pump beam using the equation:

$$\Delta I_{\mathrm{P}}/I_{\mathrm{P}} = \frac{Signal_{\mathrm{LIA}}}{K \cdot P_{\mathrm{det}}} \tag{7.6}$$

where $K = 500\ \mathrm{mV/\mu W} = 5 \cdot 10^5\ \mathrm{mV/mW}$ is a constant of the LIA, valid in conditions of maximum gain ($43.5\ \mathrm{dB}$) and post amplification on. It defines the output signal in mV per $\mu\mathrm{W}$ (or mW) of modulation. P_{det} is the pump power incident on the detector, and should be kept lower than $50\ \mathrm{mW}$ to avoid saturation.

7.5 Experimental results

Using the setup shown in Fig. 7.8 we measured the modulation induced by co-propagation of the beams in the Kagome fiber. The output signal was read and noted together with the pump power incident on the detector, which allowed us to retrieve the fractional modulation through Eq. (7.6). Whenever the lock-in signal would go to saturation and gain had to be reduced, we measured a scaling factor between the signal at maximum gain and post-amp ON (where Eq. (7.6) holds) and the signal at lower gain. This allowed us to estimate the fractional modulation for different gain levels.

7.5.1 Spectral scan

We first performed a wavelength scan over the vibrational spectrum spanning from $1200\ \mathrm{cm^{-1}}$ to $3100\ \mathrm{cm^{-1}}$. For this we used the tunable OPO pump beam. We adjusted the delay between the two beams in order to keep them overlapped at the fiber output, which was checked with the cross-correlator. The output Stokes average power was $40\ \mathrm{mW}$, which has to be multiplied by a factor 2 when calculating the peak power, in order to account for the modulation at $20\ \mathrm{MHz}$.

The fractional modulation measured for wavelengths from $780\ \mathrm{nm}$ to $920\ \mathrm{nm}$ is shown in Fig. 7.9. The logarithmic graph shows that the absolute modulations are on the order of 10^{-6} or less, except for two points at $\Omega = 1550\ \mathrm{cm^{-1}}$ and $\Omega = 2330\ \mathrm{cm^{-1}}$. These are the vibrational energies of oxygen and nitrogen [87], which are two most abundant molecular species in air. This suggests that the modulation is caused by the excitation of molecular vibrations in $\mathrm{O_2}$ and $\mathrm{N_2}$, which causes a depletion in the pump beam through SRS. This is consistent with the negative sign of the modulation, whose magnitude is on the order of 10^{-4} (Fig. 7.10). Gas-filled hollow-core fibers have been widely employed in recent years for Stimulated Raman Scattering, because they allow for high beam confinement (few microns) over long interaction lengths (the fiber length) [8]. This reduces the threshold powers for stimulated Raman conversion, so the detection of an SRS signal from $\mathrm{O_2}$ and $\mathrm{N_2}$ at atmospheric pressure comes with little surprise.
The output pump power at the fiber exit was found to be highly wavelength dependent, from an initial value of $116\ \mathrm{mW}$ at $780\ \mathrm{nm}$, to a minimum of $71\ \mathrm{mW}$ at $905\ \mathrm{nm}$ and a maximum of $250\ \mathrm{mW}$ at $888\ \mathrm{nm}$. We indirectly measured it for each wavelength, by measuring the power of the light reflected by the neutral density filter in front of the detector. This would give us the incident power on the detector as well, in order to keep it lower than $50\ \mathrm{mW}$ and to

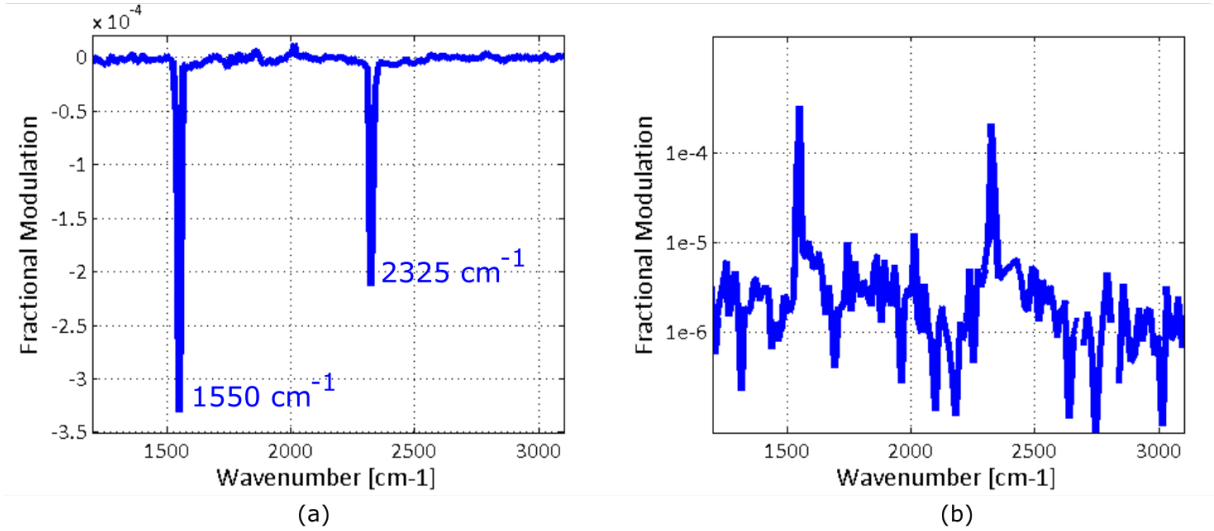

Figure 7.9: Fractional modulation in the air filled Kagome fiber, reflecting the SRS signal from oxygen and nitrogen (left) and absolute fractional modulational in log scale to highlight the orders of magnitude (right).

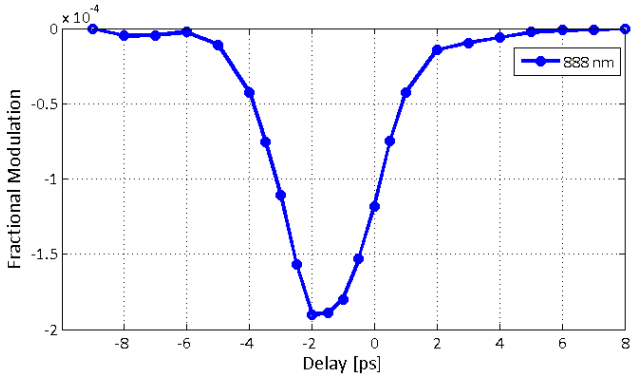

Figure 7.10: Modulation as a function of the delay at the SRS resonance of O_2 (1550 cm^{-1}).

use its value to calculate the fractional modulation. The output pump power from 780 nm to 815 nm is shown in Fig. 7.11. This power changes might be due both to the fiber loss spectrum

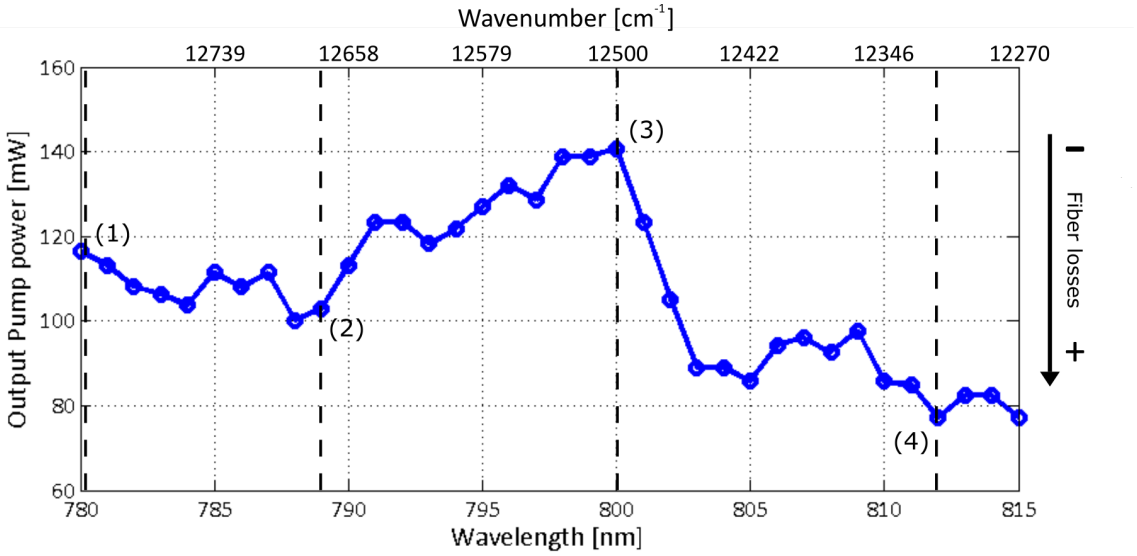

Figure 7.11: Transmitted power of the pump beam from the Kagome fiber as a function of the wavelength. Dashed lines indicate the four wavelengths where a measurement of the modulation vs delay has been performed (see Fig. 7.12)

and to fiber coupling effects. However, knowing the pointing stability of the laser pump beam (< 100 µrad / 100 nm), we rule out any change in the coupling conditions and attribute this pump transmission power dependency to fiber losses only.

7.5.2 Non-resonant modulation

When the wavelength difference between the pump and Stokes beams is not matching the vibrational resonances of O_2 and N_2, we still detect a modulation in the pump beam on the order of 10^{-6} (Fig. 7.9), which is consistent with the results from the simulations. The shape of the modulation, as a function of the delay between the pulses is shown in Fig. 7.12. In three cases, the modulations follow the dispersive-like shapes that we saw occurring in simulations when the loss spectrum had a positive-only (or negative-only) gradient. The sign is reversed for the pump beam at 789 nm. The modulation at 811 nm has a positive-only shape, with a peak at the same position where the SRS signal from O_2 was maximized (Fig. 7.10). This is probably the delay position where the interaction between pulses is maximized. The origin of the shape might be due to a local maximum in the loss spectrum, which causes any broadening (red or blue-shift) to result in a positive modulation (analogous to the simulation results in Fig. 7.6d).

It is interesting to analyze the results illustrated in Fig. 7.12 in sight of the transmitted power levels of Fig. 7.11. Indeed we see that for point (1), 780 nm the spectral losses increase (transmitted power decrease) for lower frequencies (higher λ). This corresponds to the simulation

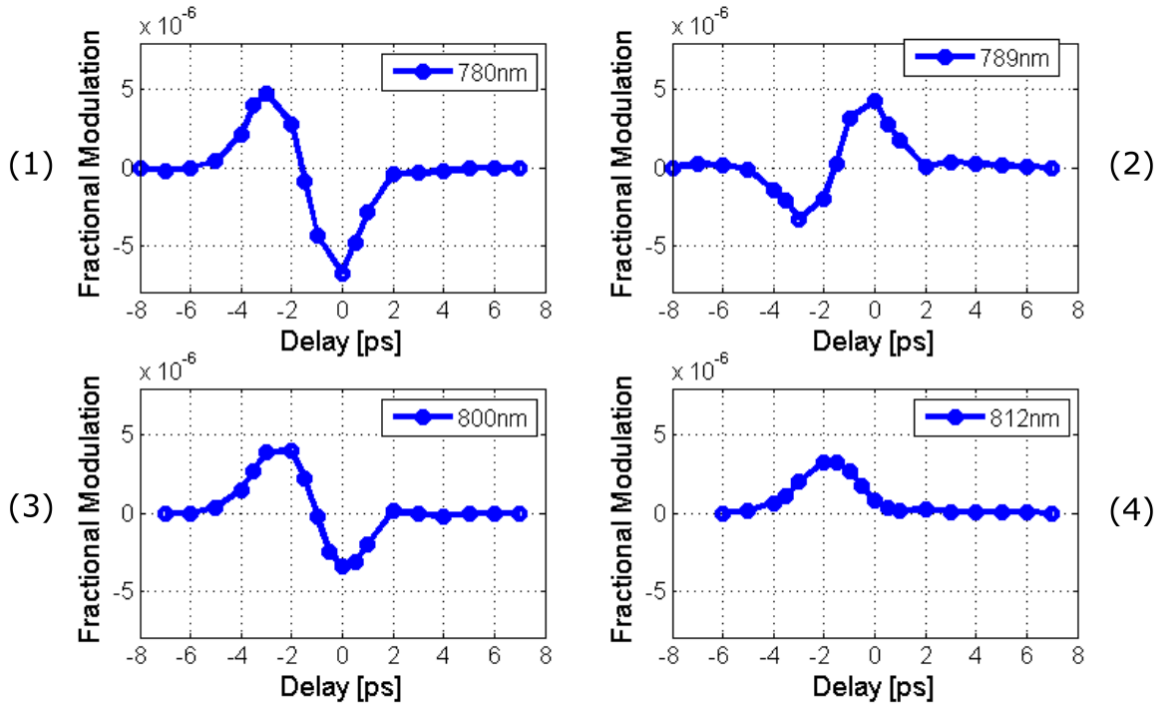

Figure 7.12: Detected signal as a function of the two delay between pulses. The time convention is the same as for simulations: negative time delay means that the 1031 nm is leading in the fiber. See Fig. 7.11 for the spectral loss profile associated with each curve (1)-(4).

of Fig. 7.6b. The same situation holds at $800\ \mathrm{nm}$ (point (3)), where the pump output power decreases at $801\ \mathrm{nm}$, while it is more flat at $799\ \mathrm{nm}$. This situation resembles the case of Fig. 7.6c. Regarding point (2), we see that at higher frequencies ($788\ \mathrm{nm}$) the losses are higher, while they decrease for lower frequencies ($790\ \mathrm{nm}$). This situation is the one of Fig. 7.6a.
We can see that in points (1)-(3) the shape of the curve follows the one predicted by simulations, if we take into account the spectral losses given by Fig. 7.11.
Regarding point (4), the transmitted pump power is in a local maximum of the loss spectrum. The measured curve has a positive peak and doesn't take on negative values, which, on the other hand, appear in the simulations (Fig. 7.6d). Apart from this discrepancy, the shape of the curves seem in agreement with each other.

It is important to point out again that, if SRS between the pump and Stokes beam would take place, the detected signal would have negative sign only, like for the O_2 resonance (where the pump is depleted by SRS, see Fig. 7.10). So these modulations must originate from some other effect. We think that this is indeed an XPM-induced modulation transfer, mediated by the frequency-dependent loss spectrum of the Kagome fiber.

7.6 Conclusions and perspectives

In the present chapter we have studied the problem of the transfer of modulation from pump to Stokes beam occuring in Kagome HC fibers. Picosecond pulses provide the spectral resolution necessary for spectroscopic analysis. Spectral resolution can be obtained with femtosecond pulses by means of a technique such as spectral focusing [57]. However, the study of the background-generating effects, occurring with picosecond pulses, is a necessary step in sight of Kagome based SRS endoscopy.

We have carried out numerical simulations and experiments, that indicate that the frequency dependent losses of the fiber are responsible for an induced modulation. While not being a proper SRS signal, this can be interpreted as such when performing SRS measurements after a HC fiber, since it carries the high-frequency modulation f of the Stokes beam. Some strategies can be envisioned for background reduction. One could rely on the use of top-hat shaped pulses (see for example [4]). In such pulses, the central part of the pulse temporal profile is flat. A zero intensity gradient means would generate no spectral broadening, for most of the pulse energy.
Another approach could be similar to the SRGold principle [10], which is based on two beams to counterbalance the spurious effects inducing transfer of modulation. In such a case, one could think of using the idler beam as a mirror pulse to the pump, with respect to the Stokes pulse position: when the pump is leading, the idler would be trailing. In this case, the pump negative intensity gradient seen by the Stokes, and the relative nonlinear phase shift, would be counterbalanced by the positive gradient of the idler pulse. Such a scheme would require two independent delay controls on the pump and Stokes, and a sufficiently broad and well-placed

(centered on the $1030\ \mathrm{nm}$) transmission window from the Kagome.

The order of magnitude of the background from the Kagome is 10^{-6}, with typical modulation values in SRS microscopy and spectroscopy being on the order of $10^{-5} - 10^{-6}$. We do not expect it to reduce the sensitivity of the system, if the laser noise figure is at shot-noise at $20\ \mathrm{MHz}$. This background can be subtracted from the total signal. However, being wavelength dependent, it will require a pre-calibration when doing spectroscopy.

Conclusions and Perspectives

In this thesis we have proposed a new approach to the problem of pulse delivery for nonlinear endoscopy. The use of hollow core fibers had been previously explored, but only to a limited extent, because of certain drawbacks of photonic bandgap (PBG) fibers. These include a limited spectral transmission window and a very steep group velocity dispersion curve. The Kagomé fiber design, used in this thesis, overcomes the limitations of PBG fibers for pulse transmission. It allows the delivery of ultrashort pulses (100 fs) with minimal distortion over a broad transmission window. This removes the necessity for more or less complicated pre-compensation mechanisms and offers great spectral flexibility in excitation. Moreover, it is not affected by the overwhelming FWM background that is generated in solid-core fibers, the main obstacle to CARS endoscopy so far.

Using a Kagomé double clad fiber, designed and produced in IRCICA (Lille, France), we developed a compact and miniature system for multimodal endoscopic imaging. Tight focusing at the Kagomé exit was made possible thanks to the inclusion of a silica micro-bead into the fiber core. The device, based on the resonant scan of the fiber tip with a piezo-electric tube, can achieve large FOVs ($> 300\ \mu\mathrm{m}$), with low driving voltages ($\pm 15\ \mathrm{V}$) and sub-micrometer spatial resolution. A miniature lens assembly, composed of commercially available micro-lenses (2 mm diameter), was developed to focus the excitation beams on the sample with low chromatic aberrations.

This device is capable of activating different contrasts, such as TPEF, SHG and CARS, with excitation pulse delivery and signal collection performed by the same fiber. The integration of these nonlinear contrasts in the same device was made possible by the properties of the Kagomé, and represents an important innovation in the field. It allowed us to perform label-free CARS and SHG endoscopic imaging of biological tissues ex-vivo. With possible developments in the fiber design, such as the enlargement of the transmission window, we expect to reach the necessary sensitivity to detect the TPEF emitted by endogenous fluorophores in tissues.

The integration in a miniature and portable probe was made possible by a collaboration with the XLIM institute (Limoges, France). The 4.2 mm diameter probe gathered in a portable device all the imaging elements, previously used in an open-space configuration. This first version was unfortunately affected by optical aberrations, due to an angle between the fixed fiber and the

optical axis. This affected the probe sensitivity and the overall imaging quality. However, CARS images of tissues were obtained in endoscope modality, the first time for a clinically compatible endoscope. Strategies to reduce the aberrations are being considered, for future versions of the probe. Such a sensitive, portable probe, will inevitably lead us to in-vivo imaging applications.

The last chapter was dedicated to the delivery of picosecond pulses for SRS imaging, and the investigation of the background generated in a Kagomé fiber. We have seen that a modulation transfer occurs, because of a coupling between nonlinear effects and the non-flat spectral transmission profile of the fiber. This is a wavelength dependent background, whose magnitude is on the order of the signals typically detected in SRS microscopy. However, when the laser system is at the shot noise limit, we expect this background not to be compromising in terms of SRS sensitivity. Understanding the mechanism behind the generation of this background was very important, in sight of the future implementation of SRS in the Kagomé DC imaging probe.

Bibliography

[1] Agrawal, G. P. *Nonlinear fiber optics*. Academic press, 2007.

[2] Albota, M. A., Xu, C., and Webb, W. W. Two-photon fluorescence excitation cross sections of biomolecular probes from 690 to 960 nm. *Applied optics 37*, 31 (1998), 7352–7356.

[3] Andresen, E. R., Bouwmans, G., Monneret, S., and Rigneault, H. Two-photon lensless endoscope. *Optics express 21*, 18 (2013), 20713–20721.

[4] Balčiūnas, T., Fan, G., Andriukaitis, G., Pugžlys, A., and Baltuška, A. High-power top-hat pulses from a yb master oscillator power amplifier for efficient optical parametric amplifier pumping. *Optics letters 37*, 13 (2012), 2547–2549.

[5] Balu, M., Liu, G., Chen, Z., Tromberg, B. J., and Potma, E. O. Fiber delivered probe for efficient cars imaging of tissues. *Optics express 18*, 3 (2010), 2380–2388.

[6] Bao, H., Allen, J., Pattie, R., Vance, R., and Gu, M. Fast handheld two-photon fluorescence microendoscope with a 475 μm$\times$ 475 μm field of view for in vivo imaging. *Optics letters 33*, 12 (2008), 1333–1335.

[7] Barretto, R. P., Messerschmidt, B., and Schnitzer, M. J. In vivo fluorescence imaging with high-resolution microlenses. *Nature methods 6*, 7 (2009), 511–512.

[8] Benabid, F., Knight, J. C., Antonopoulos, G., and Russell, P. S. J. Stimulated raman scattering in hydrogen-filled hollow-core photonic crystal fiber. *Science 298*, 5592 (2002), 399–402.

[9] Berto, P. *Microscopie et spectroscopie de phase. Développements en diffusion Raman cohérente (CRS) et en thermo-plasmonique.* PhD thesis, Aix-Marseille Université, 2013.

[10] Berto, P., Andresen, E. R., and Rigneault, H. Background-free stimulated raman spectroscopy and microscopy. *Phys. Rev. Lett. 112* (Feb 2014), 053905.

[11] Boyd, R. W. *Nonlinear optics*. Academic press, 2003.

[12] Brown, C. M., Rivera, D. R., Pavlova, I., Ouzounov, D. G., Williams, W. O., Mohanan, S., Webb, W. W., and Xu, C. In vivo imaging of unstained tissues using a compact and flexible multiphoton microendoscope. *Journal of biomedical optics 17,* 4 (2012), 0405051–0405053.

[13] Brustlein, S., Berto, P., Hostein, R., Ferrand, P., Billaudeau, C., Marguet, D., Muir, A., Knight, J., and Rigneault, H. Double-clad hollow core photonic crystal fiber for coherent raman endoscope. *Optics Express 19,* 13 (June 2011), 12562–12568.

[14] Camp Jr, C. H., and Cicerone, M. T. Chemically sensitive bioimaging with coherent raman scattering. *Nature Photonics 9,* 5 (2015), 295–305.

[15] Campagnola, P., and Dong, C.-Y. Second harmonic generation microscopy: principles and applications to disease diagnosis. *Laser and Photonics Reviews 5,* 1 (2011), 13–26.

[16] Chan, F. T. S., Kaminski Schierle, G. S., Kumita, J. R., Bertoncini, C. W., Dobson, C. M., and Kaminski, C. F. Video-rate molecular imaging in vivo with stimulated raman scattering. *The Analyst 138,* 7 (2013), 2156.

[17] Chen, P., Shen, A., Zhou, X., and Hu, J. Bio-raman spectroscopy: a potential clinical analytical method assisting in disease diagnosis. *Anal. Methods 3* (2011), 1257–1269.

[18] Chen, X., Xu, X., McCormick, D. T., Wong, K., and Wong, S. T. Multimodal nonlinear endo-microscopy probe design for high resolution, label-free intraoperative imaging. *Biomedical optics express 6,* 7 (2015), 2283–2293.

[19] Cheng, J.-X., Book, L. D., and Xie, X. S. Polarization coherent anti-stokes raman scattering microscopy. *Optics letters 26,* 17 (2001), 1341–1343.

[20] Cheng, J.-X., and Xie, X. S. *Coherent Raman Scattering Microscopy*. CRC Press, Oct. 2012.

[21] Cheng, J.-X., and Xie, X. S. Vibrational spectroscopic imaging of living systems: An emerging platform for biology and medicine. *Science 350,* 6264 (2015).

[22] Clark, S., Ilday, F., and Wise, F. Fiber delivery of femtosecond pulses from a ti: sapphire laser. *Optics letters 26,* 17 (2001), 1320–1322.

[23] Conkey, D. B., Stasio, N., Morales-Delgado, E. E., Romito, M., Moser, C., and Psaltis, D. Lensless two-photon imaging through a multicore fiber with coherence-

gated digital phase conjugation. *Journal of biomedical optics 21,* 4 (2016), 045002–045002.

[24] COUNY, F., BENABID, F., AND LIGHT, P. S. Large-pitch kagome-structured hollow-core photonic crystal fiber. *Optics Letters 31*, 24 (Dec. 2006), 3574–3576.

[25] DEBORD, B., AMSANPALLY, A., BLONDY, J.-M., GÉRÔME, F., AND BENABID, F. Low loss inhibited coupling hollow-core photonic crystal fiber with ultrabroad fundamental band. In *CLEO: Science and Innovations* (2016), Optical Society of America, pp. STu4P–2.

[26] DELADURANTAYE, P., PAQUET, A., PARÉ, C., ZHENG, H., DOUCET, M., GAY, D., POIRIER, M., CORMIER, J.-F., MERMUT, O., WILSON, B. C., ET AL. Advances in engineering of high contrast cars imaging endoscopes. *Optics express 22,* 21 (2014), 25053–25064.

[27] DENK, W., STRICKLER, J. H., AND WEBB, W. W. Two-photon laser scanning fluorescence microscopy. *Science (New York, N.Y.) 248*, 4951 (Apr. 1990), 73–76.

[28] DENK, W., AND SVOBODA, K. Photon upmanship: why multiphoton imaging is more than a gimmick. *Neuron 18,* 3 (1997), 351–357.

[29] DIASPRO, A. *Confocal and two-photon microscopy: foundations, applications and advances*. Wiley-Liss, 2001.

[30] DOMBECK, D. A., KASISCHKE, K. A., VISHWASRAO, H. D., INGELSSON, M., HYMAN, B. T., AND WEBB, W. W. Uniform polarity microtubule assemblies imaged in native brain tissue by second-harmonic generation microscopy. *Proceedings of the National Academy of Sciences 100,* 12 (2003), 7081–7086.

[31] DUCOURTHIAL, G. *Développement d'un endomicroscope multiphotonique compact et flexible pour l'imagerie in vivo haute résolution de tissus biologiques non marqués*. PhD thesis, Limoges, 2014.

[32] DUCOURTHIAL, G., LECLERC, P., MANSURYAN, T., FABERT, M., BREVIER, J., HABERT, R., BRAUD, F., BATRIN, R., VEVER-BIZET, C., BOURG-HECKLY, G., ET AL. Development of a real-time flexible multiphoton microendoscope for label-free imaging in a live animal. *Scientific reports 5* (2015).

[33] DUNCAN, M. D., REINTJES, J., AND MANUCCIA, T. Scanning coherent anti-stokes raman microscope. *Optics letters 7*, 8 (1982), 350–352.

[34] ECKHARDT, G., BORTFELD, D. P., AND GELLER, M. Stimulated emission of stokes and anti?stokes raman lines from diamond, calcite, and ??sulfur single crystals. *Applied Physics Letters 3*, 8 (1963), 137–138.

[35] ENGELBRECHT, C. J., JOHNSTON, R. S., SEIBEL, E. J., AND HELMCHEN, F. Ultra-compact fiber-optic two-photon microscope for functional fluorescence imaging in vivo. *Optics express 16*, 8 (Apr. 2008), 5556–5564.

[36] EVANS, C. L., POTMA, E. O., PUORIS'HAAG, M., CT, D., LIN, C. P., AND XIE, X. S. Chemical imaging of tissue in vivo with video-rate coherent anti-stokes raman scattering microscopy. *Proceedings of the National Academy of Sciences of the United States of America 102*, 46 (Nov. 2005), 16807–16812.

[37] FERNANDEZ, D. C., BHARGAVA, R., HEWITT, S. M., AND LEVIN, I. W. Infrared spectroscopic imaging for histopathologic recognition. *Nature biotechnology 23*, 4 (2005), 469–474.

[38] FERRAND, P. Gpscan. vi: A general-purpose labview program for scanning imaging or any application requiring synchronous analog voltage generation and data acquisition. *Computer Physics Communications 192* (2015), 342–347.

[39] FERRAND, P., WENGER, J., DEVILEZ, A., PIANTA, M., STOUT, B., BONOD, N., POPOV, E., AND RIGNEAULT, H. Direct imaging of photonic nanojets. *Optics express 16*, 10 (2008), 6930–6940.

[40] FLUSBERG, B. A., COCKER, E. D., PIYAWATTANAMETHA, W., JUNG, J. C., CHEUNG, E. L., AND SCHNITZER, M. J. Fiber-optic fluorescence imaging. *Nature methods 2*, 12 (2005), 941–950.

[41] FLUSBERG, B. A., COCKER, E. D., PIYAWATTANAMETHA, W., JUNG, J. C., CHEUNG, E. L. M., AND SCHNITZER, M. J. Fiber-optic fluorescence imaging. *Nature methods 2*, 12 (Dec. 2005), 941–950.

[42] FRANKEN, P. A., HILL, A. E., PETERS, C. W., AND WEINREICH, G. Generation of optical harmonics. *Phys. Rev. Lett. 7* (Aug 1961), 118–119.

[43] FREUDIGER, C. W., MIN, W., SAAR, B. G., LU, S., HOLTOM, G. R., HE, C., TSAI, J. C., KANG, J. X., AND XIE, X. S. Label-free biomedical imaging with high sensitivity by stimulated raman scattering microscopy. *Science 322*, 5909 (2008), 1857–1861.

[44] FREUDIGER, C. W., PFANNL, R., ORRINGER, D. A., SAAR, B. G., JI, M., ZENG, Q., OTTOBONI, L., YING, W., WAEBER, C., SIMS, J. R., ET AL. Multicolored stain-free histopathology with coherent raman imaging. *Laboratory investigation 92*, 10 (2012), 1492–1502.

[45] FU, D., YE, T., MATTHEWS, T. E., YURTSEVER, G., AND WARREN, W. S. Two-color, two-photon, and excited-state absorption microscopy. *Journal of biomedical optics 12*, 5 (2007), 054004–054004.

[46] Fu, L., and Gu, M. Fibre-optic nonlinear optical microscopy and endoscopy. *Journal of microscopy 226,* Pt 3 (June 2007), 195–206.

[47] Fu, L., Jain, A., Xie, H., Cranfield, C., and Gu, M. Nonlinear optical endoscopy based on a double-clad photonic crystal fiber and a mems mirror. *Optics Express 14,* 3 (2006), 1027–1032.

[48] Ganikhanov, F., Evans, C. L., Saar, B. G., and Xie, X. S. High-sensitivity vibrational imaging with frequency modulation coherent anti-stokes raman scattering (fm cars) microscopy. *Optics letters 31,* 12 (2006), 1872–1874.

[49] Gasecka, P. *Polarization resolved nonlinear multimodal microscopy in lipids: from model membranes to myelin in tissues.* Theses, Université Aix-Marseille, Dec. 2015.

[50] Ghenuche, P., Rammler, S., Joly, N. Y., Scharrer, M., Frosz, M., Wenger, J., Russell, P. S. J., and Rigneault, H. Kagome hollow-core photonic crystal fiber probe for raman spectroscopy. *Optics letters 37*, 21 (2012), 4371–4373.

[51] Ghenuche, P., Rigneault, H., and Wenger, J. Hollow-core photonic crystal fiber probe for remote fluorescence sensing with single molecule sensitivity. *Optics express 20*, 27 (2012), 28379–28387.

[52] Göbel, W., Kerr, J. N., Nimmerjahn, A., and Helmchen, F. Miniaturized two-photon microscope based on a flexible coherent fiber bundle and a gradient-index lens objective. *Optics letters 29*, 21 (2004), 2521–2523.

[53] Göbel, W., Nimmerjahn, A., and Helmchen, F. Distortion-free delivery of nano-joule femtosecond pulses from a ti: sapphire laser through a hollow-core photonic crystal fiber. *Optics letters 29*, 11 (2004), 1285–1287.

[54] Göppert-Mayer, M. Über elementarakte mit zwei quantensprüngen. *Annalen der Physik 401,* 3 (1931), 273–294.

[55] Guichard, F., Giree, A., Zaouter, Y., Hanna, M., Machinet, G., Debord, B., Gérôme, F., Dupriez, P., Druon, F., Hönninger, C., Mottay, E., Benabid, F., and Georges, P. Nonlinear compression of high energy fiber amplifier pulses in air-filled hypocycloid-core kagome fiber. *Opt. Express 23,* 6 (Mar 2015), 7416–7423.

[56] Haringsma, J., Tytgat, G. N., Yano, H., Iishi, H., Tatsuta, M., Ogihara, T., Watanabe, H., Sato, N., Marcon, N., Wilson, B. C., et al. Autofluorescence endoscopy: feasibility of detection of gi neoplasms unapparent to white light endoscopy with an evolving technology. *Gastrointestinal endoscopy 53,* 6 (2001), 642–650.

[57] Hellerer, T., Enejder, A. M., and Zumbusch, A. Spectral focusing: High spectral resolution spectroscopy with broad-bandwidth laser pulses. *Applied Physics Letters 85*, 1 (2004), 25–27.

[58] Helmchen, F., and Denk, W. Deep tissue two-photon microscopy. *Nature methods 2*, 12 (2005), 932–940.

[59] Helmchen, F., Fee, M. S., Tank, D. W., and Denk, W. A miniature head-mounted two-photon microscope: High-resolution brain imaging in freely moving animals. *Neuron 31*, 6 (Sept. 2001), 903–912.

[60] Hompland, T., Erikson, A., Lindgren, M., Lindmo, T., and de Lange Davies, C. Second-harmonic generation in collagen as a potential cancer diagnostic parameter. *Journal of biomedical optics 13*, 5 (2008), 054050–054050.

[61] Humbert, G., Knight, J., Bouwmans, G., Russell, P., Williams, D., Roberts, P., and Mangan, B. Hollow core photonic crystal fibers for beam delivery. *Optics express 12*, 8 (2004), 1477–1484.

[62] Ikeda, N., Hiyoshi, T., Kakihana, M., Honda, H., Kato, Y., Okunaka, T., Furukawa, K., Tsuchida, T., Kato, H., and Ebihara, Y. Histopathological evaluation of fluorescence bronchoscopy using resected lungs in cases of lung cancer. *Lung Cancer 41*, 3 (2003), 303–309.

[63] J. A. C. Weideman, B. M. H. Split-step methods for the solution of the nonlinear schrodinger equation. *SIAM Journal on Numerical Analysis 23*, 3 (1986), 485–507.

[64] Jermyn, M., Mok, K., Mercier, J., Desroches, J., Pichette, J., Saint-Arnaud, K., Bernstein, L., Guiot, M.-C., Petrecca, K., and Leblond, F. Intraoperative brain cancer detection with raman spectroscopy in humans. *Science translational medicine 7*, 274 (2015), 274ra19–274ra19.

[65] Ji, M., Orringer, D. A., Freudiger, C. W., Ramkissoon, S., Liu, X., Lau, D., Golby, A. J., Norton, I., Hayashi, M., Agar, N. Y., et al. Rapid, label-free detection of brain tumors with stimulated raman scattering microscopy. *Science translational medicine 5*, 201 (2013), 201ra119–201ra119.

[66] Jun, C. S., Kim, B. Y., Park, J. H., Lee, J. Y., Lee, E. S., and Yeom, D.-I. Investigation of a four-wave mixing signal generated in fiber-delivered cars microscopy. *Applied optics 49*, 20 (2010), 3916–3921.

[67] Jung, W., Tang, S., McCormic, D. T., Xie, T., Ahn, Y.-C., Su, J., Tomov, I. V., Krasieva, T. B., Tromberg, B. J., and Chen, Z. Miniaturized probe based

on a microelectromechanical system mirror for multiphoton microscopy. *Optics letters 33*, 12 (2008), 1324–1326.

[68] KAISER, W., AND GARRETT, C. G. B. Two-photon excitation in caf$_2$: eu^{2+}. *Phys. Rev. Lett. 7* (Sep 1961), 229–231.

[69] KIM, S.-H., LEE, E.-S., LEE, J. Y., LEE, E. S., LEE, B.-S., PARK, J. E., AND MOON, D. W. Multiplex coherent anti-stokes raman spectroscopy images intact atheromatous lesions and concomitantly identifies distinct chemical profiles of atherosclerotic lipids. *Circulation research 106*, 8 (2010), 1332–1341.

[70] KISKIS, J., FINK, H., NYBERG, L., THYR, J., LI, J.-Y., AND ENEJDER, A. Plaque-associated lipids in alzheimerŠs diseased brain tissue visualized by nonlinear microscopy. *Scientific reports 5* (2015).

[71] KNIGHT, J., BIRKS, T., RUSSELL, P. S. J., AND ATKIN, D. All-silica single-mode optical fiber with photonic crystal cladding. *Optics letters 21*, 19 (1996), 1547–1549.

[72] KNIGHT, J., AND SKRYABIN, D. Nonlinear waveguide optics and photonic crystal fibers. *Optics Express 15*, 23 (2007), 15365–15376.

[73] KNOX, W., FORK, R., DOWNER, M., STOLEN, R., SHANK, C., AND VALDMANIS, J. Optical pulse compression to 8 fs at a 5-khz repetition rate. *Applied Physics Letters 46* (1985), 1120.

[74] KOBAYASHI, M., TAJIRI, H., SEIKE, E., SHITAYA, M., TOUNOU, S., MINE, M., AND OBA, K. Detection of early gastric cancer by a real-time autofluorescence imaging system. *Cancer letters 165*, 2 (2001), 155–159.

[75] KÖNIG, K., BREUNIG, H., BÜCKLE, R., KELLNER-HÖFER, M., WEINIGEL, M., BÜTTNER, E., STERRY, W., AND LADEMANN, J. Optical skin biopsies by clinical cars and multiphoton fluorescence/shg tomography. *Laser Physics Letters 8*, 6 (2011), 465–468.

[76] KRAFFT, C., STEINER, G., BELEITES, C., AND SALZER, R. Disease recognition by infrared and raman spectroscopy. *Journal of Biophotonics 2*, 1-2 (2009), 13–28.

[77] KUNDRAT, M. J., REINHALL, P. G., LEE, C. M., AND SEIBEL, E. J. High performance open loop control of scanning with a small cylindrical cantilever beam. *Journal of Sound and Vibration 330*, 8 (Apr. 2011), 1762–1771.

[78] KUNDRAT, M. J., REINHALL, P. G., LEE, C. M., AND SEIBEL, E. J. High performance open loop control of scanning with a small cylindrical cantilever beam. *Journal of sound and vibration 330*, 8 (2011), 1762–1771.

[79] Latka, I., Dochow, S., Krafft, C., Dietzek, B., and Popp, J. Fiber optic probes for linear and nonlinear raman applications Ű current trends and future development. *Laser and Photonics Reviews 7*, 5 (2013), 698–731.

[80] Le, T. T., Huff, T. B., and Cheng, J.-X. Coherent anti-stokes raman scattering imaging of lipids in cancer metastasis. *BMC cancer 9*, 1 (2009), 1.

[81] Le, T. T., Langohr, I. M., Locker, M. J., Sturek, M., and Cheng, J.-X. Label-free molecular imaging of atherosclerotic lesions using multimodal nonlinear optical microscopy. *Journal of biomedical optics 12*, 5 (2007), 054007–054007.

[82] Le Harzic, R., Riemann, I., Weinigel, M., König, K., and Messerschmidt, B. Rigid and high-numerical-aperture two-photon fluorescence endoscope. *Applied optics 48*, 18 (2009), 3396–3400.

[83] Lee, C. M., Engelbrecht, C. J., Soper, T. D., Helmchen, F., and Seibel, E. J. Scanning fiber endoscopy with highly flexible, 1-mm catheterscopes for wide-field, full-color imaging. *Journal of biophotonics 3*, 5-6 (2010), 385.

[84] Lee, C. M., Engelbrecht, C. J., Soper, T. D., Helmchen, F., and Seibel, E. J. Scanning fiber endoscopy with highly flexible, 1 mm catheterscopes for wide-field, full-color imaging. *Journal of Biophotonics 3*, 5-6 (2010), 385–407.

[85] Lee, J. H., Kim, D. H., Song, W. K., Oh, M.-K., and Ko, D.-K. Label-free imaging and quantitative chemical analysis of alzheimerŠs disease brain samples with multimodal multiphoton nonlinear optical microspectroscopy. *Journal of biomedical optics 20*, 5 (2015), 056013–056013.

[86] Légaré, F., Evans, C. L., Ganikhanov, F., and Xie, X. S. Towards cars endoscopy. *Optics Express 14*, 10 (2006), 4427–4432.

[87] Leonard, D. A. Observation of raman scattering from the atmosphere using a pulsed nitrogen ultraviolet laser. *Nature 216* (1967), 142–143.

[88] Levenson, M., and Bloembergen, N. Dispersion of the nonlinear optical susceptibility tensor in centrosymmetric media. *Physical Review B 10*, 10 (1974), 4447.

[89] Llewellyn, M. E., Barretto, R. P., Delp, S. L., and Schnitzer, M. J. Minimally invasive high-speed imaging of sarcomere contractile dynamics in mice and humans. *Nature 454*, 7205 (2008), 784–788.

[90] Lotem, H., Lynch Jr, R., and Bloembergen, N. Interference between raman resonances in four-wave difference mixing. *Physical Review A 14*, 5 (1976), 1748.

[91] Lu, F.-K., Basu, S., Igras, V., Hoang, M. P., Ji, M., Fu, D., Holtom, G. R., Neel, V. A., Freudiger, C. W., Fisher, D. E., et al. Label-free dna imaging in vivo with stimulated raman scattering microscopy. *Proceedings of the National Academy of Sciences 112*, 37 (2015), 11624–11629.

[92] Lu, S., Min, W., Chong, S., Holtom, G. R., and Xie, X. S. Label-free imaging of heme proteins with two-photon excited photothermal lens microscopy. *Applied Physics Letters 96*, 11 (2010), 113701.

[93] Luan, F., Knight, J. C., Russell, P. S. J., Campbell, S., Xiao, D., Reid, D. T., Mangan, B. J., Williams, D. P., and Roberts, P. J. Femtosecond soliton pulse delivery at 800nm wavelength in hollow-core photonic bandgap fibers. *Opt. Express 12*, 5 (Mar 2004), 835–840.

[94] Maker, P. D., and Terhune, R. W. Study of optical effects due to an induced polarization third order in the electric field strength. *Phys. Rev. 137* (Feb 1965), A801–A818.

[95] Masters, B. R., and So, P. *Handbook of biomedical nonlinear optical microscopy*. Oxford University Press on Demand, 2008.

[96] Mattha?us, C., Dochow, S., Bergner, G., Lattermann, A., Romeike, B. F., Marple, E. T., Krafft, C., Dietzek, B., Brehm, B. R., and Popp, J. In vivo characterization of atherosclerotic plaque depositions by raman-probe spectroscopy and in vitro coherent anti-stokes raman scattering microscopic imaging on a rabbit model. *Analytical chemistry 84*, 18 (2012), 7845–7851.

[97] Meyer, T., Bergner, N., Bielecki, C., Krafft, C., Akimov, D., Romeike, B. F., Reichart, R., Kalff, R., Dietzek, B., and Popp, J. Nonlinear microscopy, infrared, and raman microspectroscopy for brain tumor analysis. *Journal of biomedical optics 16*, 2 (2011), 021113–021113.

[98] Mittal, R., Balu, M., Krasieva, T., Potma, E. O., Elkeeb, L., Zachary, C. B., and Wilder-Smith, P. Evaluation of stimulated raman scattering microscopy for identifying squamous cell carcinoma in human skin. *Lasers in surgery and medicine 45*, 8 (2013), 496–502.

[99] Mittal, R., Balu, M., Wilder-Smith, P., and Potma, E. O. Achromatic miniature lens system for coherent raman scattering microscopy. *Biomedical optics express 4*, 10 (2013), 2196–2206.

[100] MOLLENAUER, L. F., STOLEN, R. H., AND GORDON, J. P. Experimental observation of picosecond pulse narrowing and solitons in optical fibers. *Phys. Rev. Lett. 45* (Sep 1980), 1095–1098.

[101] MORALES-DELGADO, E. E., PSALTIS, D., AND MOSER, C. Two-photon imaging through a multimode fiber. *Optics express 23*, 25 (2015), 32158–32170.

[102] MOVASAGHI, Z., REHMAN, S., AND REHMAN, D. I. U. Raman spectroscopy of biological tissues. *Applied Spectroscopy Reviews 42*, 5 (2007), 493–541.

[103] MURARI, K., ZHANG, Y., LI, S., CHEN, Y., LI, M.-J., AND LI, X. Compensation-free, all-fiber-optic, two-photon endomicroscopy at 1.55 μm. *Optics letters 36*, 7 (2011), 1299–1301.

[104] MURUGKAR, S., SMITH, B., SRIVASTAVA, P., MOICA, A., NAJI, M., BRIDEAU, C., STYS, P. K., AND ANIS, H. Miniaturized multimodal cars microscope based on mems scanning and a single laser source. *Optics express 18*, 23 (2010), 23796–23804.

[105] MYAING, M. T., MACDONALD, D. J., AND LI, X. Fiber-optic scanning two-photon fluorescence endoscope. *Optics letters 31*, 8 (2006), 1076–1078.

[106] NIEMAN, K. M., ROMERO, I. L., VAN HOUTEN, B., AND LENGYEL, E. Adipose tissue and adipocytes support tumorigenesis and metastasis. *Biochimica et Biophysica Acta (BBA)-Molecular and Cell Biology of Lipids 1831*, 10 (2013), 1533–1541.

[107] OUZOUNOV, D. G., AHMAD, F. R., MÜLLER, D., VENKATARAMAN, N., GALLAGHER, M. T., THOMAS, M. G., SILCOX, J., KOCH, K. W., AND GAETA, A. L. Generation of megawatt optical solitons in hollow-core photonic band-gap fibers. *Science 301*, 5640 (2003), 1702–1704.

[108] PALONPON, A. F., ANDO, J., YAMAKOSHI, H., DODO, K., SODEOKA, M., KAWATA, S., AND FUJITA, K. Raman and sers microscopy for molecular imaging of live cells. *Nature protocols 8*, 4 (2013), 677–692.

[109] PAPADOPOULOS, I. N., FARAHI, S., MOSER, C., AND PSALTIS, D. High-resolution, lensless endoscope based on digital scanning through a multimode optical fiber. *Biomedical optics express 4*, 2 (2013), 260–270.

[110] PEARCE, G., WIEDERHECKER, G., POULTON, C., BURGER, S., AND RUSSELL, P. S. J. Models for guidance in kagome-structured hollow-core photonic crystal fibres. *Optics express 15*, 20 (2007), 12680–12685.

[111] Pearce, G. J., Wiederhecker, G. S., Poulton, C. G., Burger, S., and St. J. Russell, P. Models for guidance in kagome-structured hollow-core photonic crystal fibres. *Optics Express 15,* 20 (Oct. 2007), 12680–12685.

[112] Ploetz, E., Laimgruber, S., Berner, S., Zinth, W., and Gilch, P. Femtosecond stimulated raman microscopy. *Applied Physics B 87,* 3 (2007), 389–393.

[113] Plotnikov, S. V., Millard, A. C., Campagnola, P. J., and Mohler, W. A. Characterization of the myosin-based source for second-harmonic generation from muscle sarcomeres. *Biophysical journal 90,* 2 (2006), 693–703.

[114] Potma, E. O., Evans, C. L., and Xie, X. S. Heterodyne coherent anti-stokes raman scattering (cars) imaging. *Optics letters 31*, 2 (2006), 241–243.

[115] Provenzano, P. P., Eliceiri, K. W., Campbell, J. M., Inman, D. R., White, J. G., and Keely, P. J. Collagen reorganization at the tumor-stromal interface facilitates local invasion. *BMC medicine 4,* 1 (2006), 1.

[116] Rivera, D. R., Brown, C. M., Ouzounov, D. G., Pavlova, I., Kobat, D., Webb, W. W., and Xu, C. Compact and flexible raster scanning multiphoton endoscope capable of imaging unstained tissue. *Proceedings of the National Academy of Sciences 108,* 43 (Oct. 2011), 17598–17603.

[117] Russell, P. Photonic crystal fibers. *science 299,* 5605 (2003), 358–362.

[118] Russell, P. S. J. Photonic-crystal fibers. *Journal of lightwave technology 24,* 12 (2006), 4729–4749.

[119] Russell, P. S. J., Hölzer, P., Chang, W., Abdolvand, A., and Travers, J. Hollow-core photonic crystal fibres for gas-based nonlinear optics. *Nat. Photonics 8,* 4 (2014), 278–286.

[120] Saar, B. G., Johnston, R. S., Freudiger, C. W., Xie, X. S., and Seibel, E. J. Coherent raman scanning fiber endoscopy. *Optics letters 36,* 13 (July 2011), 2396–2398.

[121] Saint-Jalm, S. *Sources optiques fibrées solitoniques pour la spectroscopie et la microscopie non linéaires*. PhD thesis, Aix-Marseille, 2014.

[122] Saint-Jalm, S., Andresen, E. R., Ferrand, P., Bendahmane, A., Mussot, A., Vanvincq, O., Bouwmans, G., Kudlinski, A., and Rigneault, H. Fiber-based ultrashort pulse delivery for nonlinear imaging using high-energy solitons. *Journal of biomedical optics 19,* 8 (2014), 086021–086021.

[123] Samineni, P., Li, B., Wilson, J. W., Warren, W. S., and Fischer, M. C. Cross-phase modulation imaging. *Optics letters 37*, 5 (2012), 800–802.

[124] Seibel, E. J., and Smithwick, Q. Y. Unique features of optical scanning, single fiber endoscopy. *Lasers in surgery and medicine 30*, 3 (2002), 177–183.

[125] Shephard, J., Jones, J., Hand, D., Bouwmans, G., Knight, J., Russell, P., and Mangan, B. High energy nanosecond laser pulses delivered single-mode through hollow-core pbg fibers. *Optics Express 12*, 4 (2004), 717–723.

[126] Shephard, J. D., Couny, F., Russell, P. S. J., Jones, J. D., Knight, J. C., and Hand, D. P. Improved hollow-core photonic crystal fiber design for delivery of nanosecond pulses in laser micromachining applications. *Applied optics 44*, 21 (2005), 4582–4588.

[127] Sinkin, O. V., Holzlöhner, R., Zweck, J., and Menyuk, C. R. Optimization of the split-step fourier method in modeling optical-fiber communications systems. *Journal of lightwave technology 21*, 1 (2003), 61.

[128] Sivankutty, S., Andresen, E. R., Cossart, R., Bouwmans, G., Monneret, S., and Rigneault, H. Ultra-thin rigid endoscope: two-photon imaging through a graded-index multi-mode fiber. *Optics express 24*, 2 (2016), 825–841.

[129] Smith, B., Naji, M., Murugkar, S., Alarcon, E., Brideau, C., Stys, P., and Anis, H. Portable, miniaturized, fibre delivered, multimodal cars exoscope. *Optics express 21*, 14 (2013), 17161–17175.

[130] Tai, S.-P., Chan, M.-C., Tsai, T.-H., Guol, S.-H., Chen, L.-J., and Sun, C.-K. Two-photon fluorescence microscope with a hollow-core photonic crystal fiber. *Optics express 12*, 25 (2004), 6122–6128.

[131] Tang, S., Jung, W., McCormick, D., Xie, T., Su, J., Ahn, Y.-C., Tromberg, B. J., and Chen, Z. Design and implementation of fiber-based multiphoton endoscopy with microelectromechanical systems scanning. *Journal of biomedical optics 14*, 3 (2009), 034005–034005.

[132] Tomlinson, W., Stolen, R., and Shank, C. Compression of optical pulses chirped by self-phase modulation in fibers. *JOSA B 1*, 2 (1984), 139–149.

[133] Toulouse, J. Optical nonlinearities in fibers: review, recent examples, and systems applications. *Journal of Lightwave Technology 23*, 11 (2005), 3625–3641.

[134] Tournois, P. New diffraction grating pair with very linear dispersion for laser pulse compression. *Electronics letters 29*, 16 (1993), 1414–1415.

[135] Tu, Q., and Chang, C. Diagnostic applications of raman spectroscopy. *Nanomedicine: Nanotechnology, Biology and Medicine 8*, 5 (2011), 545–558.

[136] Tzortzakis, S., Bergé, L., Couairon, A., Franco, M., Prade, B., and Mysyrowicz, A. Breakup and fusion of self-guided femtosecond light pulses in air. *Phys. Rev. Lett. 86* (Jun 2001), 5470–5473.

[137] Varadarajulu, S., Banerjee, S., Barth, B. A., Desilets, D. J., Kaul, V., Kethu, S. R., Pedrosa, M. C., Pfau, P. R., Tokar, J. L., Wang, A., et al. Gi endoscopes. *Gastrointestinal endoscopy 74*, 1 (2011), 1–6.

[138] Volkmer, A., Book, L. D., and Xie, X. S. Time-resolved coherent anti-stokes raman scattering microscopy: Imaging based on raman free induction decay. *Applied Physics Letters 80*, 9 (2002), 1505–1507.

[139] Wang, H., Fu, Y., Zickmund, P., Shi, R., and Cheng, J.-X. Coherent anti-stokes raman scattering imaging of axonal myelin in live spinal tissues. *Biophysical Journal 89*, 1 (2005), 581–591.

[140] Wang, H., Huff, T. B., Fu, Y., Jia, K. Y., and Cheng, J.-X. Increasing the imaging depth of coherent anti-stokes raman scattering microscopy with a miniature microscope objective. *Optics letters 32*, 15 (2007), 2212–2214.

[141] Wang, T. D., and Van Dam, J. Optical biopsy: A new frontier in endoscopic detection and diagnosis. *Clinical Gastroenterology and Hepatology 2* (2004), 744–753.

[142] Wang, Y., Alharbi, M., Bradley, T. D., Fourcade-Dutin, C., Debord, B., Beaudou, B., Gerôme, F., and Benabid, F. Hollow-core photonic crystal fibre for high power laser beam delivery. *High Power Laser Science and Engineering 1*, 01 (2013), 17–28.

[143] Wang, Y., Wheeler, N. V., Couny, F., Roberts, P., and Benabid, F. Low loss broadband transmission in hypocycloid-core kagome hollow-core photonic crystal fiber. *Optics letters 36*, 5 (2011), 669–671.

[144] Wang, Z., Gao, L., Luo, P., Yang, Y., Hammoudi, A. A., Wong, K. K., and Wong, S. T. Coherent anti-stokes raman scattering microscopy imaging with suppression of four-wave mixing in optical fibers. *Optics express 19*, 9 (2011), 7960–7970.

[145] Washburn, B. R., Buck, J. A., and Ralph, S. E. Transform-limited spectral compression due to self-phase modulation in fibers. *Optics letters 25*, 7 (2000), 445–447.

[146] Williams, R. M., Flesken-Nikitin, A., Ellenson, L. H., Connolly, D. C., Hamilton, T. C., Nikitin, A. Y., and Zipfel, W. R. Strategies for high resolution

imaging of epithelial ovarian cancer by laparoscopic nonlinear microscopy. *Translational oncology 3*, 3 (2010), 181–194.

[147] Wu, Y., Leng, Y., Xi, J., and Li, X. Scanning all-fiber-optic endomicroscopy system for 3d nonlinear optical imaging of biological tissues. *Optics express 17*, 10 (2009), 7907–7915.

[148] Xu, C., and Webb, W. W. Measurement of two-photon excitation cross sections of molecular fluorophores with data from 690 to 1050 nm. *JOSA B 13*, 3 (1996), 481–491.

[149] Xu, X., Cheng, J., Thrall, M. J., Liu, Z., Wang, X., and Wong, S. T. Multimodal non-linear optical imaging for label-free differentiation of lung cancerous lesions from normal and desmoplastic tissues. *Biomedical optics express 4*, 12 (2013), 2855–2868.

[150] Zhang, Y., Akins, M. L., Murari, K., Xi, J., Li, M.-J., Luby-Phelps, K., Mahendroo, M., and Li, X. A compact fiber-optic shg scanning endomicroscope and its application to visualize cervical remodeling during pregnancy. *Proceedings of the National Academy of Sciences 109*, 32 (2012), 12878–12883.

[151] Zhao, Y., Nakamura, H., and Gordon, R. J. Development of a versatile two-photon endoscope for biological imaging. *Biomedical optics express 1*, 4 (2010), 1159–1172.

[152] Zipfel, W. R., Williams, R. M., Christie, R., Nikitin, A. Y., Hyman, B. T., and Webb, W. W. Live tissue intrinsic emission microscopy using multiphoton-excited native fluorescence and second harmonic generation. *Proceedings of the National Academy of Sciences 100*, 12 (2003), 7075–7080.

[153] Zoumi, A., Yeh, A., and Tromberg, B. J. Imaging cells and extracellular matrix in vivo by using second-harmonic generation and two-photon excited fluorescence. *Proceedings of the National Academy of Sciences 99*, 17 (2002), 11014–11019.

[154] Zumbusch, A., Holtom, G. R., and Xie, X. S. Three-dimensional vibrational imaging by coherent anti-stokes raman scattering. *Physical Review Letters 82*, 20 (1999), 4142–4145.

Abstract

Nonlinear optical microscopy (NLOM) is a very powerful tool for live tissue imaging. It does not require staining of the samples and offers high spatial resolution and molecular specificity. Thanks to the combination of different nonlinear contrast mechanisms, such as two-photon fluorescence (TPEF), second harmonic generation (SHG) and coherent anti-Stokes Raman scattering (CARS), NLOM is now emerging as a serious candidate for future in-vivo label-free optical histology. However, the translation of nonlinear imaging into clinics depends very much on the development of miniature and portable endoscope probes. One main issue is represented by the transmission of the excitation ultra-short pulses with optical fibers. Pulse propagation in classical silica fibers is affected by a number of problems, such as temporal and spectral broadening, or generation of a strong background at the CARS wavelength. In this thesis, we propose the use of a novel type of photonic crystal fiber, the Kagomé lattice hollow core fiber, for the delivery of ultra-short pulses in nonlinear endoscopy. These fibers allow undistorted pulse delivery, over a broad transmission window, with minimum background signal generated in the fiber, thanks to the propagation in a hollow-core. We solved the problem of spatial resolution by means of a silica micro-bead inserted in the Kagomé fiber large core. We have developed a miniature imaging system, based on a piezo-electric tube scanner, an achromatic micro-lenses assembly and a custom design Kagomé double-clad fiber. With this system we were able to image biological tissues, in endoscope modality, activating different contrasts such as TPEF, SHG and CARS, a result which finds no equal in current literature. The integration in a portable probe (4.2 mm in diameter) shows the potential of this system for future in-vivo multimodal endoscopy.

Key words: Nonlinear optical microscopy; endoscopy; micro-structured optical fibers; Kagomé fibers; ultrashort pulse delivery; deep tissue imaging; coherent Raman scattering.

Résumé

La microscopie optique non linéaire (NLOM) est aujourd'hui un outil important pour l'imagerie des tissus en temps réel. Elle ne nécessite pas du marquage des échantillons et offre haute résolution spatiale et spécificité moléculaire. À l'aide de la combinaison de différents mécanismes de contraste non linéaires, tels que la fluorescence à deux photons (TPEF), la génération de seconde harmonique (SHG) et la diffusion anti-Stokes Raman cohérente (CARS), la NLOM se présente un candidat pour l'application à l'histologie optique sans marquage. Cependant, le transfert de l'imagerie non linéaire dans les hôpitaux dépend fortement du développement de sondes endoscopiques flexibles et miniaturisées. La transmission des impulsions ultra-courtes, avec des fibres optiques, est l'un des principaux problèmes à régler. Il existe des nombreux effets liés à la propagation des impulsions dans les fibres de silice classiques, tels que l'élargissement temporel et spectral, ou la génération d'un bruit de fond à la longueur d'onde CARS. Dans cette thèse, nous proposons l'utilisation d'un nouveau type de fibre à cristal photonique, la fibre Kagomé à coeur creux, pour la livraison d'impulsions ultra-courtes en endoscopie non linéaire. Ces fibres permettent la livraison d'impulsions sans distorsion sur une large bande spectrale, avec un faible bruit de fond, grâce à la propagation dans le coeur creux. Nous avons résolu le problème de la résolution spatiale, à l'aide d'une microbille en silice, insérée dans le coeur de la fibre Kagomé. Nous avons développé un système d'imagerie compacte, qui utilise un tube piezo-électrique pour le balayage du faisceau, un système achromatique de microlentilles et une fibre Kagomé double gaine, spécialement conçue pour l'endoscopie. Avec ce système, nous avons réussi à imager des tissus biologiques, à l'extrémité distale de la fibre, en utilisant des différentes techniques tels que TPEF, SHG et CARS, un résultat qui ne trouve pas égale dans la littérature actuelle. L'intégration dans une sonde portable (4,2 mm de diamètre) montre le potentiel de ce système pour de futures applications en endoscopie multimodale in-vivo.

Key words: Microscopie optique non-lineaire; endoscopie; fibres optiques micro-structurées ; fibres Kagomé; livraison des impulsions ultra-courtes; imagerie des tissus en profondeur; diffusion Raman cohérente.